Progress and Applications of (Cu-)Ag-Bi-I Semiconductors, and Their Derivatives, as Next-Generation Lead-Free Materials for Photovoltaics, Detectors and Memristors

Huimin Zhu,[*,†] Ivan Turkevych,[*,¶] Hugh Lohan,[‡] Pengjun Liu,[‡] Robert W. Martin,[†] Fabien C. P. Massabuau,[†] and Robert L. Z. Hoye[*,‡]

†*Department of Physics, SUPA, University of Strathclyde, Glasgow, G4 0NG, United Kingdom*

‡*Inorganic Chemistry Laboratory, Department of Chemistry, University of Oxford, South Parks Road, Oxford OX1 3QR, United Kingdom*

¶*National Institute of Advanced Industrial Science and Technology, Tsukuba, Ibaraki 305-8565, Japan*

§*Department of Materials, Imperial College London, Exhibition Road, London SW7 2AZ, United Kingdom*

E-mail: huimin.zhu@strath.ac.uk; ivan.turkevych@aist.go.jp; robert.hoye@chem.ox.ac.uk

Abstract

The search for efficient but inexpensive photovoltaics over the past decade has been disrupted by the advent of lead-halide perovskite solar cells. Despite impressive rises in performance, the toxicity and stability concerns of these materials have prompted a broad, interdisciplinary community across the world to search for lead-free and stable alternatives.

A set of such materials that have recently gained attention are semiconductors in the CuI-AgI-BiI_3 phase space, and their derivatives. These materials include ternary silver bismuth iodide compounds ($Ag_aBi_bI_{a+3b}$), ternary copper bismuth iodide Cu-Bi-I compounds, and quaternary Cu-Ag-Bi-I materials, as well as analogs with Sb substituted into the Bi site and Br into the I site. These compounds are comprised of a cubic close packed sub-lattice of I, with Ag and Bi occupying octahedral holes, while Cu occupies tetrahedral holes. The octahedral motifs adopted by these compounds are either spinel, $CdCl_2$-type, or $NaVO_2$-type. $NaVO_2$-type $Ag_aBi_bI_{a+3b}$ compounds are also known as rudorffites. Many of these compounds have thus far demonstrated improved stability and reduced toxicity compared to halide perovskites, along with stable bandgaps in the 1.6-1.9 eV range, making them highly promising for energy harvesting and detection applications. This review begins by discussing the progress in the development of these semiconductors over the past few years, focusing on their optoelectronic properties and process-property-structure relationships. Next, we discuss the progress in developing Ag-Bi-I and Cu-Bi-I compounds for solar cells, indoor photovoltaics, photodetectors, radiation detectors and memristors. We finish with a discussion of the critical fundamental questions that need to be addressed to push this area forward, and how the learnings from the wider metal-halide semiconductor field can inform future directions.

Keywords: rudorffites, lead-free perovskite-inspired materials, photovoltaics, energy harvesting, Internet of Things, thin films, photodetectors, memristors

1. Introduction

Metal-halide semiconductors have recently gained significant interest as novel energy conversion materials.[1–3] This has been driven by the astonishing rises in performance of lead-halide perovskite (LHPs) devices, originally in photovoltaics,[4,5] but now also in light-emitting diodes,[6] radiation detectors,[7] field-effect transistors,[8] photoelectrochemical cells,[9] and many other applications. However, lead is toxic and regulated in many jurisdictions,

which, for example, may prevent the commercial use of LHP devices in consumer electronics.[10,11] Furthermore, the polar solvents used for processing LHPs are toxic and environmentally harmful.[12] These limitations have prompted a global effort to develop alternative classes of materials that can replicate the exceptional optoelectronic properties of the LHPs (especially their defect tolerance),[13,14] but which are stable (under thermal, environmental and light stressors) and overcome the toxicity challenges. However, simply substituting Pb for Sn or Ge has led to perovskites with inferior photovoltaic performance that still have limited stability.[15] In considering the broader family of metal-halide semiconductors, ternary and quaternary compounds within the CuI-AgI-BiI_3 phase space have recently gained increasing attention.

Ternary Ag-Bi-I and Cu-Bi-I semiconductors were originally investigated several decades ago as potential ionic conductors, but were found to exhibit poor ionic conductivity.[16–20] Following the rise in efforts to find lead-free alternatives to metal-halide perovskites, two groups reported the use of Ag-Bi-I compounds in photovoltaics in 2016, with a patent from Turkevych *et al.* reporting 4.3% power conversion efficiency (PCE),[21] and a paper from Kim *et al.* reporting 1.22% PCE.[22] Since then, there have been many efforts to develop these materials as solar cells, particularly since the optical limit in efficiency (*i.e.*, spectroscopic limited maximum efficiency, or SLME) is well in excess of 20%,[23] showing there to be much room for improvement. In addition, these materials have been shown to have highly-promising absorption properties for indoor light harvesting, with SLMEs exceeding 50%.[23,24] In 2017, it was proposed to call these Ag-Bi-I compounds "rudorffites" because the Ag-rich compounds adopted a $NaVO_2$-type structure, which was first investigated by Rüdorff and Becker in 1954.[25] However, as will be discussed in Section 2, Ag-Bi-I semiconductors do not adopt only one structure, but also the layered $CdCl_2$ structure and 3D spinel structure. Although there is a tendency in the wider field now to collectively refer to the family of Ag-Bi-I compounds (and their substitutional derivatives) as rudorffites, we emphasize that this is not strictly correct, since "rudorffite" would then also be referring to compounds that

do not have the $NaVO_2$ structure.

Beyond promising performance, the Ag-Bi-I compounds are advantageous in that they have stable performance in photovoltaic devices in ambient air,[26,27] with structural and optoelectronic properties that are tunable through the composition (e.g., the ratio of Ag/Bi cations).[20,24] There has also been rekindled interest in Cu-Bi-I compounds, but some of these materials have been reported to not be as stable as their ternary Ag-based analogs.[28] Including both Cu and Ag to form quaternary compounds has been found to retain the stability of Ag-Bi-I compounds, but also reduce the total quantity of Ag (which is expensive and toxic to aquatic life when released to water as Ag^+).[28] However, these materials are at an early stage in their development, and there are many unresolved questions on their process-property-structure relationships, such as what trap states limit performance, and the role of carrier-phonon coupling on charge-carrier transport. Answering these questions will be crucial to moving the field forward toward the efficiency limits of these materials.

This Full Critical Review examines the potential and future directions of the family of materials within the CuI-AgI-BiI_3 phase space, as well as their derivatives, for both solar- and visible-light harvesting for optoelectronic applications, as well as more broadly for energy conversion and detection. The scope of this review is shown in Fig. 1. Whilst there have been many previous reviews on LHPs and pnictogen-based perovskite-inspired materials (see for example Ref.[29–31]), rudorffites and other Cu-Ag-Bi-I materials have not featured in these in detail. Given the gathering pace of this emerging field, a comprehensive review focused on these materials is called for,[32] especially to highlight important recent developments, including carrier localization, the role of defects on photovoltaic performance, and advances in indoor light harvesting, which have not been covered in previous reviews. The review begins by discussing the structure-property relationships of Ag-Bi-I semiconductors (which have by far the largest body of literature), followed by Cu-Bi-I compounds, and then the quaternary Cu-Ag-Bi-I materials. Within each sub-section for each set of materials, we discuss the structure, optoelectronic properties, charge-carrier transport properties and the

effects of chemical substitution on these properties. Furthermore, we discuss the stability of the materials as a whole. Each section also briefly covers the synthesis methods investigated for each set of materials, but our emphasis in this review is on the core principles, and we do not extensively summarize the various synthesis routes attempted, which can be found in other reviews.[30,32] This discussion on structure-property relationships is then followed with a detailed discussion on the performance of these materials in solar cells (including how morphology can be controlled through processing), indoor photovoltaics, radiation detectors and memristors. We also discuss the potential for applying these materials in photocatalysis and photoelectrochemistry. Finally, we discuss the key outstanding challenges and future directions for this field.

2. Structure-Property Relationships of Compounds in the CuI-AgI-BiI_3 Phase Space, and their Derivatives

Over the past five years, the subset within the CuI-AgI-BiI_3 phase space of materials that have gained the greatest attention are the ternary Ag-Bi-I compounds. In particular, Ag_3BiI_6,[37–39] Ag_2BiI_5,[40–43] $AgBiI_4$,[44–46] $AgBi_2I_7$[22,47–49] have been popular. We therefore begin this section by discussing these Ag-Bi-I compounds, before discussing Cu-Bi-I compounds, followed by the quaternary Cu-Ag-Bi-I compounds. Within each of these three sub-sections, we discuss the structure of the materials, as well as the optoelectronic properties and band positions. Where studies have been made, we discuss the effects of chemical substitution into the metal cation and anion sites. Within each sub-section, we also discuss the stability of each of these classes of materials. Finally, we finish off the section with a collective discussion of defects and ion migration. Across each of these sub-sections, we reference how the materials discussed were synthesized, and discuss in detail the unusual features of synthesizing quaternary Cu-Ag-Bi-I compounds. But a more detailed discussion on the effects of processing on the morphology Ag-Bi-I and Cu-Bi-I materials, and their effects on solar cell performance, is provided later in Section 3.1.2.

2.1 Silver Bismuth Iodide (Ag-Bi-I) Compounds

2.1.1 Crystal Structure of Ag-Bi-I

The crystal structure of $Ag_aBi_bI_{a+3b}$ compounds vary with stoichiometry, as illustrated in Fig. 2a, and shown in Table 1. The structures of these materials were solved from both single crystal and powder X-ray diffraction (PXRD) measurements, with single crystals synthesized by solvothermal methods, chemical vapor transport (CVT) and vertical Bridgman method,[16–18,34,44] and powders grown by melt crystallization.[50] The common structures reported are: i) 3D defect spinel ($Fd\bar{3}m$), ii) a 2D $CdCl_2$-type structure ($R\bar{3}m$), and iii) a 3D rhombohedral $NaVO_2$-type structure ($R\bar{3}m$).[20,33] Bi-rich compounds ($AgBi_2I_7$ and $Ag_2Bi_3I_{11}$) adopt the defect spinel structure, while Ag-rich compounds (Ag_2BiI_5 and Ag_3BiI_6) adopt the $NaVO_2$-type structure.[20,33,44,49,50] $AgBiI_4$, with an equal concentration of Ag and Bi, has been reported to adopt either of these structures, or the $CdCl_2$-type structure.[20,44] All of these structures have a cubic close packed (ccp) I sub-lattice (Fig. 2b–d). At the extremes of the BiI_3-AgI phase space, both BiI_3 and AgI have a hexagonal close packed sub-lattice of I.[33] In close packed anion sub-lattices, there are two tetrahedral holes and one octahedral hole per anion. Bi^{3+}, Ag^+ and vacancies occupy octahedral holes, with the exception of AgI, in which Ag^+ occupies 1/2 of the tetrahedral holes (Fig. 2a). Ag^+ occupies a different lattice site in AgI than in Ag-Bi-I compounds because the I–I distance is larger in AgI (ca. 4.6 Å vs. ca. 4.3 Å in Ag-Bi-I compounds).[33] In BiI_3, there is a layered structure, and to maintain charge neutrality, Bi^{3+} occupies 2/3 of the octahedral holes in layer 1, while occupying no octahedral holes in layer 2, thus maintaining a Bi^{3+}:I^- ratio of 1:3 (Fig. 3a).[33] The defect spinel octahedral motif for Ag-Bi-I has 1/2 of the octahedral holes fully occupied overall, as shown in Fig. 2a.[20,33] This motif can also be depicted in the trigonal setting (Fig. 3b), in which layer 1 has 3/4 of the octahedral holes occupied, while layer 2 has 1/4 of the octahedral holes occupied.[44] Since Ag^+ and Bi^+ have very similar ionic radii (129 pm for Ag^+

and 117 pm for Bi^{3+}),[51] they occupy the same crystallographic lattice site. In $AgBiI_4$, each of the cation-occupied octahedral holes has an equal probability of being occupied by Ag^+ or Bi^{3+}. But as the stoichiometry becomes Bi-rich, vacancies also occupy these lattice sites in order to maintain charge neutrality.[20,33] The powder diffraction pattern for $AgBiI_4$ can also be explained with a $CdCl_2$-type structure. Therein, there are also 1/2 of the octahedral holes overall occupied with Ag^+ and Bi^{3+}. But this time, a 2D rather than 3D structure is adopted, as illustrated in Fig 3c. In layer 1, all of the octahedral holes are occupied, while in layer 2, none of the octahedral holes are occupied. It is likely that the Bi-rich compounds can also be explained by a $CdCl_2$ structure, although this is yet to be proven.[33] As the materials become Ag-rich, the extra Ag^+ cations partially occupy the octahedral holes in layer 2, and this gives rise to a 3D $NaVO_2$-type structure (Fig. 2a). Across all of these structures, from BiI_3 to Ag-rich Ag-Bi-I compounds, all BiI_6 and AgI_6 octahedra are edge-sharing, and all tetrahedral holes remain vacant.[33]

In addition to these commonly-reported structures, Turkevych *et al.* proposed that the structure of all $Ag_aBi_bI_{a+3b}$ compounds can be described based on the $NaVO_2$-type structure, and not just the Ag-rich compounds. In this model, each octahedral hole is comprised of a mixture of Ag^+, Bi^{3+} and vacancies, with a different ratio of these species in layers 1 and 2. All combinations of these species and vacancies in each layer is shown in Fig. 4(a), with each point representing a distinct material. The stoichiometries that lead to the smallest unit cells, and which are therefore the most thermodynamically probable, are the Ag_3BiI_6, Ag_2BiI_5, $AgBiI_4$ and $AgBi_2I_7$ compounds. These match the common stoichiometries reported (Fig. 2a). It was on this basis that Turkevych *et al.* proposed to call these Ag-Bi-I compounds "rudorffites".[20] However, as described above, not all stoichiometries, especially the Bi-rich ones, adopt the $R\bar{3}m$ $NaVO_2$ structure (see also Table 1 for reported structures).

In an early report on $AgBi_2I_7$ for photovoltaics by Kim *et al.* in 2016, the authors proposed that the material had a $ThZr_2H_7$-type structure, consisting of [AgI_6] octahedra and [BiI_8] hexahedra.[22] However, [BiI_8] hexahedra are unusual. Subsequently, Yan and co-

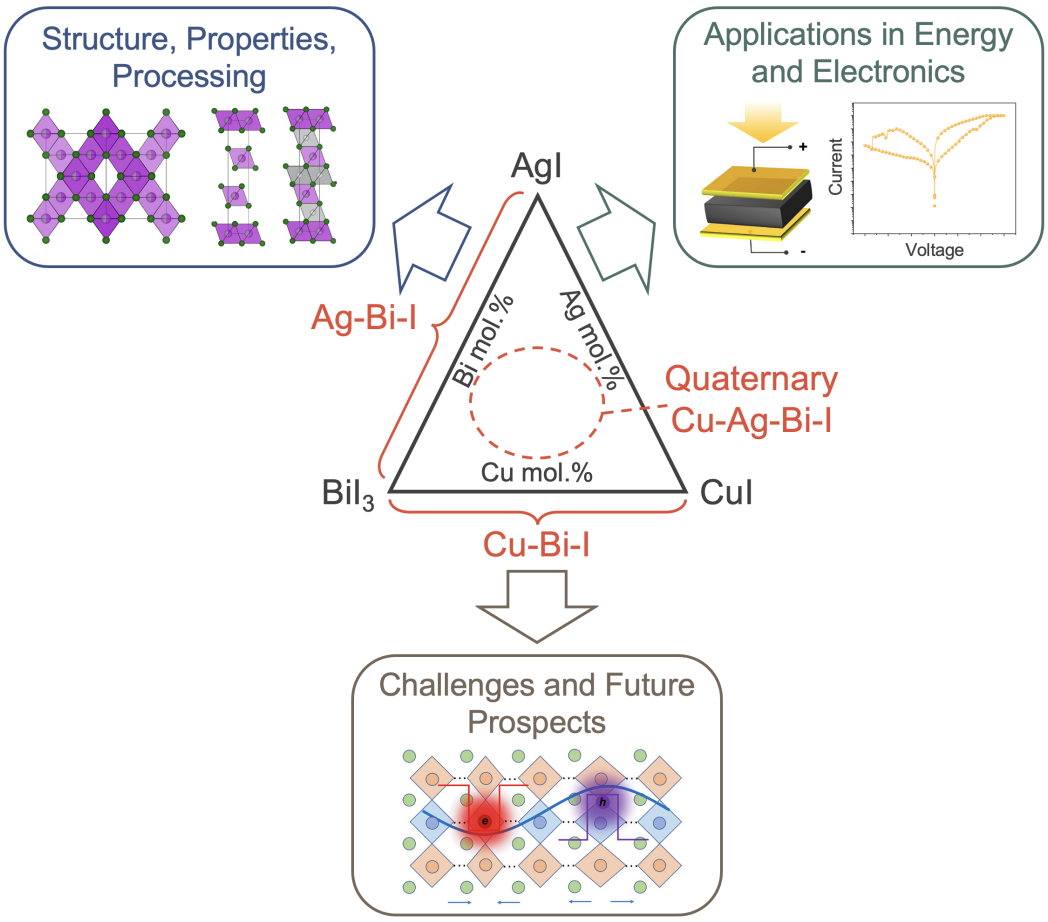

Figure 1: Overview and structure of this Full Critical Review. The materials focused on are ternary Ag-Bi-I and Cu-Bi-I semiconductors, along with quaternary Cu-Ag-Bi-I semiconductors, along with derivatives from compositional engineering. This review focuses on the crystal structure and properties, with a brief discussion of the processing, and followed by the applications of these materials in energy and electronic devices (solar cells, indoor photovoltaics, photodetectors, X-ray detectors and memristors). We finish with a discussion of current challenges, open questions and future opportunities. Structures shown inset of "Structure, Properties, Processing" box reproduced under the terms of the CC-BY license from Ref.[33] Copyright 2021, The Authors. Figures inset in applications box reproduced with permission from Ref.[34] (Copyright 2020, American Chemical Society) and Ref.[35] (Copyright 2022, Royal Society of Chemistry). In the outlook box, the image was reproduced under the terms of the CC-BY-NC license from Ref.[36] Copyright 2021, The Authors.

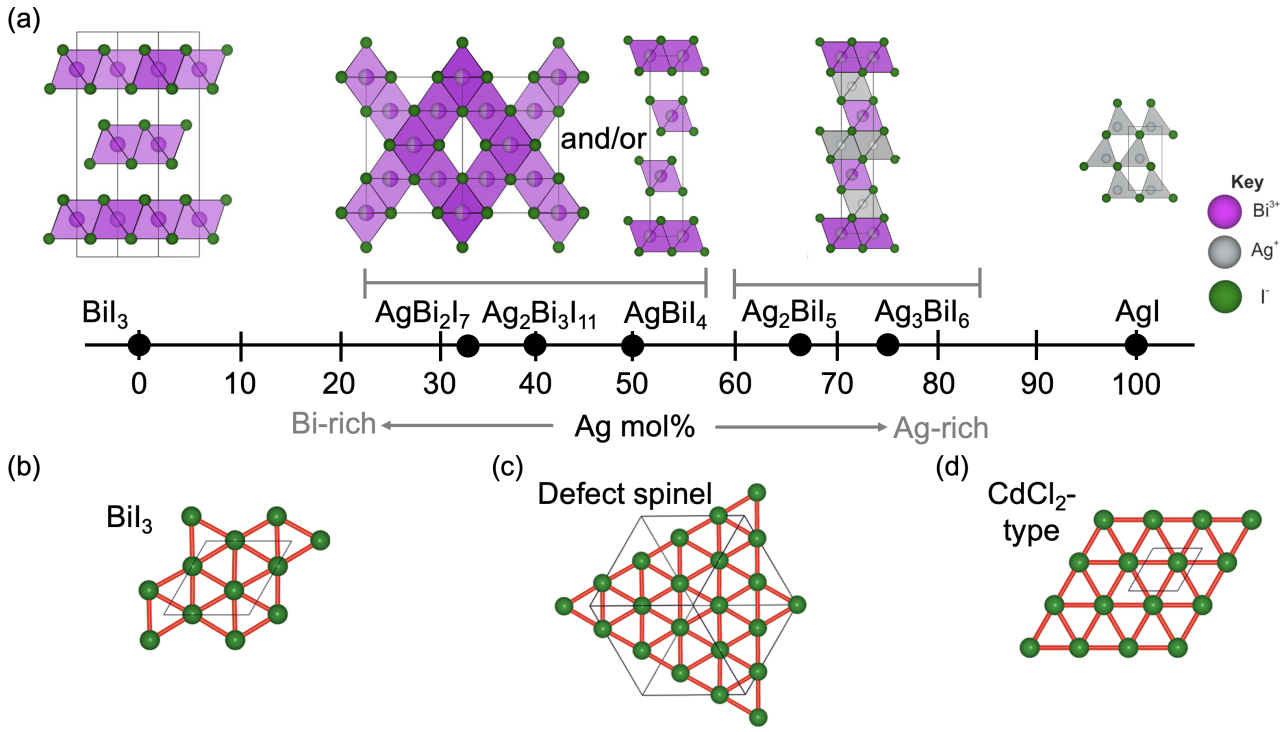

Figure 2: (a) Influence of stoichiometry on the structure of $Ag_aBi_bI_{a+3b}$ compounds. Adapted with permission under the terms of the CC-BY license from Ref.[33] Copyright 2021, The Authors. Iodide sub-lattice of (b) BiI_3, (c) $AgBiI_4$ (defect spinel structure), and (d) $AgBiI_4$ ($CdCl_2$-type structure). Reproduced under the terms of the CC-BY license from Ref.[44] Copyright 2017, The Authors.

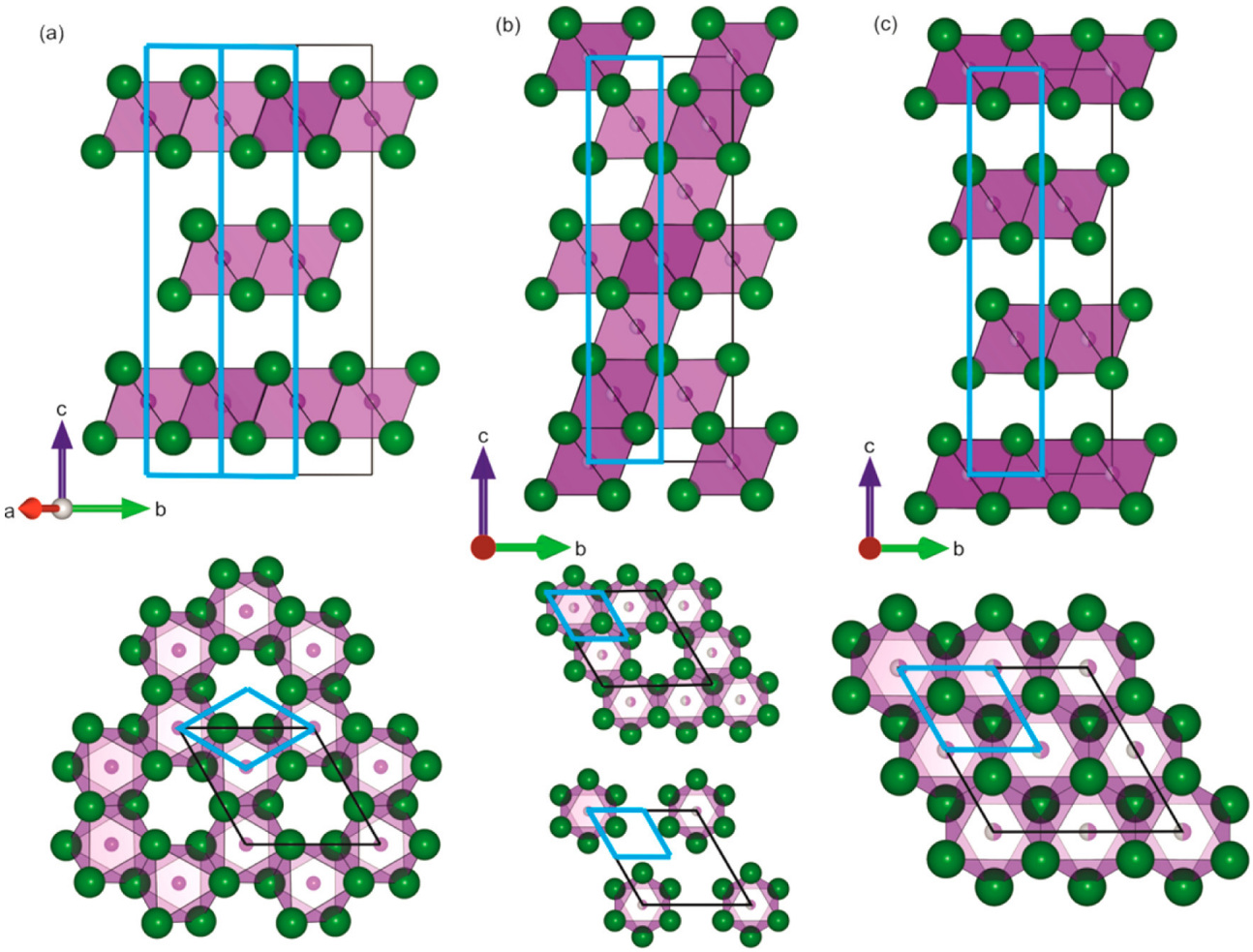

Figure 3: Comparison of the crystal structures of (a) BiI_3, (b) $AgBiI_4$ with the defect spinel structure, and (c) $AgBiI_4$ with the $CdCl_2$-type structure. Reproduced under the terms of the CC-BY license from Ref.[44] Copyright 2017, The Authors.

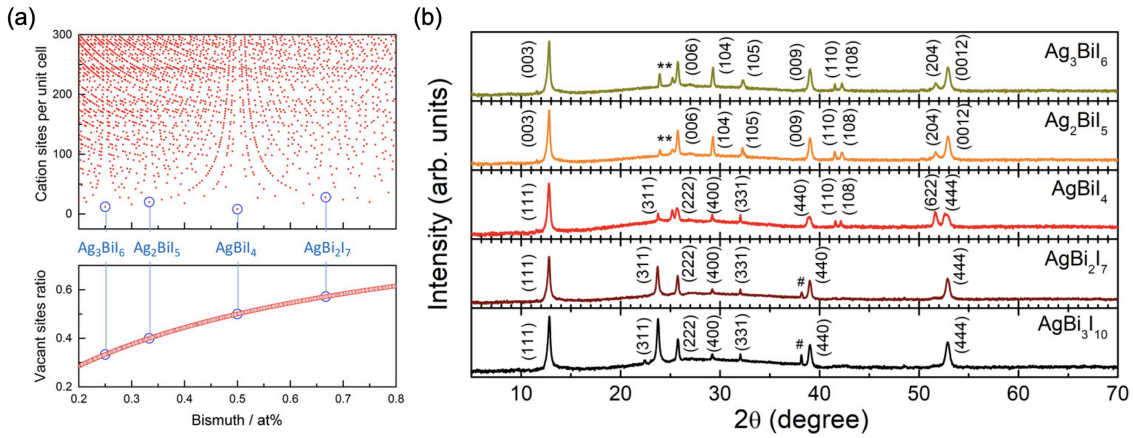

Figure 4: (a) Variation in the number of cation sites per unit cell (top) and vacant sites ratio with the fraction of cations that are bismuth.[20] (b) XRD patterns of $Ag_aBi_bI_{a+3b}$. Unreacted AgI and BiI_3 are marked with asterisk (*) and hash (#) symbols, respectively.[52] Part (a) reproduced with the permission from Ref.[20] Copyright 2017, Wiley. Part (b) reproduced with the permission from Ref.[52] Copyright 2021, American Physical Society.

Table 1: Crystal structures of ternary Ag-Bi-I, Cu-Bi-I and quaternary Cu-Ag-Bi-I compounds compared with their precursors: AgI, BiI_3 and CuI.[33] HCP = hexagonal close packed, CCP = cubic close packed. Note that Sansom *et al.* also believe that $AgBi_2I_7$ and $Ag_2Bi_3I_{11}$ could also have the twinned $CdCl_2$ structure.[33]

System	Compound	Unit Cell	Space Group	Octahedral Motif	Octahedral Site Occupancy (%)	Tetrahedral Sites	Iodide Sublattice	Impurity	Refs
binary	AgI	hexagonal	$P6_3mc$	none	n/a	wurtzite (3D)	HCP	n/a	[53]
binary	BiI_3	trigonal	$R\bar{3}$	BiI_3-type (2D)	33	none	HCP	n/a	[54]
binary	CuI	cubic	$F\bar{4}3m$	none	n/a	zinc blende (3D)	CCP	n/a	[55]
ternary	$AgBi_2I_7$	cubic	$Fd\bar{3}m$ (3D)	spinel (3D)	43	none	CCP	BiI_3	[17,33,50,52]
ternary	$Ag_2Bi_3I_{11}$	cubic	$Fd\bar{3}m$ (3D)	spinel (3D)	45	none	CCP	n.r.	[33,50]
ternary	$AgBiI_4$	cubic	$Fd\bar{3}m$ (3D)	spinel (3D)	50	none	CCP	Ag_2BiI_5	[16,33,44,52]
ternary	$AgBiI_4$	small trigonal	$R\bar{3}m$ (2D)	$CdCl_2$ (2D)	50	none	CCP	Ag_2BiI_5	[33,44,52]
ternary	Ag_2BiI_5	small trigonal	$R\bar{3}m$ (3D)	$NaVO_2$ (3D)	60	none	CCP	AgI	[17,20,44,50,52]
ternary	Ag_3BiI_6	small trigonal	$R\bar{3}m$ (3D)	$NaVO_2$ (3D)	66	none	CCP	AgI	[16,20,44,52]
ternary	$CuBiI_4$	cubic	$Fd\bar{3}m$ (3D)	spinel (3D)	25	antifluorite (3D)	CCP	CuI + BiI_3	[19,33]
ternary	$CuBiI_4$	small trigonal	$R\bar{3}m$ (2D)	$CdCl_2$ (2D)	25	antifluorite (3D, layered ordering)	CCP	CuI + BiI_3	[33]
quaternary	$CuAgBiI_5$	large trigonal	$R\bar{3}m$	spinel (3D)	40	$CuAgBiI_5$ (2D)	CCP	n/a	[33]
quaternary	Cu_2AgBiI_6	small trigonal	$R\bar{3}m$	$CdCl_2$ (2D)	33	antifluorite (3D, layered ordering)	CCP	n/a	[28]

workers[49] performed computational studies to show that $AgBi_2I_7$ cannot adopt the $ThZr_2H_7$-type structure with [BiI_8] hexahedra, as it was found to be thermodynamically unstable. Rather, the defect spinel structure is much more likely.

Finally, a current challenge is that the stoichiometry reported for Ag-Bi-I compounds is usually based on the molar ratio of the precursors used in solution processing. However, it is difficult to clearly distinguish between these stoichiometries because of the high degree of similarity in their X-ray diffraction (XRD) patterns. For example, in the series of Ag-Bi-I compounds shown in Fig. 4(b),[52] all Ag-poor compounds have (111), (311), (222), (400), (331), (440) and (444) peaks that are all at similar Bragg angles. The Ag-rich compounds have (003), (006), (104) and (009), etc. peaks in similar positions, and these in turn are in similar positions to those of their Ag-poor counterparts (e.g., (111) peak for Ag-poor and (003) peak for Ag-rich compounds). Compounding the difficulties in distinguishing between stoichiometries is the presence of phase-impurities in many Ag-poor and Ag-rich materials, such as BiI_3 (denoted in Fig. 4(b) by a #), and AgI (denoted in Fig. 4(b) by an *),[20,56] as shown in Table 1. Therefore, it is essential to directly measure the stoichiometry both in the bulk and at the surface, such as through Rutherford Backscattering Spectrometry and X-ray photoemission spectroscopy, respectively.[57] Identifying phase separation, or how uniformly distributed the Ag and Bi cations are will be essential to understand and control the reproducibility of films.

2.1.2 Electronic Structure and Optical Properties

Fig. 5 shows the band structure and density of states (DOS) of Ag-Bi-I compounds from first-principles density functional theory (DFT) calculations. Fig. 5(a)[58] and (b)[56] show that the Ag 4d and I 5p orbitals are the main contributors to the upper valence band (VB), whilst the lower conduction band (CB) is mainly comprised of I 5p and Bi 6p orbitals for all Ag-Bi-I semiconductors. From these DFT calculations, it can be seen that the curvature of the

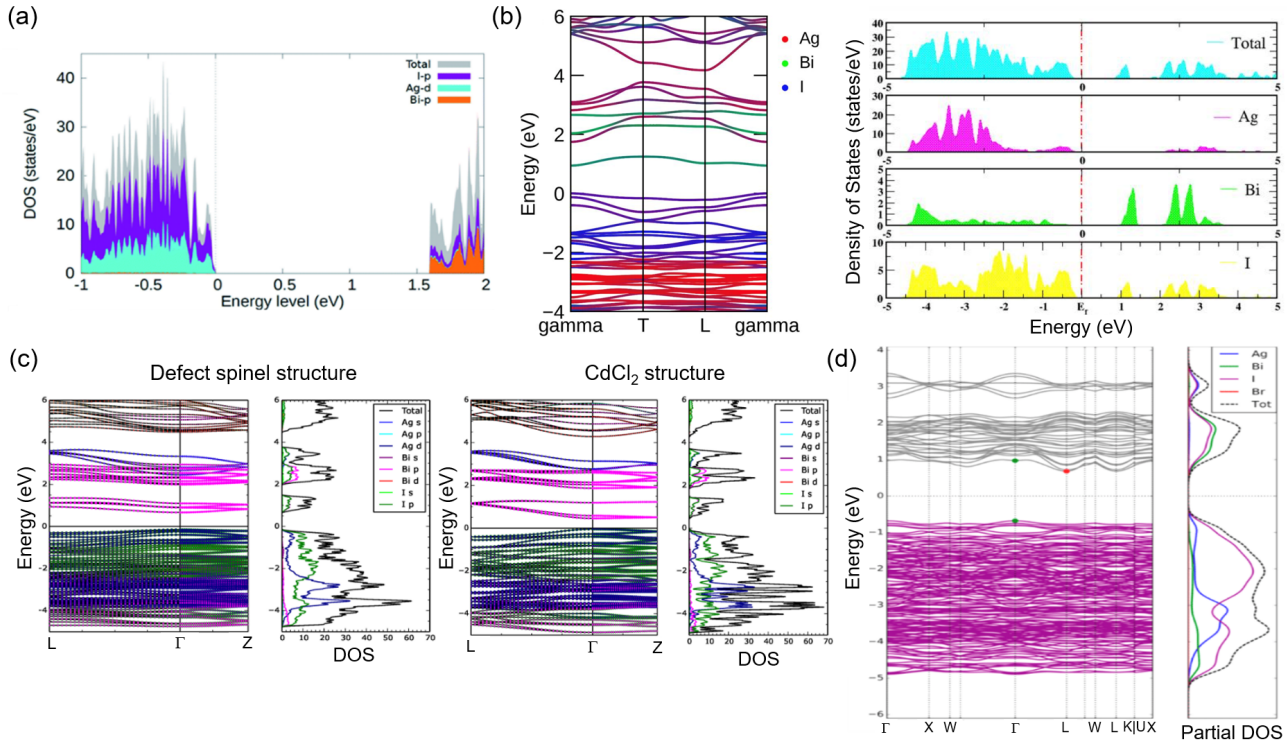

Figure 5: Total and orbital-projected density of states of (a) Ag_2BiI_5, (b) Ag_3BiI_6, (c) $AgBiI_4$ in the defect spinel (left) and $CdCl_2$-type (right) structures, and (d) $AgBi_2I_7$ obtained from DFT calculations. For (b), (c) and (d), the band diagrams are also shown. Part (a) reproduced with the permission from Ref.[58] Copyright 2021, The Royal Society of Chemistry. Part (b) reproduced under the terms of the Creative Commons CC-BY license from Ref.[56] Copyright 2021, The Authors. Part (c) reproduced under the terms of the CC-BY license from Ref.[44] Copyright 2017, The Authors. Part (d) reproduced with permission from Ref.[59] Copyright 2019, American Chemical Society.

band extrema for Ag-rich Ag_3BiI_6 in Fig. 5(b) is much larger than the curvature of $AgBiI_4$ (Fig. 5(c))[44] and Ag-poor $AgBi_2I_7$ (Fig. 5(d)).[59] As the electron (m_e*) and hole (m_h*) effective masses are inversely proportional to the curvature of the band edges,[60] this would suggest that Ag_3BiI_6 has lower effective masses than Ag-poor materials, and therefore higher upper limits in mobility. Lower effective masses also have beneficial ramifications on other important properties, such as longer diffusion lengths, lower exciton binding energies, and smaller capture cross-sections for charged defect states through lower Sommerfeld factors.[2,31] Indeed Crovetto *et al.* found that Ag_3BiI_6 has low effective masses down to $0.4m_0$ for both electrons and holes along the *ab* plane (where m_0 is the rest mass of an electron),[38] while

$AgBiI_4$ has electron and hole effective masses of 0.6–0.8m_0 and 0.9–1.0m_0, respectively, for the cubic defect-spinel polymorph, and 1.3m_0 and 1.8m_0, respectively, for the $CdCl_2$-type polymorph.[44]

Furthermore, Ag-Bi-I semiconductors have shown good optical absorption coefficients (α) $>10^4$ cm^{-1} in the visible wavelength range,[61] although the exact value for α varies with the stoichiometry.

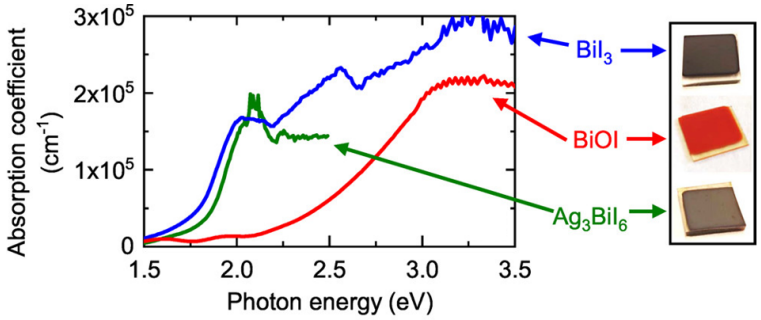

Figure 6: Absorption coefficient of Ag_3BiI_6 thin films compared with BiI_3 and BiOI. Reproduced with permission from Ref.[38] Copyright 2020, American Chemical Society.

Absorption coefficients have been reported to reach as high as 10^5 cm^{-1} for Ag_3BiI_6 prepared by iodizing sputter-deposited Ag_2Bi films (Fig. 6).[38] However, currently, the absorption spectra of Ag-Bi-I thin films have been found to have long Urbach tails (*e.g.*, see Fig. 6).[44,61] This is indicative of a relatively high level of crystal structure disorder. This disorder may be caused by an inhomogeneous distribution of the Ag^+ and Bi^{3+} cations, regions of low crystallinity in the solution-processed samples, strong electron-phonon coupling, or point defects, such as Bi_{Ag} antisites.[62,63]

2.1.3 Band Positions

The band positions of Ag-Bi-I compounds are shown in Fig. 7 in comparison with common electron transport layers (ETLs) and hole transport layers (HTLs) used in solar cells. It can be seen that these band positions are influenced by the stoichiometry. The upper VB

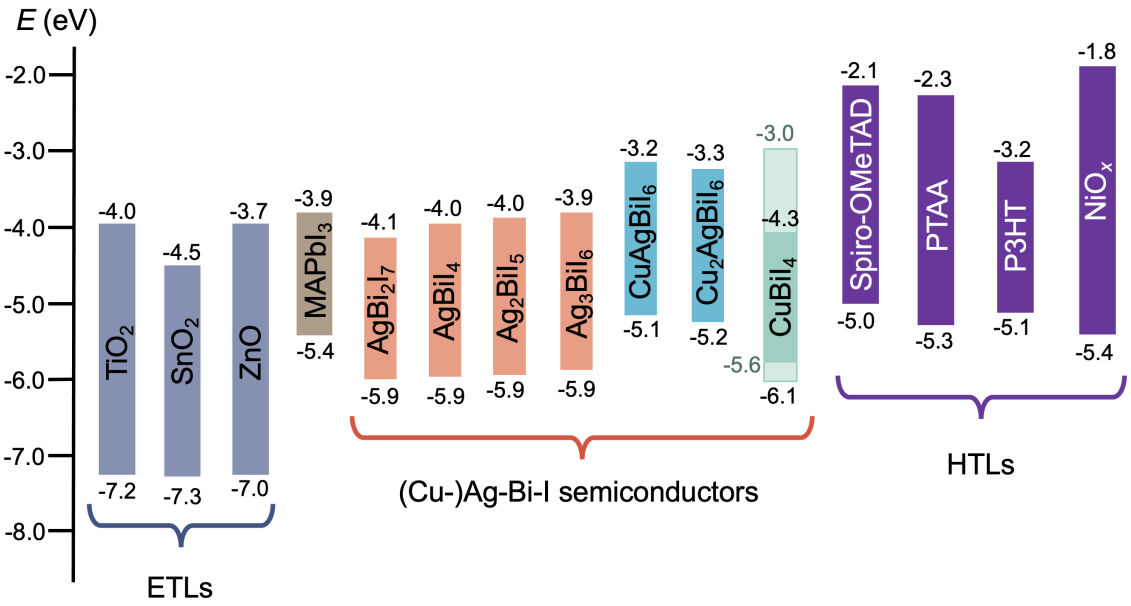

Figure 7: Band positions of Ag-Bi-I, $CuBiI_4$, and quaternary Cu-Ag-Bi-I compounds compared to the energy extrema for common electron (ETLs) and hole transport layers (HTLs) used in solar cells. Band positions obtained from Ref.[31,64–72] Please note that Lu *et al.* and Zhang *et al.* reported different electron affinities and ionization potentials for $CuBiI_4$ (3.0 and 5.7 eV by Lu *et al.*, and 4.3 and 6.1 eV by Zhang *et al.*[66,67]

is mainly comprised of Ag 4d and I 5p states (with a small contribution from Bi 6s states), whereas the lower CB is mainly due to Bi 6p and I 5p states (Fig. 5). Given that Ag 4d is closer to vacuum level than Bi 6s, the increased Ag 4d character of the VB in Ag-rich compounds may cause the upwards shift in the valence band maximum (VBM).[52,64] By contrast, the conduction band minimum (CBM) shifts down for Bi-rich compositions (Fig. 7), and this may be due to the strong Bi 6p character of the lower CB.[64] In particular, as a heavy-metal element, Bi has strong spin-orbit coupling, and a stronger Bi 6p character may led to the CB density of states shifting down into the bandgap as a result. The E_g values of Ag-Bi-I compounds can change from 1.86 eV to 1.95 eV when the stoichiometry changes from Ag-poor to Ag-rich.[52,64] Despite the strong influence of stoichiometry on the band positions of Ag-Bi-I compounds, DFT calculations have shown that a direct bandgap is maintained in both the defect-spinel and $CdCl_2$-type polymorphs of $AgBiI_4$ (Fig. 5c), as well as in Ag_2BiI_5 (Fig. 5a). In both cases, the VBM and CBM remain at the Γ point. However, in $AgBi_2I_7$,

the bandgap becomes indirect (Fig. 5d), as the VBM remains at the Γ point, but the CBM shifts to the L point.[59]

2.1.4 Charge-Carrier Properties

An important question is whether the nature of charge-carriers in Ag-Bi-I compounds is more free-carrier-like, or more exciton-like. The exciton binding energy (E_b) of Ag-Bi-I materials was studied by Buizza *et al.* and Ghosh *et al.*[27,62] Although both groups used Elliott model fitting to their measured optical absorption spectra to obtain E_b, the values determined were very different. Buizza *et al.* obtained an E_b value of 27 meV for $AgBiI_4$ (implying most charge-carriers are free),[62] whereas the value determined by Ghosh *et al.* for the same material was 260 meV (implying excitons dominate the material).[27] In the same work and using the same method, Ghosh *et al.* determined the E_b for Ag_2BiI_5 to be 150 meV.[27] More detailed studies are therefore needed to understand the nature of charge-carriers in Ag-Bi-I materials, such as through magneto-optical spectroscopy measurements,[73] measurements of the fluence-dependence of the photoluminescence (PL) peak intensity, or calculations of E_b using a high level of theory. Nevertheless, the E_b values found so far are higher than in LHPs (approximately 20 meV or lower).[73] This may be due to the higher effective masses found in Ag-Bi-I (ranging from $0.4m_0$ to $1.8m_0$,[38,44] see Section 2.1.2, compared to ca. 0.1–$0.2m_0$ for 3D LHPs[2]).

Another important factor that complicates charge-carrier transport in Ag-Bi-I materials is the strong interaction between charge-carriers and phonons that lead to carrier localization, in which the wavefunction of the charge-carrier is confined to a unit cell or smaller.[62,63] As a result, charge-carriers can only move in the bulk of the compound through thermally-activated hopping between adjacent sites, which severely limits the mobility.

At the same time, it has been found that the stoichiometry can influence the opto-electronic properties. A comparison beteween $AgBiI_4$ and Ag_2BiI_5 made by dynamic hot

casting showed that as the fraction of Ag increased, there was an increase in the mobility from 1.7±0.3 cm^2 V^{-1} s^{-1} to 2.3±0.3 cm^2 V^{-1} s^{-1} (as determined from Hall measurements), along with an increase in the charge-carrier lifetime from 87±5 ns to 133±11 ns (as determined from transient absorption spectroscopy).[27] Turkevych *et al.* suggested that the longer charge-carrier lifetime and higher mobility in the Ag-rich compounds may arise from fewer recombination centers (*e.g.*, Bi^0 - see Section 3.1 for a more detailed discussion).[20]

2.1.5 Compositional Engineering

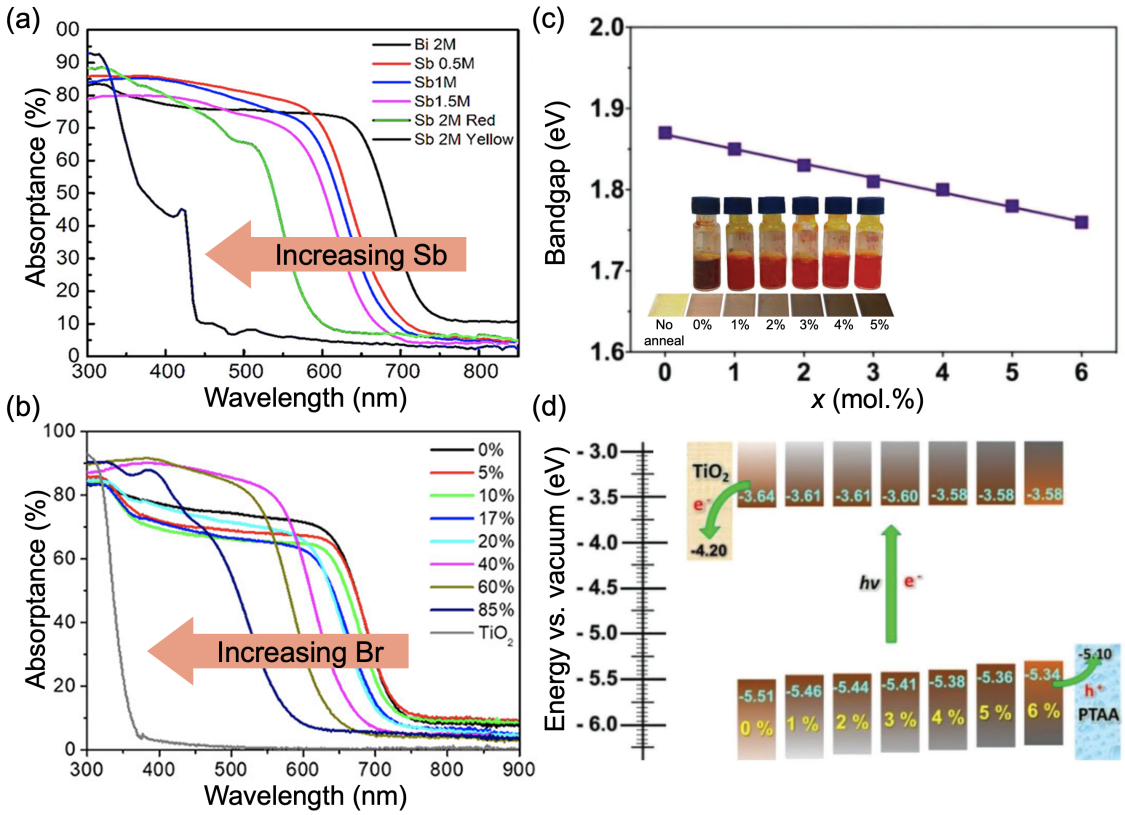

Figure 8: Compositional engineering in Ag-Bi-I. Absorbance of $AgBi_2I_7$ films with increasing (a) Sb content, and (b) Br content. Part (a) reproduced under the terms of the CC-BY license from Ref.[26] Copyright 2020, The Authors. Part (b) reproduced with permission from Ref.[59] Copyright 2019, American Chemical Society. Effect of S alloying in the anion site of Ag_3BiI_6 on (c) the optical bandgap, E_g (photographs of precursor solutions and films inset) and (d) band positions. Parts (c) and (d) reproduced with permission from Ref.[74] Copyright 2019, Wiley.

Tuning the composition of materials is an effective method to adjust their properties. For example, mixing together different cations into the cuboctahedral site of LHPs has led to materials that are more stable and efficient than the prototypical methylammonium lead iodide ($MAPbI_3$).[75] Similarly, there have been several works investigating the inclusion of additives in Ag-Bi-I materials to tune their optical properties and defect density.[32] Fig. 8 shows the examples of alloying Sb into the pnictogen-site of $AgBi_2I_7$,[26] and Br[59] and S[74] into the anion site of $AgBi_2I_7$ and Ag_3BiI_6, respectively. In all three examples, XRD and composition measurements confirmed the incorporation of the additives into the materials.[26,59,74] Furthermore, the thin film absorbers in all cases were prepared by spin coating the precursor solution (using DMF [*N*,*N*-dimethylformamide], DMSO [dimethyl sulfoxide], or a mixture of both) inside a glovebox, and annealing at 90–150 °C.[26,59,74]

Incorporating Sb into $AgBi_2I_7$ results in an increase in the indirect bandgap from 1.61 eV (0% Sb) to 1.98 eV (100% Sb), as shown in Fig. 8a. Computational analyses showed that this was due to the higher spin-orbit coupling for Bi compared to Sb. The pnictogen valence p orbitals make a strong contribution to the density of states in the CB, and replacing Bi with Sb results in the density of states extending less into the bandgap due to reduced spin-orbit coupling.[26] Zhu *et al.* also investigated the effects of pnictogen chemistry on the Urbach tail of these $AgBi_{2-x}Sb_xI_7$ films by calculating the "near edge absorptivity ratio" (NEAR). NEAR is defined as the square root of α at the bandgap divided by α at an energy 2% larger the bandgap, with the value of 2% being arbitrarily chosen. It was found that alloying Sb into $AgBi_2I_7$ leads to a reduction in the NEAR value,[26] which was attributed to a reduction in the density of defect states in the bandgap.[76]

Similarly, incorporating Br into the anion site of $AgBi_2I_7$ broadened the bandgap (Fig. 8b).[59] Furthermore, Wu *et al.* found that alloying 10 at.% Br in $AgBi_2I_7$ led to more uniform films with a lower pinhole density.[59] The photostability was also found to be improved, and this could be due to Br alloying improving film formation to give rise to lower defect densities.[59]

At the same time, the bandgap of Ag-Bi-I materials, at approximately 1.9 eV, is too wide for single-junction photovoltaic applications under 1-sun illumination. It is therefore important to also find routes to lower the bandgap, and Pai *et al.* reported that this can be achieved through S incorporation. As can be seen from Fig. 8c, increasing the fraction of S in the precursor solution resulted in a reduction in the bandgap of Ag_3BiI_6 from 1.87 eV (0% S) to 1.76 eV (6 at.% S), leading to darker films. This reduction in bandgap came about due to a lowering of the ionization potential (Fig. 8d), which was likely due to an increase in the S 3p character of the VBM.[74] That is, the S 3p orbital has a lower energy than the I 5p orbital, and is closer to the Ag 4d orbital energy. The upper VB is dominated by the hybridization between Ag 4d and anion p orbitals, and increasing the S 3p character would increase the repulsion between Ag 4d and the anion p orbital, leading to an antibonding orbital at the VBM with lower energy, thus shifting the VBM closer to vacuum level. The effects on photovoltaic performance are discussed later in Section 3.1.4.

The inclusion of Cs additives to $AgBiI_4$ by solution processing has also been investigated.[77] From XRD measurements, it was found that these materials adopted a cubic defect-spinel structure, and that including 1% and 5% Cs^+ to the precursor solution led to an improvement in crystallinity, along with an increase in absorbance, PL intensity and PL lifetime. Further increasing the concentration of Cs^+ to 10% in the precursor solution resulted in a phase impurity appearing in the resulting films.[78] In these studies into Cs additives, it is uncertain as to where in the lattice Cs^+ is incorporated, but Wang *et al.* speculate that Cs^+ and other alkali additives may occupy interstitial sites.[77]

The inclusion of Cs and Sb additives into Ag_2BiI_5 has also been investigated,[77,79] and it was found that larger grains could be formed, especially with the use of Sb additives. As a result, the Urbach energy was decreased, accompanied with a reduction in the bandgap.[79]

2.1.6 Materials Stability

Ag-Bi-I compounds have a negative formation enthalpy under ambient conditions, meaning that they are thermodynamically stable.[56] Given that they are free from organic constituents, Ag-Bi-I compounds have demonstrated phase-stability in ambient air (30% to 70% relative humidity).[34,40] However, there are noticeable impurity issues in Ag-Bi-I materials that can accelerate decomposition. Light illumination can also increase the degradation rate in these materials. In this section, we will discuss how these impurities form, and the processes by which they can cause film degradation. Here, the focus is on materials stability and degradation products, and this discussion is carried on in Section 3.1 on photovoltaic device stability.

Many groups have reported Ag-Bi-I thin films to be phase-stable in ambient air. Kulkarni *et al.* synthesized Ag-Bi-I films with different stoichiometries by solution processing (see Fig. 9a), and found that when there was a high fraction of the AgI phase impurity, the stability of the resulting photovoltaic devices worsened (Fig. 9b).[56] Curiously, bright dots were seen in the secondary electron images of all of the films (see Fig. 9c for an example), and these bright dots have been widely reported in Ag-Bi-I thin films.[38,40,56,74] Accounts of the causes, behavior and consequences of these bright dots have varied in different reports. Kulkarni *et al.* and Pai *et al.* both believe that these bright dots are due to aggregates of the Ag-rich phase,[56] such as AgI.[74] Crovetto *et al.* reported that these spots are not present initially in Ag_3BiI_6 when imaged in scanning electron microscopy (SEM), but appear within seconds of electron beam irradiation.[38] By contrast, we have, at times, observed them to be present initially but disappear over time under beam exposure. Kulkarni *et al.* reported that they only found bright dots to be present at the Ag-Bi-I/TiO_2 interface for the $AgBi_2I_7$ and Ag_2BiI_5 samples, whereas the Ag_3BiI_6 devices had bright dots at the Ag-Bi-I/P3HT/Au interfaces and layers (where P3HT is poly[3-hexylthiophene-2,5-diyl]). This was believed to indicate an accumulation of AgI at the hole-extracting electrode, resulting in poorer photovoltaic performance. Kulkarni *et al.* also believed that the excess of Ag and I present in

these aggregates resulted in the release of Ag^+ cations and I^- anions that migrated through to the top Au electrode, enhancing the degradation of the device.[56] Notably, this decrease in performance only occurred after incorporating the Ag-Bi-I film into a photovoltaic device. Ag_3BiI_6 films made into devices fresh *vs.* after storing in air for 2 weeks before making into devices exhibited very similar performance and stability (Fig. 9d). This suggests that ionic species are only released after fabricating the interfaces with the HTL and Au, and may also be accentuated by the application of an electric field.[56] Zhu *et al.* also observed that Ag-Bi-I films remained stable under storage without an electric field applied, despite the presence of bright dots on the surface of the films.[40]

2.2 Cu-Bi-I Compounds

$CuBiI_4$ and Cu_2BiI_5 were first reported decades ago ,[80] with the structure for $CuBiI_4$ later being solved by the same author[19]. Despite this, the first $CuBiI_4$ solar cell was only published in 2018.[67] There are a handful of works on Cu-Bi-I semiconductors for photovoltaic applications.[66,67,81] Cu-Bi-I compounds have bandgaps in the visible wavelength range. In addition, Cu-Bi-I compounds have promising photo- and air-stability, in which the photovoltaic performance was maintained after 30 days of air and 1-sun light exposure. Apart from $CuBiI_4$, there have also been reports on Cu_3BiI_6 solar cells, which exhibited little hysteresis.[82] But currently, $CuBiI_4$ is the material that has been investigated the most, and we will therefore focus on this compound. This section covers the crystal structure, band structure, and optoelectronic properties of $CuBiI_4$.

2.2.1 Crystal Structure of Cu-Bi-I

Structural investigations into ternary Cu-Bi-I compounds have also mostly been made using single crystal and powder samples.[19,28,80,83] Fourcroy *et al.* prepared $CuBiI_4$ single crystals by melt crystallization.[19] Sansom *et al.* and Das *et al.* also used melt crystallization,

but prepared powders instead. All three groups reported the use of rapid quenching in water from a temperature of 350 °C instead of slow cooling to room temperature.[19,28,80,83] Sansom *et al.* found that, unlike quaternary Cu-Ag-Bi-I materials prepared using similar methods (see later in Section 2.3.2), the $CuBiI_4$ crystals were too fragile to retrieve, and so relied on powder XRD to solve the structure.[28]

Like the Ag-Bi-I system, $CuBiI_4$ also has a ccp I sub-lattice, and $CuBiI_4$ has the structure shown in Fig. 10.[19] But unlike Ag-Bi-I compounds, Cu^+ occupies tetrahedral holes rather than octahedral holes because of the smaller ionic radius of Cu^+ (74 pm) than Ag^+ (129 pm).[84] $CuBiI_4$ still has 1/2 of the octahedral holes filled, but these are occupied by Bi^{3+} and vacancies with 50% occupancy each.[19,33,83] Cu^+ is disordered over all tetrahedral sites, with 9-18% occupancy each, and the BiI_6 octahedra are edge-sharing with the CuI_4 tetrahedra, forming a 3D network (Fig. 10)[19,33,83]. However, Cu^+ occupies an extra tetrahedral site compared to spinel structures, and therefore does not have a spinel tetrahedral motif, even though its octahedral motif is spinel.[33] Cu^+ also occupies tetrahedral holes in CuI, but unlike AgI, the I sub-lattice in CuI is ccp (Fig. 10).[33]

Beyond $CuBiI_4$, Cu_2BiI_5 has been reported to have a hexagonal unit cell.[19] Ramachandran *et al.* prepared thin films of Cu_2BiI_5 and, by comparing their measured pattern with reference patterns, agreed that this material has a hexagonal structure.[85] However, more detailed structural analysis using high-quality powder or single-crystal XRD patterns should be made. Baranwal *et al.* also reported the synthesis of Cu_3BiI_6,[82] but the structure of this material has not yet been solved.

Apart from these structures, Wang *et al.* also suggested, based on computational analyses, that $CuBiI_4$ could form two $P\bar{1}$ structures, as well as one $P2_1/m$ structure (Fig. 11a).[86] However, these structures have yet to be realized experimentally.

2.2.2 Optoelectronic Properties and Band Positions

From the computational work by Wang *et al.*, $CuBiI_4$ with the theoretical $P\bar{1}$ and $P2_1/m$ structures were predicted to have high absorption coefficients exceeding 10^5 cm^{-1} (Fig. 11b).[86] Wang *et al.* went further to predict the potential of these materials as photovoltaics by calculating the SLME from the computed absorption spectra and proximity of the first direct transition to the optical bandgap.[87] These calculations showed that all three $CuBiI_4$ structures have SLMEs in the range of 17–20% under 1-sun illumination.[86] These values fall below those of silicon and other established thin film solar absorbers, which is partly due to the wide bandgap of the materials (close to 2 eV).[86] On the other hand, these bandgaps are close to the ideal value for indoor photovoltaics (1.9 eV), and the high absorption coefficients suggests that these materials could have higher SLMEs under indoor light spectra.

Experimentally, a handful of groups have reported the synthesis of $CuBiI_4$ thin films by spin-coating,[66,81] as well as by iodizing sputter-deposited Bi/Cu alloys.[67] The absorption spectra of $CuBiI_4$ thin films prepared by Hu *et al.* is shown in Fig. 11c, where it can be seen that the absorption onset remains the same despite changing the precursor concentration and therefore the thickness of the films. However, the direct bandgap found was determined to be 2.67 eV by Hayase and co-workers (Fig. 11d),[66] which would imply a very low electron affinity (Fig. 7). It should be noted that the diffraction pattern of these Cu-Bi-I films did not match well with the reference pattern for $CuBiI_4$, with some peaks offset and many peaks missing (possibly due to preferred orientation).[66] In a more recent work, Qu *et al.* and Zhang *et al.* reported a bandgap of 1.84 eV,[67,81] with an electron affinity more in line with other Cu-Ag-Bi-I semiconductors at -4.3 eV (Fig. 7). Consistent with these reports, Qu *et al.* measured a PL peak at 683 nm wavelength (1.82 eV).[81]

2.2.3 Charge-Carrier Properties

Hayase and co-workers found that as the thickness of $CuBiI_4$ thin films increased, both

the Hall mobility (Table 2) and PL lifetime (Fig. 11e) increased, owing to an increase in grain size (Table 2) and reduced non-radiative recombination.[66] It should be noted, however, that the Hall mobility values reported are substantially higher than expected from a solution-processed thin film. For example, Sansom *et al.* reported that the quaternary compound, Cu_2AgBiI_6, in polycrystalline thin film form has a mobility of only 1.7 cm^2 V^{-1} s^{-1}.[28] More in-depth investigations into the mobility of $CuBiI_4$ should be made, especially for single crystal samples to determine the upper limits in mobility.

The charge-carrier properties of $CuBiI_4$ were also examined by transient photovoltage (TPV) measurements.[88] From these, a positive signal was observed, implying that the films were n-type. The recombination lifetime of $CuBiI_4$ thin films was found to exceed 3 ns, which are consistent with the PL lifetime measurement from Hayase and co-workers (Fig. 11e), and imply that the material is suitable for further efforts to develop them into photovoltaics.[89]

Table 2: Effect of the precursor concentration on the charge-carrier properties of $CuBiI_4$ reported by Hayase *et al.*[66]

Precursor Solution Concentration (M)	0.4	0.5	0.6	0.7
Thickness (nm)	150	196	245	303
Average grain size (nm)	130	191	242	300
Mean charge-carrier lifetime (ns)	0.23	0.82	1.67	3.03
Carrier concentration (cm^{-3})	2.47×10^{14}	5.75×10^{14}	6.03×10^{14}	6.56×10^{14}
Hall mobility (cm^2 V^{-1} s^{-1})	33.3	48.2	88.4	110
Resistivity (Ω cm)	7.59×10^2	2.25×10^2	1.17×10^2	0.86×10^2

2.2.4 Materials Stability

There have been some stability studies on $CuBiI_4$ thin films and powders (Fig. 12), with mixed conclusions. Sansom *et al.* synthesized phase-pure powders by heating BiI_3 and CuI powders in silica ampoules followed by rapid quenching. When samples were stored in air for 3 weeks at both room temperature and −20 °C, they were found to decompose to BiI_3 and CuI precursors. Cooling powders to −20 °C slowed this decomposition process. Sansom,

et al. concluded that $CuBiI_4$ is meta-stable.[28] This is consistent with reports of Fourcroy *et al.*, who stated $CuBiI_4$ only exists above 276 °C based on extensive exploratory synthesis within the $CuI-BiI_3$ phase space, although they did not comment on the degradation rate of quenched materials.[80] Using a similar synthesis method, Das *et al.* prepared a phase-pure ingot of $CuBiI_4$. They found powders exposed to ambient air with standard laboratory lighting for 10 days showed no signs of decomposition as observed via PXRD and thermal conductivity measurements. Furthermore, they found samples heated in air between 323 K to 398 K for 4 hours remained stable as measured using PXRD and UV-vis spectroscopy.[83] Hu *et al.* synthesised (111)-orientated $CuBiI_4$ thin films by combining spin coating with solvent vapour annealing. After exposing the thin films to air for 42 days, they found no change in the the XRD patterns as compared to freshly annealed films.[66] Ramachandran *et al.* claim to have synthesized Cu_2BiI_5 thin-films for use in photodetector devices. They compared XRD patterns of freshly annealed samples with thin films exposed to air for 30 days. The XRD patterns of the air-exposed samples showed changes in peak intensity ratios, along with the appearance/disappearance of a number of minor peaks.[85]

2.3 Quaternary Cu-Ag-Bi-I Compounds

2.3.1 Crystal Structure of Cu-Ag-Bi-I

Sansom *et al.* reported the exploration of five materials along the $AgBiI_4$-CuI solid solution line: $Cu_x(AgBi)_{1-x}I_4$ with $x = 0$ ($AgBiI_4$), 0.09 ($Cu_{0.4}AgBiI_{4.4}$), 0.2 ($CuAgBiI_5$), 0.33 (Cu_2AgBiI_6), 0.6 (Cu_6AgBiI_{10}), as shown in Fig. 13a.[28,33,62] The structures of $CuAgBiI_5$ and Cu_2AgBiI_6 were examined in detail from single crystal and powder XRD measurements.[28,33] $CuAgBiI_5$ was found to form a 3D defect spinel structure,[33] whereas Cu_2AgBiI_6 has a 2D $CdCl_2$-type structure (Fig. 13a).[90] This change in phase may account for the large change in lattice parameters and cell volume from $x = 0.2$ to $x = 0.33$ (Fig. 13b[62]).

Sansom *et al.* found that the single crystal XRD pattern of $CuAgBiI_5$ could be solved with

the 3D spinel octahedral motif. But unlike $AgBiI_4$, this structure cannot also be described by a twinned $CdCl_2$ structure.[33] Furthermore, Sansom *et al.* found from fitting the powder XRD pattern that the unit cell is not well described by a cubic unit cell, and instead transformed the cubic unit cell ($Fd\bar{3}m$) to a trigonal unit cell ($R\bar{3}m$) with an equivalent spinel octahedral motif, which is now comprised of two octahedral sites for the first and second layers (compare Fig. 13a with Fig. 3b).[33] From Rietveld refinement, both octahedral sites were found to be comprised of 42.1% Bi^{3+}, 41.4% Ag^+, and 16.5% vacancy. There are also two tetrahedral sites, one in layer 1 (with 3/4 of the octahedral holes occupied) and the other in layer 2 (with 1/4 of the octahedral holes occupied). Sansom *et al.* found that only the tetrahedral holes in layer 2 were occupied by Cu^+ with 17.3% occupancy.[33] Since only one of these tetrahedral holes are partially occupied, $CuAgBiI_5$ does not have a spinel *tetrahedral* motif, even though it has a spinel *octahedral* motif.

For Cu_2AgBiI_6, Sansom *et al.* found that the octahedral motif is $CdCl_2$-type, and the occupancies are 30.6% (Bi^{3+}), 34.7% (Ag^+), with the balance vacancies.[28] Cu^+ is disordered over all tetrahedral holes, with 17.9% occupancy.[28]

Beyond these detailed studies, there have also been reports of $CuAgBi_2I_8$ prepared by sputter depositing Bi, Cu and Ag, followed by heating in a I_2-rich gas environment (referred to as one-step gas-solid-phase diffusion-induced direct metal surface elemental reaction, or DMSER).[91] From thin film diffraction measurements, it is believed that this material has a defect spinel structure, with a space group of $Fd\bar{3}m$,[91] but there are no detailed investigations into the structure of this composition. Park *et al.* also investigated the incorporation of Cu^+ additives to Ag_2BiI_5 thin films prepared by powder melt synthesis, followed by solution processing of the powders.[58] However, the structure of these materials were also not studied in detail. Although Park *et al.* believed that Cu^+ substituted for Ag^+,[58] Cu^+ likely instead occupies tetrahedral sites, while Ag^+ fills octahedral holes, as described above.

2.3.2 Particular Considerations for the Synthesis of quaterany Cu-Ag-Bi-I Compounds

Single crystals, powders and polycrystalline thin films of quaternary Cu-Ag-Bi-I compounds have all been synthesized.[28,33,58,62,65,91,92] The detailed structural information discussed in Section 2.3.1 above was obtained from single crystal and powder X-ray diffraction. Unlike the synthesis of Ag-Bi-I and $CuBiI_4$ powders, which can be obtained by melt crystallization,[17,18,28] Sansom *et al.* reported that $CuAgBiI_5$ and Cu_2AgBiI_6 needed to be synthesized by solid-state reaction (at 350 °C for a few days) between the binary iodide precursors with fast quenching.[28,33] This was to avoid compositional inhomogeneities, which occur if a melt is formed or if the product synthesized is cooled down to room temperature slowly.[28,33] These complications may arise because of the mobile nature of the elements present, especially at elevated temperatures. In the synthesis of these Cu-Ag-Bi-I powders, Sansom *et al.* found that sufficiently large single crystals (ca. 20 μm along each dimension) could be obtained for single crystal diffraction measurements.[28,33] In contrast, Park *et al.* used melt crystallization by heating the CuI, AgI and BiI_3 precursor powders at 450 °C for 12 h.[58] At this temperature, BiI_3 melts (melting point of 409 °C), and acts as a solvent for AgI and CuI, which have higher melting points of 558 °C and 606 °C, respectively.[58] However, in this work, the compositional homogeneity was not reported.

There have been a handful of reports of thin film processing of these materials, which have mostly been reported since 2021. Like Ag-Bi-I and LHPs, thin films of Cu-Ag-Bi-I compounds are commonly deposited by solution processing thus far, typically using a mixture of DMF and DMSO as the solvent.[28,33,58,62,65,92,93] A challenge is that the binary iodide salts tend to have low solubility in this solvent mixture, or in each solvent individually.[93] Thus, groups have reported that the Cu-Ag-Bi-I films are Ag- and Bi-poor compared to the precursor stoichiometry,[28,33] and many groups have mixed their solutions at high temperature and sometimes spin coat with the precursor solution still warm to avoid precipitating out the inorganic salts.[28,33,62,92] Another strategy employed to overcome this challenge is to add pyridine to the precursor solution,[93] or to directly use pyridine to dissolve CuI before mix-

ing this solution into the DMF/DMSO solution containing the Ag-Bi-I precursors.[28] Indeed pyridine has been found to coordinate with both CuI and BiI_3.[94]

Finally, as mentioned in Section 2.3.1, DMSER has also been used to synthesize Cu-Ag-Bi-I thin films, where the stoichiometry can be tuned through the thickness of the original metal layers sputter deposited.[91] However, in all cases, a thin layer of CuI forms on the surface of the films, and this can act as a HTL, given its wider bandgap and lower ionization potential compared to Cu-Ag-Bi-I semiconductors. This surface CuI layer can be removed by etching with dilute nitric acid.[91]

2.3.3 Optoelectronic and Charge-Carrier Transport Properties

Several groups have found that Cu-Ag-Bi-I compounds have high absorption coefficients $>10^5$ cm^{-1} (Fig. 14a),[28,65] which are at a comparable level to the reported absorption coefficients of Ag_3BiI_6 (see Fig. 6).[38] Taking the specific example of Cu_2AgBiI_6, the absorption coefficient at the band-edge substantially exceeds that of $MAPbI_3$ perovskite, as well as the popular elpasolite $Cs_2AgBiBr_6$ (Fig. 14a). Notably, Cu_2AgBiI_6 exhibited a PL peak at room temperature, albeit red-shifted to 1.71 eV (Fig. 14a).[28] Sansom *et al.* also found that $CuAgBiI_5$ has slightly higher absorption coefficients than Cu_2AgBiI_6, although the PL intensity was weaker.[33] The bandgap of $CuAgBiI_5$ and Cu_2AgBiI_6 are similar (1.8 eV and 2.06 eV, respectively).[28,33] Fan *et al.* found that increasing the Cu and I content (to maintain charge neutrality) in DMSER-made Cu-Ag-Bi-I films resulted in a reduction in the bandgap from 1.91 eV ($Cu_{0.6}AgBi_2I_{7.6}$) to 1.78 eV ($CuAgBi_2I_8$).[91]

To better understand the origin of the high absorption coefficients in Cu_2AgBiI_6, the orbital-projected density of states were calculated (Fig. 14b). As with all other Ag-Bi-I materials, the upper VB is mainly comprised of Ag 4d and I 5p orbitals, whilst the lower CB is mainly comprised of Bi 6p and I 5p orbitals. Introducing Cu results in a substantial increase in the density of states in the upper VB due to Cu 3p orbitals (Fig. 14b, blue), with minimal changes in the CB. These changes to the VB density of states result in the

high absorption coefficients found in Cu_2AgBiI_6.[28]

From the absorption spectrum of Cu_2AgBiI_6, it can be seen that there is a small peak just above the absorption onset (Fig. 14a), which may arise from an excitonic peak. To understand this, Sansom *et al.* fitted the Elliott model to the absorption spectrum, obtaining an E_b of only 25 meV.[28] The low E_b may be due to the higher band dispersion and lower effective masses in $Cu_x(AgBi)_{1-x}I_4$ with increasing Cu content.[62]

At the same time, there is a significant Stokes shift in the PL peak, that is not consistent with the low E_b. Buizza *et al.* tested the hypothesis that this large Stokes shift is due to carrier localization.[62] Using optical pump - terahertz probe (OPTP) spectroscopy, Buizza *et al.* measured the photoconductivity transients in this material, observing an ultrafast decay in photoconductivity over the first few picoseconds, followed by a slow tail in the decay of the OPTP signal. The initial rapid decay in photoconductivity is characteristic of carrier localization due to strong electron-phonon coupling, resulting in the charge-carrier wavefunction localizing to the order of a unit cell, causing a substantial reduction in mobility (and therefore decrease in photoconductivity). This carrier localization process was found to be particularly severe in $AgBiI_4$. Intriguingly, increasing the Cu content resulted in an increased tail in the photoconductivity transients, suggesting the presence of more free charge-carriers, and an increase in the overall charge-carrier mobility.[62]

In addition, Buizza *et al.* found that increasing the Cu content in $Cu_{4x}(AgBi)_{1-x}I_4$ compounds led to a reduction in the E_b from 27 meV ($AgBiI_4$) to 19 meV (Cu_6AgBiI_{10}).[62] Both Buizza *et al.* and Sansom *et al.* found the E_b for Cu_2AgBiI_6 to be 25-27 meV.[62,90] These values were all obtained from Elliott model fitting of the optical absorption spectra of these materials as thin films,[62,90] and imply that a substantial fraction of the charge-carriers at room temperature in these materials are free carriers. Furthermore, Buizza *et al.* found from OPTP measurements that the photoconductivity signal did not completely decrease to zero instantaneously after photo-excitation, but rather the kinetics changed depending on the Cu content.[62] This is also consistent with free carriers being dominant, since the formation of

excitons would lead to the OPTP signal decreasing to zero. Indeed, electron-beam induced current (EBIC) measurements showed that the electron/hole diffusion lengths were short in Cu_2AgBiI_6 and $CuAgBiI_5$, in the range of 40–50 nm, well below the active layer thickness of 120–150 nm.[65]

2.3.4 Materials Stability

Sansom *et al.* found that while $CuBiI_4$ decomposed to BiI_3 and CuI at room temperature, the stability of Cu_2AgBiI_6 was substantially improved, with no signs of decomposition after a week, even under 1-sun illumination (Fig. 15a).[28]

Ambient air exposure has a curious effect on the optoelectronic properties of $CuAgBiI_5$. Like Cu_2AgBiI_6, there is a large Stokes shift in the PL peak compared to the optical bandgap, which may also originate from carrier localization (see Section 2.3.2). Intriguingly, it was found that the PL peak blue-shifted and became brighter as the $CuAgBiI_5$ film was kept in ambient air (the sample was kept in ambient air in the dark, and measured after 20 min, 60 min and 90 min since being taken to air), as seen in Fig. 15b.[33] This observation was attributed to oxygen passivation of deep traps in the Cu-Ag-Bi-I film, and is consistent with the observed increase in PL lifetime after storage in air.[33] On the other hand, after a week of air exposure, $CuAgBiI_5$ changed color from dark red to yellow, despite no changes in the bulk diffraction pattern, indicating that this material may not be as air-stable as Cu_2AgBiI_6.[33]

2.4. Defects and Ion Migration

One of the key motivations behind the exploration of Bi-based materials is to find compounds that could replicate the defect tolerance of LHPs through similarities in the electronic structure.[89] However, it is questionable as to whether materials in the CuI-AgI-BiI_3 phase space are defect tolerant, and indeed we argue later in Section 3.1 that it is not.

Efforts into understanding and controlling the defects present in these materials have thus far focussed on the ternary silver bismuth iodide semiconductors. These studies have mostly

been on the structural and point defects in Ag-Bi-I thin films by controlling the composition and morphology. However, thus far, there have been no detailed studies into the point defects present (*e.g.*, vacancies or interstitials). Probing these point defects experimentally and computationally would be challenging. Ag-Bi-I compounds are ionic conductors, and ion migration would complicate the use of any capacitance-based method to measure the traps present (such as thermal admittance spectroscopy).[95] Cation disorder makes it difficult to accurately simulate these systems computationally to determine the defect diagrams. Overcoming these challenges will be important to understand what defects are limiting performance, and how the processing and composition of these materials could be optimized in the future. This section discusses the few works that have considered the defects that may be present in Ag-Bi-I semiconductors.

2.4.1 Defects in Ag-Bi-I Compounds

Table 3 summarizes the carrier type of Ag-Bi-I compounds (made by spin coating with antisolvent dripping), and the point defects that may be present to give rise to this type of conductivity.[52] The Ag-rich materials, Ag_3BiI_6 and Ag_2BiI_5, exhibit p-type conductivity, indicating the involvement of acceptor-like point defects, as these compounds have been observed to occur with unreacted AgI.[20,56] Ag vacancies (V_{Ag}) are therefore a plausible cause of these observations. $AgBiI_4$ and $AgBi_2I_7$, on the other hand, showed n-type conductivity. Unreacted BiI_3 has been observed in Ag-poor materials,[20,56] signifying the presence of I vacancies (V_I) in these compounds.

Macroscopic structural defects are also present in Ag-Bi-I thin films. As with other thin films, grain boundaries can act as sites of non-radiative recombination, and pinholes in the film can cause shunting in the vertically-structured photovoltaic device. But apart from these structural/macroscopic defects, Kulkarni *et al.* found that Ag_3BiI_6 thin films grown by solution processing (and using a chlorobenzene antisolvent) formed voids at the interface

with the TiO_2 ETL it was deposited onto (Fig. 16a).[56] It was believed that these voids formed because the chlorobenzene antisolvent could remove excess DMSO solvent, especially at the bottom interface. As a result, Ag_3BiI_6 only crystallized at the top surface, forming voids at the bottom.[56] Such voids act as sites of non-radiative recombination and limit electron extraction, thus decreasing the photovoltaic performance of these materials, and possibly also decreasing the stability of the devices in air. These voids could be eliminated by depositing Ag_3BiI_6 without using any antisolvent.

Table 3: Carrier type, possible defects and likely phase impurities reported so far in $Ag_aBi_bI_{a+3b}$ compounds. n.r. = no report.[52]

Compound	Carrier Type	Acceptor-like defects	Donor-like defects	Impurities
Ag_3BiI_6	p-type	Ag vacancies, Ag on Bi anti-sites	n.r.	AgI
Ag_2BiI_5	p-type	I on cation anit-sites	n.r.	AgI
$AgBiI_4$	n-type	I interstitials, Ag vacancies	I vacancies, Bi on I anti-sites	Ag_2BiI_5
$AgBi_2I_7$	n-type	n.r.	Bi interstitial	BiI_3

2.4.2 Ion migration in Ag-Bi-I

Despite Ag-Bi-I originally being investigated as an ion conductor, little is known about ionic conductivity in these materials. The activation energy barrier for Ag^+ cation migration has been reported to be 0.4 eV in Ag_3BiI_6 single crystals made by solvothermal growth,[16] which is similar to the activation energy of I migration (0.44 eV) in lead halide perovskites.[56] Although Ag-Bi-I semiconductors are thermodynamically favored to form, Kulkarni *et al.* found through computations that the degradation of Ag_3BiI_6 to AgI and BiI_3 is also thermodynamically favored, with a negative enthalpy change of -0.053 eV per formula unit.[56] This is consistent with the presence of AgI and BiI_3 phase impurities in the Ag-Bi-I films (see Tables 1 and 3). It is believed that AgI can decompose further to Ag^+ and I^-. It is proposed that these ionic species, as well as BiI_3, can diffuse through the organic HTL (accentuated

by the presence of an electric field) and reach the Au electrode (Fig. 16b). BiI_3 can undergo an underpotential deposition reaction on the surface of Au, leading to the formation of Bi^0, while Au reacts with the iodide species, and likely forms Au^+. This proposed mechanism was corroborated by X-ray photoemission spectroscopy measurements on the surface of Au, where a degradation product peak was found from the Au 4f spectra (Fig. 16c), and Bi^0 was found from the Bi 4f spectra (Fig. 16d).[56] This degradation mechanism was suppressed by increasing the thickness of the HTL. Further work is needed to prove the mechanism by which these species migrate to the Au electrode, but it is suspected that these are facilitated by vacancy defects, as well as the voids present in the film.[56]

3. Applications

3.1 Solar Cells

Since the first two reports of photovoltaics using Ag-Bi-I semiconductors were made in 2016,[21,22] a wide range of deposition methods, fabrication protocols and device structures have been investigated, as shown in Table 4. The highest PCE under 1-sun illumination now reported is 5.56% for Ag_3BiI_6 compounds with S additives (Table 4), which lowered the bandgap.[74] 1-sun SLMEs for these materials have been reported for $AgBiI_4$, Ag_2BiI_5 and $CuBiI_4$, and these SLMEs were found to be 26%, 24% and 17–20%, respectively.[23,86] We note that the SLME for $CuBiI_4$ was calculated based on computationally-determined crystal structures instead of the experimentally-solved cubic structure.[33,86] Nevertheless, the highest PCEs reported for these compounds (2.8%, 2.6% and 1.12% for $AgBiI_4$, Ag_2BiI_5 and $CuBiI_4$, respectively, as shown in Table 4) are still well below these SLMEs, showing there to be much room for improvement.

The correlation between the short-circuit current density (J_{SC}), open-circuit voltage (V_{OC}) and fill factor (FF) with the PCE of these photovoltaic devices is visualized in Fig. 17a–c. From these, it can be seen that the main factor influencing PCE is the J_{SC}, while FF has a lower influence, and the V_{OC} has almost no correlation with PCE, apart from the

lowest performing devices.[20–22,26,27,38–40,45,58,59,64–67,74,77,78,82,88,96–107] In this section, we will examine the role and relative importance of a range of properties and processing conditions on Ag-Bi-I photovoltaic performance.

3.1.1 Morphology vs. Defects

In the early studies of Ag-Bi-I solar cells, there was a tendency to think that the PCE was mainly limited by the poor morphology of the Ag-Bi-I absorber layers. In contrast to hybrid LHPs, Ag-Bi-I semiconductors form adducts with a much higher content of solvent molecules. For example, Ag_3BiI_6 coordinates with 8 DMSO molecules each,[20] which leads to substantial shrinking of the adduct layer upon decomposition during annealing (see Fig. 18). This shrinking results in the formation of discontinuous Ag-Bi-I films with columnar morphology. If antisolvent treatment is used, then crystallization begins from the top of the film, which results in the formation of voids in the bottom part of the film (see Section 2.4.1 for a detailed discussion[56]). Ghosh *et al.* optimized the hot casting procedure and improved the morphology of the absorber layers. Whilst they improved the PCE for Ag_2BiI_5 from 1.6% to 2.6% by changing from spin coating to hot-casting, they were not able to exceed earlier reports of Ag-Bi-I solar cells (see Table 4).[27] Similarly, for absorber layers with improved morphology fabricated by co-evaporation of AgI and BiI_3,[106] or by co-sputtering of Ag and Bi followed by treatment in iodine vapor,[38] the PCEs reached were <1% (Table 4).

As we can see in Fig. 17(d), the PCE tends to be higher for Ag-rich compositions. Here, we are plotting the PCEs shown for all of the solar cell devices in the above panels (*i.e.*, Fig. 17a-c) as a function of the ratio of Bi^{3+} to all cation species present in the nominal stoichiometry. We denote this as $b/(a+b)$, which is directly applicable for Ag-Bi-I compounds with the general formula $A_aB_bX_{a+3b}$. We emphasize that Cu-Ag-Bi-I quaternary compounds do not have this general formula (see Section 2.3.1 for a description of the structure of these materials). For completeness, it is still useful to include the data for these

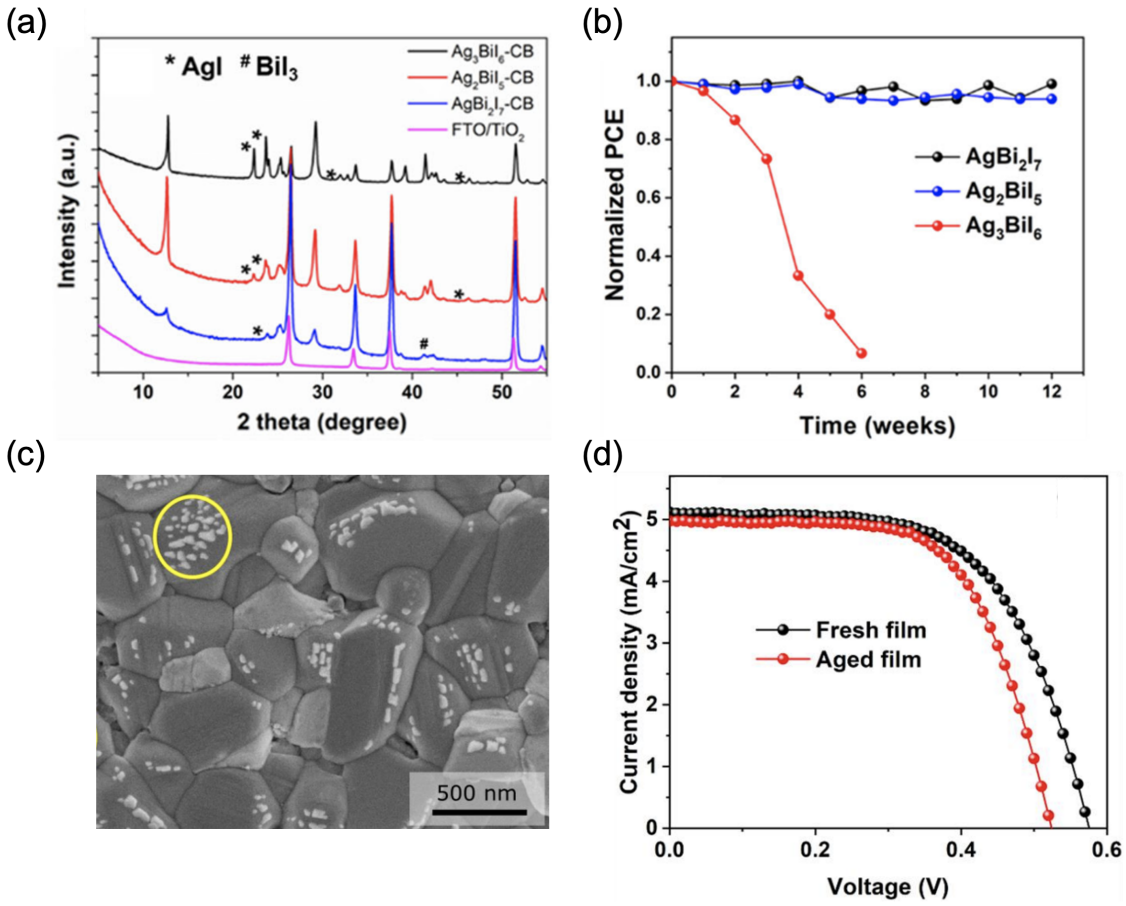

Figure 9: Effect of air exposure on the performance of Ag-Bi-I thin films. (a) XRD pattern and (b) normalized PCE of Ag-Bi-I thin films used in photovoltaics. The XRD patterns were taken in air on fresh samples. (c) Top-down scanning electron microscopy (SEM) image of a Ag_3BiI_6 thin film giving an example of bright spots that sometimes appear in the secondary electron image. (d) Current density - voltage curves of devices made from Ag_3BiI_6 that were fresh, and aged in air for 2 weeks. For the aged samples, the P3HT HTL and Au were only deposited over the Ag-Bi-I films after the 2 week ageing period. Parts (a), (b) and (d) reproduced with under the terms of the CC-BY license from Ref.[56] Copyright 2021, The Authors. Part (c) reproduced with permission from Ref.[38] Copyright 2020, American Chemical Society.

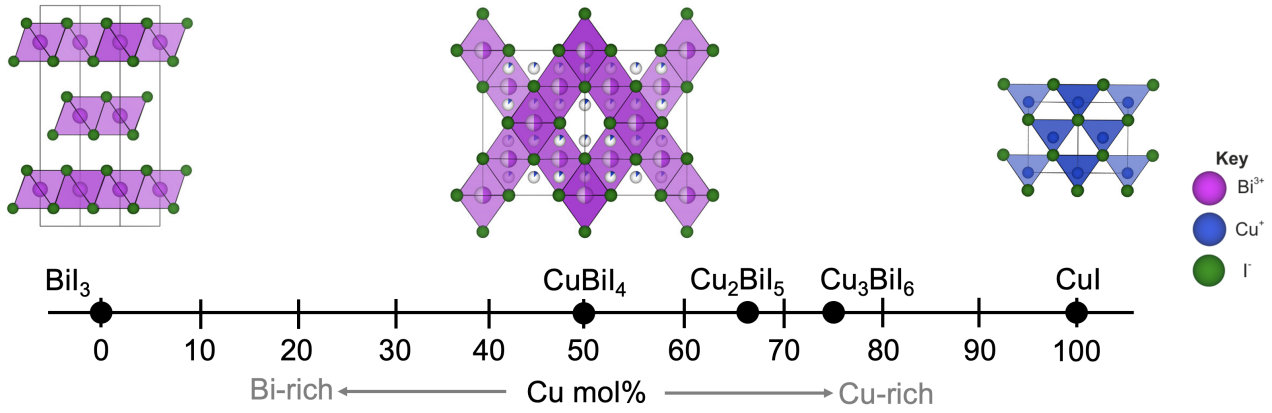

Figure 10: Reported stoichiometries of Cu-Bi-I compounds, and a comparison of the solved structure of $CuBiI_4$ with the structures of BiI_3 and CuI. Adapted with permission under the terms of the CC-BY license from Ref.[33] Copyright 2021, The Authors.

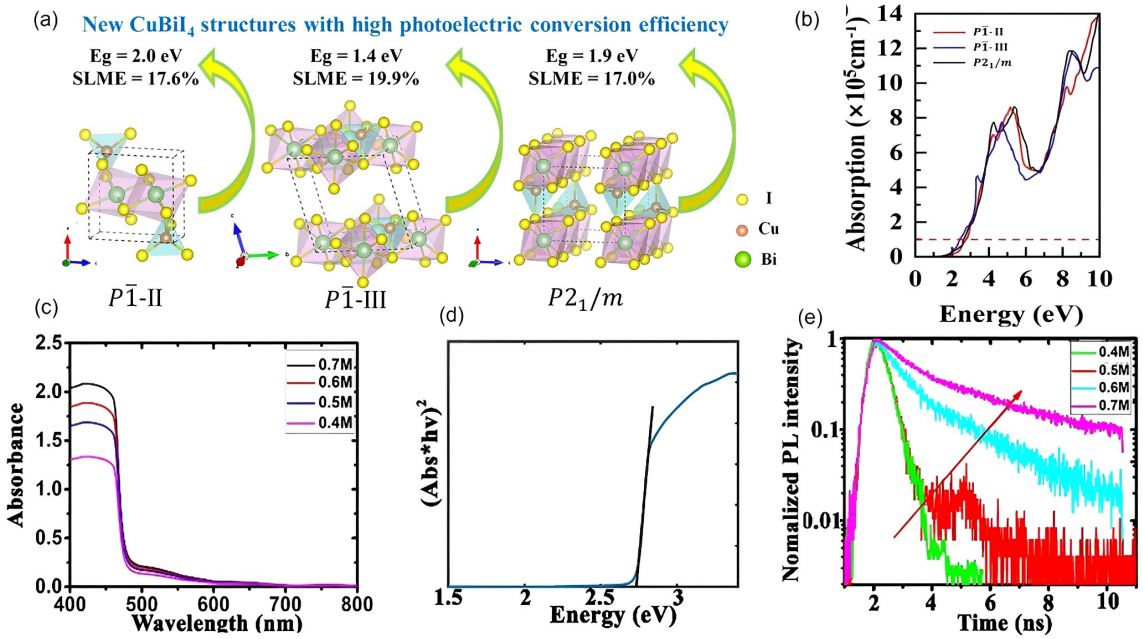

Figure 11: Properties of $CuBiI_4$ from computations and experiment. Computations: (a) Predicted structures of $CuBiI_4$: P$\bar{1}$-II, P$\bar{1}$-III, and P2_1/m, and (b) calculated optical absorption spectra of the three structures.[86] Experiment: (c) UV-Vis absorbance spectra of $CuBiI_4$ deposited from precursors with concentrations of 0.4–0.7 M. (d) Tauc plot to determine the direct bandgap of $CuBiI_4$ deposited from a solution with 0.7 M concentration, and (e) PL decay curves of $CuBiI_4$ deposited from solutions with different concentrations.[66] Parts (a-b) reprinted with permission from Ref.[86] Copyright 2021, American Chemical Society. Parts (c-e) reproduced with permission from Ref.[66] Copyright 2018, Wiley.

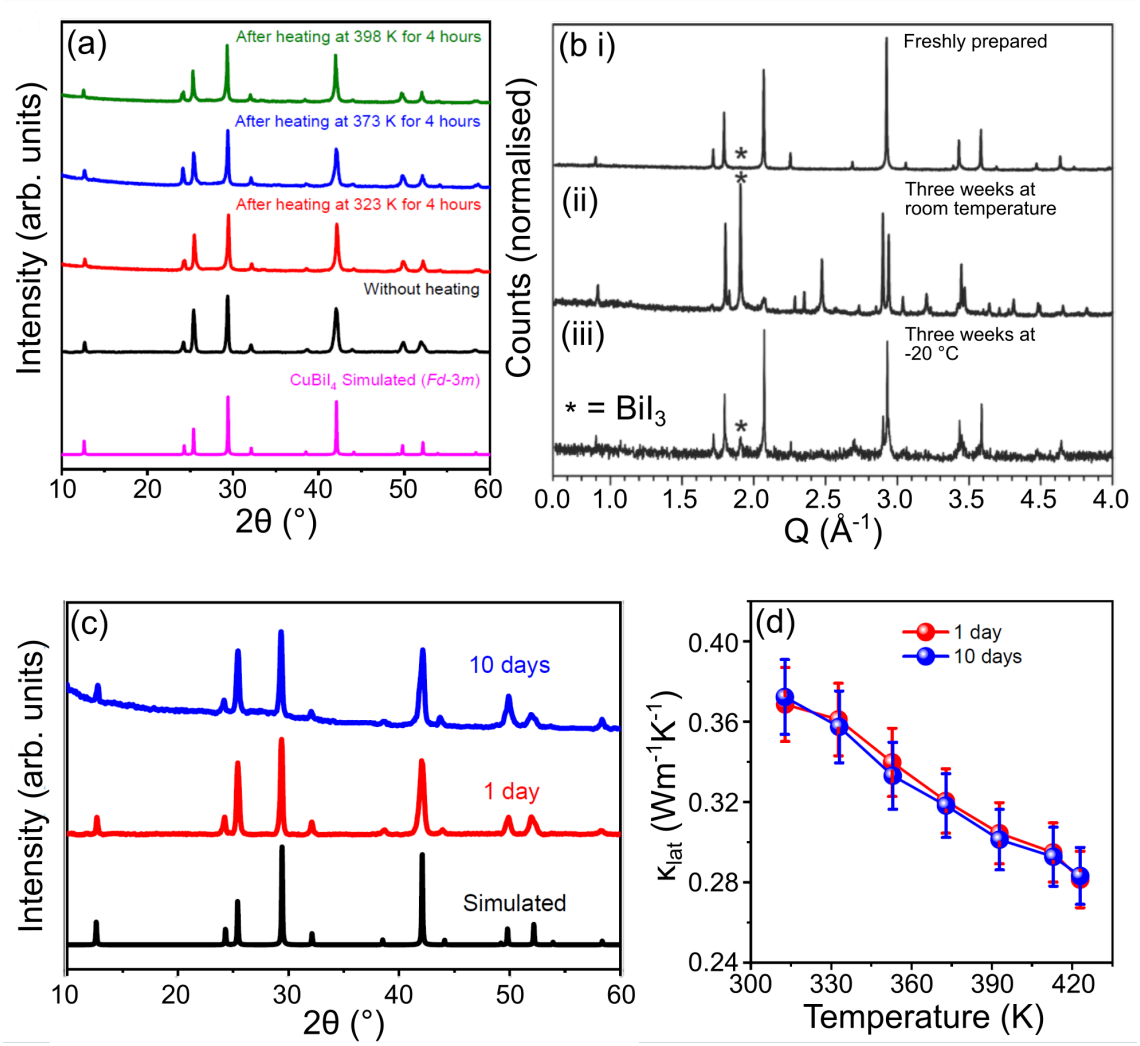

Figure 12: Stability studies of $CuBiI_4$ powder samples. (a) Thermal stability of $CuBiI_4$ after heating for four hour intervals in an air oven.[83] (b) PXRD patterns of (i) freshly prepared $CuBiI_4$ powder, and powders stored in air and darkness for three weeks at (ii) RT and (iii) $-20\,^{\circ}C$.[28] (c) PXRD patterns and (d) lattice thermal conductivity measurements of $CuBiI_4$ powders stored in open lab conditions for ten days. Das *et al.* suggest $CuBiI_4$ is a stable material.[83] However, Sansom *et al.* believe that it is only meta-stable and degrades to BiI_3 and CuI when given enough time.[28] Parts (a), (c) and (d) reprinted (adapted) with permission from J. Am. Chem. Soc. 2023, 145, 2, 1349–1358. Copyright 2023, American Chemical Society. Part (c) reproduced with permission under the terms of the CC-BY license from Ref.[28] Copyright 2021, The Authors.

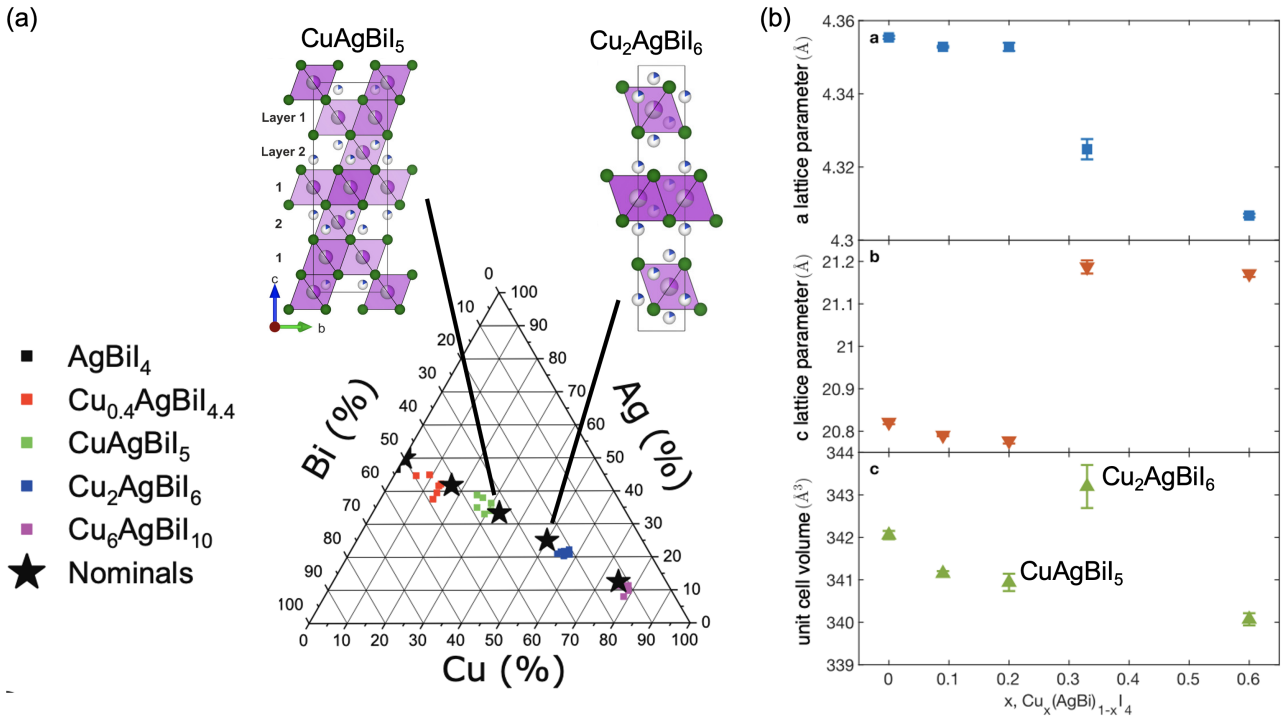

Figure 13: Structure of quaternary Cu-Ag-Bi-I compounds. (a) Nominal and reported compositions of Cu-Ag-Bi-I materials investigated, and (b) the lattice parameters and unit cell volumes of these materials. These are plotted against x in $Cu_x(AgBi)_{1-x}I_4$, where x = 0 ($AgBiI_4$), 0.09 ($Cu_{0.4}AgBiI_{4.4}$), 0.2 ($CuAgBiI_5$), 0.33 (Cu_2AgBiI_6), 0.6 (Cu_6AgBiI_{10}). Adapted with permission under the terms of the CC-BY license from Ref.[62] Copyright 2022, The Authors.

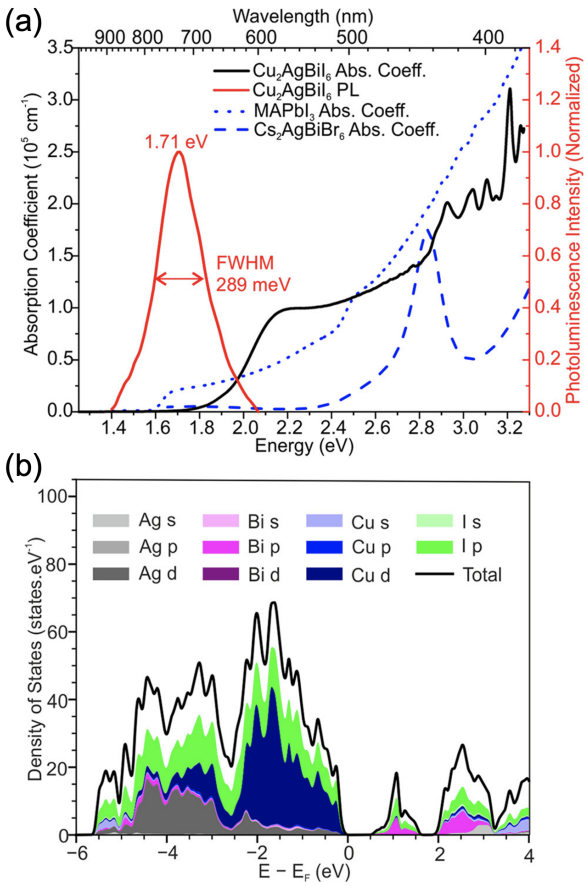

Figure 14: Optical and electronic properties of Cu-Ag-Bi-I compounds. (a) Absorption coefficient (black) and PL spectra (red) of Cu_2AgBiI_6 thin films compared with the absorption coefficient of $MAPbI_3$ (blue, short dashes) and $Cs_2AgBiBr_6$ double perovskite (blue, long dashes). (b) Calculated orbital-projected density of states of Cu_2AgBiI_6. Reproduced under the terms of the CC-BY license from Ref.[28] Copyright 2021, The Authors.

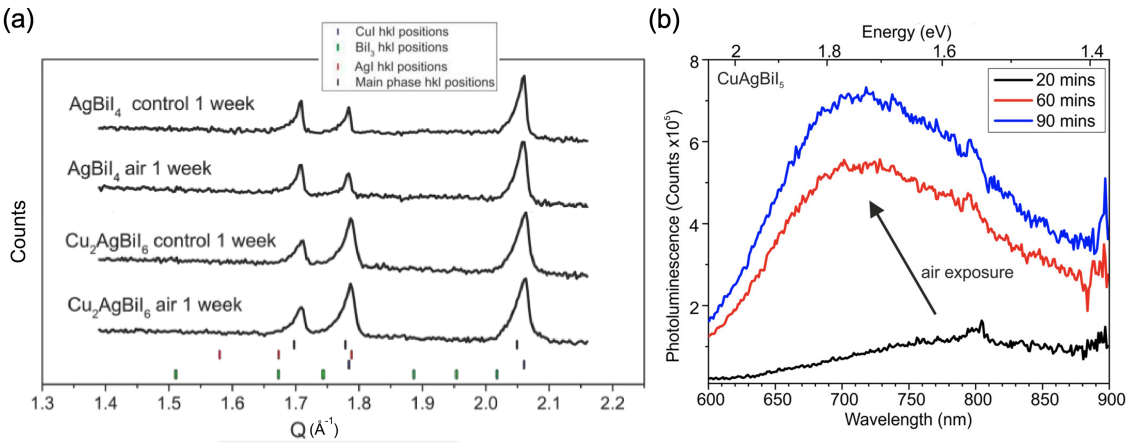

Figure 15: Stability of quaternary Cu-Ag-Bi-I compounds. (a) Powder XRD pattern of Cu_2AgBiI_6 stored in air in the dark (control) compared to Cu_2AgBiI_6 stored in a capillary sealed with air and exposed to 1-sun illumination. Both sets of samples were stored for 1 week. These measurements are compared to $AgBiI_4$ stored under equivalent conditions. Reproduced under the terms of the CC-BY license from Ref.[28] Copyright 2021, The Authors. (b) PL spectra of $CuAgBiI_5$ thin films made in a N_2-filled glovebox and stored in air for up to 90 min. Part (f) reproduced with permission from Ref.[33] under the terms of the CC-BY license. Copyright 2021, The Authors.

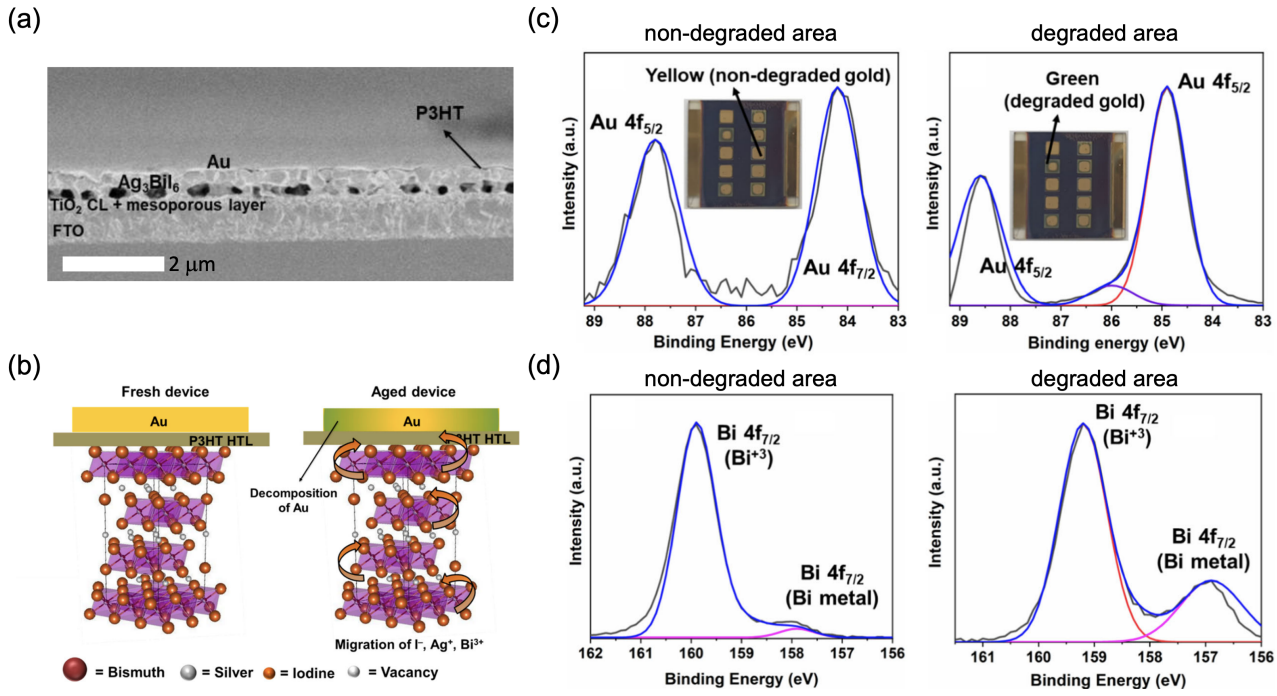

Figure 16: Defects and ion migration in Ag-Bi-I semiconductors. (a) Cross-sectional SEM image of a Ag_3BiI_6 photovoltaic device, showing voids at the TiO_2/Ag_3BiI_6 interface. (b) Proposed mechanism for Au electrode degradation through the migration of I^-, Ag^+ and Bi^{3+} ions through the organic HTL. X-ray photoemission spectra of the (c) Au 4f and (d) Bi 4f core levels, measured on the Au top electrode in the regions that were pristine *vs.* degraded (shown inset in part (c). Reproduced with under the terms of the CC-BY license from Ref.[56] Copyright 2021, The Authors.

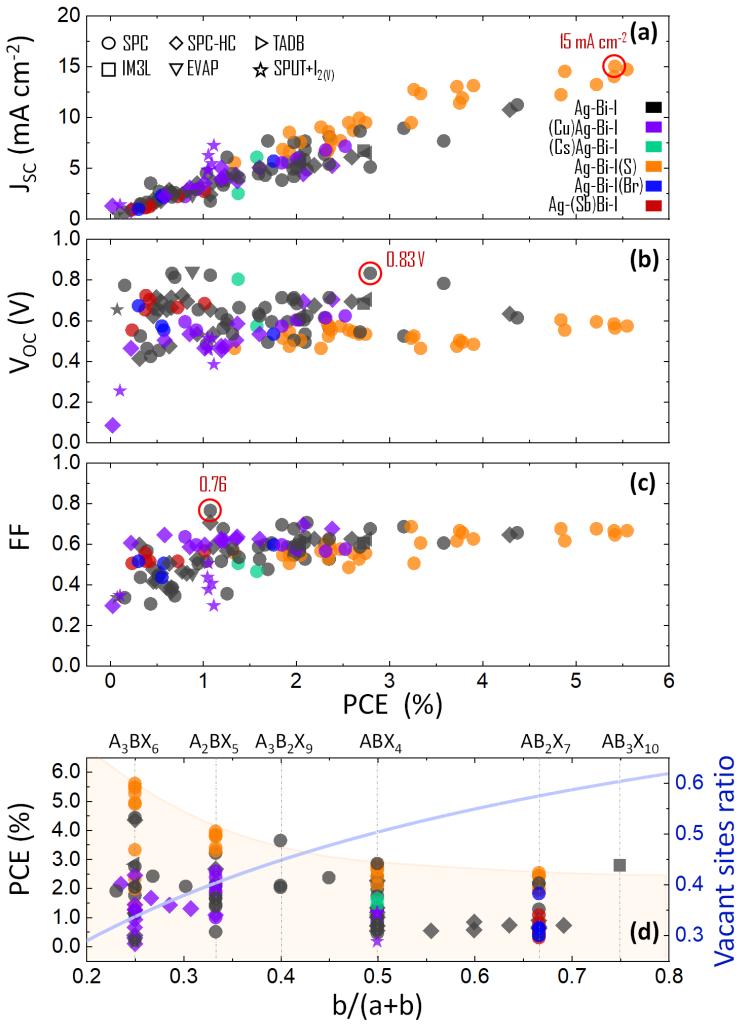

Figure 17: Visualization of the performance parameters tabulated in Table 4,[20–22,26,27,38–40,45,58,59,64–67,74,78,82,88,96–98,100–107] showing the correlation between the (a) J_{SC}, (b) V_{OC}, and (c) FF with the PCE. (d) PCE *vs.* nominal stoichiometry expressed as b/(a+b) for $A_aB_bX_{a+3b}$ compounds, where A = Ag, Cu; B = Bi, Sb and X = I, Br. Please note that we include the data for Cu-Ag-Bi-I absorbers on this plot by taking b/(b+a) as being the fraction of Bi^{3+} to the total number of cations in the formula of the species. But we emphasize that these quaternary compounds do not have the general formula $A_aB_bX_{a+3b}$, and the number of vacant sites deviates from the rudorffite structure model (see Section 2.1.1 and 2.3.1). The blue line in part (d) shows the vacant site ratio in the cation sublattice calculated for various stoichiometries.[20,21] The shapes of the points correspond to the fabrication methods: SPC (circles), SPC-HC (diamonds), TADB (right-triangles), IM3L (squares), EVAP (down-triangles), SPUT+$I_{2(V)}$ (stars), where SPC is spincoating, SPC-HC is spincoating with hot-casting, TADB is thermally-assisted doctor blading, IM3L is infiltration into mesoscopic three-layer structure, EVAP is evaporation, SPUT+$I_{2(V)}$ is sputtering with subsequent treatment in iodine vapor. The colors of the points correspond to various elemental compositions: Ag-Bi-I (black), (Cu)Ag-Bi-I (violet), (Cs)Ag-Bi-I (green), Ag-Bi-I(S) (orange), Ag-Bi-I(Br) (blue) and Ag-(Sb)Bi-I (red). The empty red circles highlight the highest J_{SC} (15 mA cm^{-2}),[74] V_{OC} (0.83 V),[101] and FF (76%)[39] out of all devices reported thus far that we are aware of.

Table 4: Reported photovoltaic performance of Cu-Ag-Bi-I absorbers. The average values and uncertainties for each performance parameter, along with the performance of the champion device, are shown where available. [Please note that this is a placeholder. Please refer to the Word document with the full table included, along with the definitions of all abbreviations used.]

quaternary absorbers. Interestingly, in Fig. 17(d), we observe that the PCEs of solar cells based on Ag-Bi-I absorbers decrease overall as the content of Bi increases. Simultaneously, for increases in $b/(a+b)$, the fraction of octahedral holes in a rudorffite structure occupied by vacancies (*i.e.*, vacant sites ratio) increases (see Section 2.1.1.)[20] Thus, we would infer that the probability of lattice defects forming increases as the materials become more Bi-rich, which is consistent with the overall reduction in PCE. This hypothesis correlates with ultrafast transient absorption spectroscopy studies that reveal significantly slower trap-mediated charge-carrier recombination in Ag_3BiI_6 in contrast to $AgBiI_4$.[108] Also, the time-resolved microwave conductivity (TRMC) figure of merit, studied by Iyoda *et al.*,[109] is significantly higher for Ag-rich compositions. At the same time, we observe no trend in the PCE of solar cells based on Cu-Ag-Bi-I *vs.* $b/(a+b)$ (Fig. 17(d)). This may be because these materials are severely underdeveloped in photovoltaics compared to Ag-Bi-I compounds, but also because the fraction of octahedral and tetrahedral holes that are vacant has a more complex relationship with the content of monovalent cations (see Section 2.3.1).

Nevertheless, we can draw several conclusions: (1) materials within the CuI-AgI-BiI_3 phase space are not defect tolerant semiconductors, (2) trap-mediated charge-carrier recombination seems to be the major performance-limiting factor and (3) Ag-Bi-I compounds that are Ag-rich, in general, give higher PCEs, because they tend to form a lower density of traps. From these arguments, we would suggest three strategies to combat the issue of trap-mediated charge-carrier recombination in Ag-Bi-I photovoltaic devices: (1) improving the crystallinity and minimizing the native defect density, (2) compensation of traps by doping and (3) fabrication of extremely thin absorber heterojunction structures (as detailed later). This analysis also encourages future efforts on photovoltaics to focus on compounds with lower fractions of the cation sites occupied with vacancies.

3.1.2 Morphology Control

Precursor Dissolution

Beyond challenges with the formation of pinhole-free Ag-Bi-I thin films, it has also been challenging to find suitable solvents to dissolve the AgI and BiI_3 precursors for Ag-Bi-I compounds. BiI_3 is sparingly soluble, and AgI insoluble in polar aprotic solvents commonly used in solution processing halide compounds, *e.g.*, DMF and DMSO.[20,22] The strategies employed to overcome this limitation have been to (1) heat the polar aprotic solvents, (2) add a small quantity of acid to the precursor solution to improve solubility, or (3) change to a different solvent system.

In the first case, Turkevych *et al.* reported that AgI can be dissolved in DMSO when mixed with BiI_3 and heated to 110 °C. This was attributed to the formation of $[BiI_{3+x}]^{x-}$ complex ions that faciliate AgI dissolution.[20] The warm solution was deposited by spin coating onto substrates that were not pre-heated (*i.e.*, not hot casting), but with the use of a toluene antisolvent. Pinhole-free Ag_3BiI_6 thin films were achieved, with 4.3%-efficient photovoltaic devices realized (Table 4).[20]

In the second case, groups have reported successful dissolution of Ag-Bi-I precursors by adding HI or HCl to the organic solvents. Shao *et al.* mixed AgI and BiI_3 into DMF at a lower temperature of 70 °C, and improved precursor dissolution by adding 50–70 μL of 37% HCl to a 1 mL solution.[97] Dense films with large grains were achieved across a range of Ag-Bi-I stoichiometries, however the photovoltaic performance only reached up to 0.78% for $Ag_2Bi_3I_{11}$, mostly due to low short-circuit current densities of up to 2.39 mA cm^{-2}.[97] This was due to low external quantum efficiencies (EQEs) reaching up to 15%.[97] Jung *et al.* took a different approach of pre-synthesizing Ag_2BiI_5 powders through melt synthesis, then dissolving these powders into a DMF/DMSO solution by adding a small quantity of HI (DMSO:DMF:HI = 3:2:0.2 by volume).[96] However, these Ag_2BiI_5 films did not completely cover the mesoporous TiO_2 substrate, and yet a higher PCE of 2.31% was achieved, mainly due to higher J_{SC} values of 6.33 mA cm^{-2}.[96] A discontinuous morphology was also achieved by Vivo and co-workers with Cu_2AgBiI_6 thin films. Adding 1.5 vol.% HI to the precursor solution (using a mixture of DMF and DMSO as the solvent) resulted in films that were still

dicontinuous, but had larger microfeatures with greater coverage of the substrate, leading to an increase in the PCE from 0.60% (no HI) to 1.30% (with HI), and this was attributed to a reduction in the defect density of these films.[110]

In the third strategy, groups have investigated the use of primary alkylamines as an alternative to polar aprotic solvents, since the alkylamines are known to dissolve AgI.[22] Kim *et al.* proposed the use of n-butylamine, and successfully achieved dense thin films that were pinhole-free after annealing at 150 °C. This annealing temperature was found from FTIR measurements to remove remnant n-butylamine and therefore fully crystallize the film. The PCE achieved in photovoltaic devices was 1.22% (see Table 4).[22] Zhu *et al.* used the same solvent to dissolve AgI and BiI_3, and improved the PCE up to 2.1% (see Table 4) by tuning the stoichiometry towards Ag-rich Ag_2BiI_5, despite the presence of a small quantity of pinholes.[40]

Similar strategies have been adopted for Cu-based systems. For example, whilst CuI has low solubility in DMF or DMSO, a combination of CuI and SbI_3 was found to dissolve.[99] Similarly, for $CuBiI_4$, the use of HI mixed with *N*,*N*-dimethylacetamide successfully dissolved the precursors.[66] However, in both cases, the PCEs reached were poor, below 1%, as is the case with all other solution-processed Cu-Bi-I compounds without Ag added (Table 4). Finally, as discussed earlier in Section 2.3.2, adding pyridine to the DMF/DMSO solvent mixture has been found to improve the solubility of the binary iodide precursors for making quaternary Cu-Ag-Bi-I compounds, and this contributed to an improvement in PCE from 0.43% to 1% for Cu_2AgBiI_6.[28,93] However, these PCEs are still low compared to those achieved using hot casting and solvent-free methods (see next two sections below).

Antisolvent Dripping and Hot Casting

In the solution processing of LHPs, a common strategy to improve film morphology is to employ antisolvent treatment. In this approach, a solvent with poor solubility for the precur-

sors is dripped onto the film during spinning, washing away the original "good" solvent. This induces rapid supersaturation, and the formation of a high density of nuclei, thus increasing the chances of avoiding pinholes (see Ref.[111] for mechanistic details). As mentioned earlier in Section 3.1.1, antisolvent treatment has been employed with the deposition of Ag-Bi-I and Cu-Ag-Bi-I films, giving rise to improvements in morphology. Since the precursors used are polar, poor solvents will have low dielectric constants and low polarity. The antisolvents that have been investigated are ethyl ether, toluene, chlorobenzene and isopropanol, which all have dielectric constants below 20 (whereas DMF and DMSO have dielectric constants of 37).[20,58,78,103] However, the use of antisolvents has not yet proven to be as effective as in LHPs, and poor morphology is often still obtained. Furthermore, stoichiometry, device architecture, and other processing parameters, such as annealing conditions, have had a larger influence than antisolvent dripping on device performance. For example, Zhai *et al.* compared toluene, chlorobenzene and isopropanol as antisolvents and found isopropanol to give $AgBiI_4$ films with the lowest pinhole density.[103] Although this improved the PCE of $AgBiI_4$ solar cells from 0.64% (without antisolvent) to 1.26% (with isopropanol),[103] the performance falls below that reported by Turkevych *et al.* for Ag_3BiI_6 (4.3%) using a toluene antisolvent.[20]

The supersaturation during spin coating can also be enhanced through hot casting, in which both the precursor solution and substrate are pre-heated to a certain temperature, and spin coating is carried out while both are warm. This enhances the evaporation rate of the original solvent. Ghosh *et al.* combined hot casting with antisolvent dripping (using chlorobenzene as the antisolvent), improving the PCE of $AgBiI_4$ from 1.2% (comparable to the best devices reported by Zhai *et al.* for the same composition) to 2.2% with hot casting.[27,103] These improvements in device performance were due to increases in grain size and reductions in pinhole density with the use of both hot casting and antisolvent dripping.[27] However, hot casting critically depends on how quickly the substrate and precursor solution are deposited after being taken off from the substrate, and it is difficult to precisely measure

the temperature of the solution and substrate during the spin coating process. These factors make hot casting difficult to reliably reproduce in the lab with spin coating, but might be implemented more reproducibly in a manufacturing process where the substrate and precursor temperatures are controlled (*e.g.*, in blade coating).

Overall, in comparing all fabrication methods detailed in Table 4 and visualized in Fig. 17a–c, there is no significant difference between spin coating, antisolvent dripping or hot casting. These observations for Ag-Bi-I absorbers also generally apply to Cu-Ag-Bi-I absorbers, although it is more difficult to draw conclusions given the scarcity of reports on these more novel materials. As an illustrative example, Pai *et al.* reported a champion PCE of 2.45% for solar cells using hot-cast Cu_2AgBiI_6.[65] Park *et al.* obtained a slightly higher PCE of 2.53% for Ag_2BiI_5 with Cu added in, made by conventional spin coating.[58] The stoichiometry and structure of these two absorbers are likely not the same, preventing a direct like-for-like comparison. But, at least we cannot conclude that hot casting leads to a substantial improvement in PCE over conventional spin coating. Furthermore, the effects of annealing conditions on photovoltaic performance are also not clear. More work to understand the process-property-structure-performance relationships of Ag-Bi-I, Cu-Bi-I and Cu-Ag-Bi-I compounds are needed, especially focussing on scalable fabrication methods.

Solvent-Free Methods

Thermal evaporation of $AgBiI_4$[106] and sputter deposition of Ag_3BiI_6 and $CuBiI_4$ have been demonstrated,[38,67,88] as shown in Table 4. But in all cases, the performance reached has not substantially exceeded those of their solution-processed counterparts, despite dense films being achieved (see Table 4). Khazee *et al.* attributed the low performance of the thermally-evaporated $AgBiI_4$ films to be due to the presence of Bi^0, found from XPS measurements, which could act as recombination centers.[106] Crovetto *et al.* synthesized Ag_3BiI_6 films by first sputter-depositing Ag and Bi, followed by iodization. A narrow processing window was found to avoid the formation of AgI or BiI_3 impurities, and these may have played a

role in limiting device performance. Indeed, as discussed earlier in Section 2.6.2, Ag_3BiI_6 is thermodynamically favored to decompose to AgI and BiI_3.[56]

A similar approach was used to fabricate $CuBiI_4$ films from the vapor phase, in which Cu and Bi were first deposited by sputter deposition, followed by iodization.[67,88] However, it was found that the deposition of a spiro-OMeTAD HTL on top led to the re-dissolution of the dense $CuBiI_4$ film by the 4-*tert*-butylpyridine and acetonitrile present, leading to a rough morphology with intimate contact between the spiro-OMeTAD and $CuBiI_4$.[67,88] This was believed to enhance hole extraction by reducing the required hole transport length, leading to PCEs reaching 1.1%, which slightly exceeded the photovoltaic performance of solution-processed $CuBiI_4$ (0.81%),[66] as seen in Table 4.

Quaternary Cu-Ag-Bi-I films have also been prepared by iodizing sputter-deposited metallic Cu/Ag/Bi films (*i.e.*, DMSER). PCEs reaching up to 2.76% have been achieved for DMSER $CuAgBi_2I_8$ and with a natural CuI layer on top to help facilitate hole extraction. In these devices, a carbon electrode was directly deposited on top of CuI by blade coating and annealing at 100 °C for 10 min.[91] These devices are currently the most efficient for solar cells based on quaternary Cu-Ag-Bi-I absorbers (Table 4).

Further work on developing vapor-based fabrication methods are worthwhile, since these are more easily compatible with large-scale manufacturing than spin-coating. Future efforts to improve performance will require detailed analyses of processes causing non-radiative losses, the defects present in the bulk and interfaces of the films, band alignment between the absorber and charge transport layers, as well as whether the deposition of charge transport layers onto the absorber damages the film or interface.

3.1.3 Potential of the Extremely Thin Absorber Architecture

As shown in Table 4, the device structures utilized for Ag-Bi-I, Cu-Bi-I and Cu-Ag-Bi-I photovoltaics have mostly been borrowed from those developed for LHPs, *i.e.*, using mesoporous TiO_2 or SnO_2 for the ETL, and an organic HTL over the halide thin film (Fig. 19(a)).

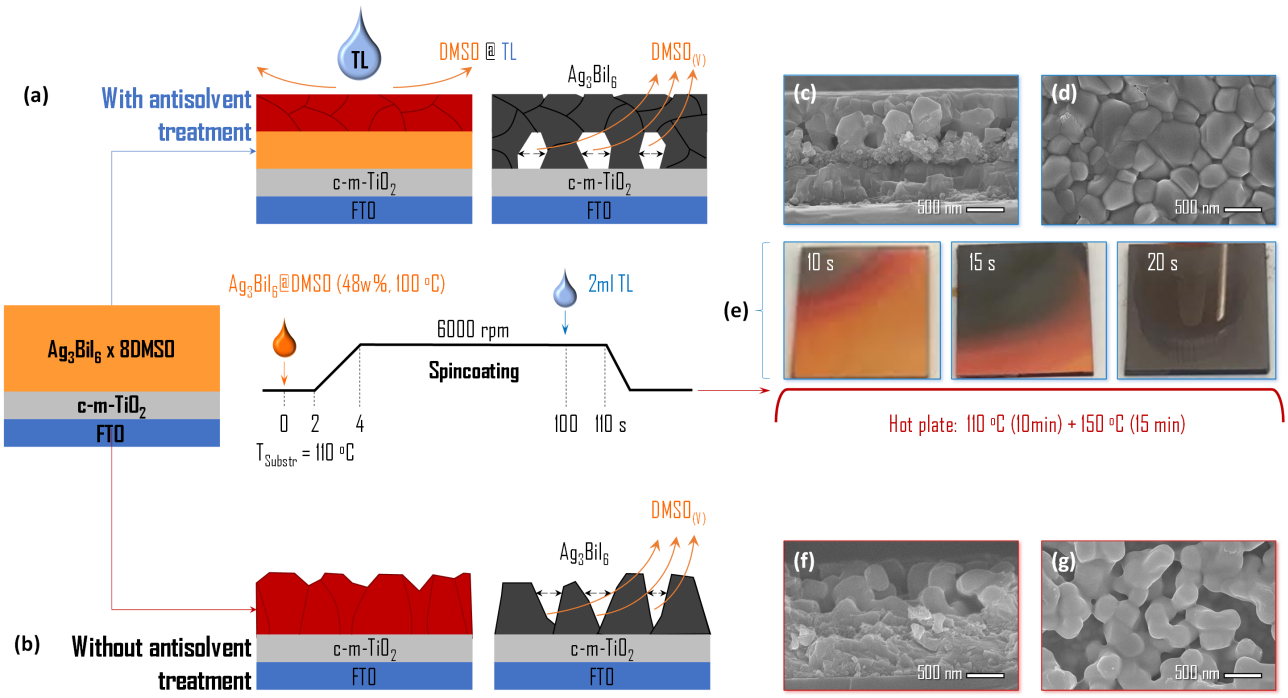

Figure 18: Fabrication of Ag_3BiI_6 thin films by spin coating with hot-casting (SPC-HC). Schematic illustration, along with cross-sectional and top-down SEM images of Ag_3BiI_6 thin films fabricated with (a, c, d) and without (b, f, g) antisolvent treatment with toluene (TL). (e) Photographs demonstrating the annealing process of the samples fabricated with antisolvent treatment, resulting in a gradual decomposition of the Ag_3BiI_6·8DMSO adduct[20] and formation of smooth mirror-like Ag_3BiI_6 films. In contrast to the top-down SEM image in part (d) that gives the impression of a compact film, the cross-sectional SEM image in part (c) reveals large holes at the bottom of the film. The samples fabricated without antisolvent treatment (f, g) feature rough, columnar morphology. Reproduced with permission from I. Turkevych, presented at the MNC-2020 conference, 33 Osaka, Japan, Nov. 9, 2020.[112]

In particular, a thick absorber layer is required in this planar or mesosuperstructured device archtiecture. However, Ag-Bi-I (and likely also Cu-Bi-I and Cu-Ag-Bi-I) have shorter diffusion lengths (L_D) than LHPs. Rather than using a thick planar thin film, the extremely thin absorber (ETA) heterojunction structure could be an effective alternative to alleviate the issue of the short L_D. In the ETA heterojunction, the absorber layer is sandwiched between the highly structured ETLs and HTLs (Fig. 19(b)). The absorber can therefore be thinner than the L_D, whilst light trapping in the nanostructured device ensures high optical absorption. The ETA structure can therefore significantly improve the collection probability of the photogenerated carriers, because they do not need to travel over large

distances before separation. Another important advantage of the ETA structure is more efficient light scattering, which increases the optical path through the device and thereby enhances photon absorption. As a result, the photocurrent of the solar cell can be maximized by a separate optimization of optical and electronic thicknesses of the absorber layer. Ag-Bi-I, Cu-Bi-I and Cu-Ag-Bi-I solar cells with the ordered ETA structure have not been realized yet, however, there are several works that demonstrate structured absorbers with a disordered bulk-heterojunction, such as phase separated $0.5Ag_3Bi_2I_9$-$Cs_3Bi_2I_9$,[102] $CuBiI_4$ mixed with doped spiro-OMeTAD or PTB7,[88] and Ag_2BiI_5 mixed with MWCNT or RGO.[104]

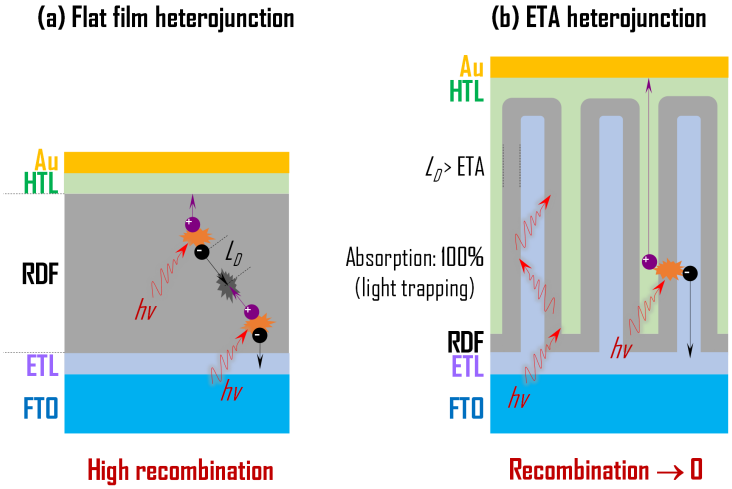

Figure 19: Advantages of the Extremely Thin Absorber (ETA) heterojunction structure for Cu-Ag-Bi-I solar cells. The ETA heterojunction structure is an effective approach to alleviate the issue of the short L_D and associated high non-radiative recombination rate. In contrast to the flat film heterojunction (a), the absorber layer, which is sandwiched between highly structured ETLs and HTLs in the ETA heterojunction (b), is thinner than the L_D, while the trapping of light ensures sufficient light absorption in the thin absorber layer.

3.1.4 Using Additives to Improve Photovoltaic Performance

As mentioned earlier, compositional engineering in Ag-Bi-I films has a significant effect on their photovoltaic performance. There have been several works that studied elemental substitutions in Ag-Bi-I compounds with Cs,[78] Sb,[26] Br[59] and S,[74] and a detailed discussion of the effects of doping with these elements is given in Section 2.1.5. In terms of photovoltaic

performance, the additive that has led to the highest PCE so far has been S incorporation into Ag-rich rudorffites. These compounds, with a nominal composition of $Ag_3BiI_{5.92}S_{0.04}$, demonstrated a PCE 5.56%,[74] which is currently the record performance amongst all Ag-Bi-I solar cells (Table 4). These increases in PCE were driven by an increase in J_{SC} from 11.2 mA cm^{-2} for Ag_3BiI_6 without S incorporation, to 14.7 mA cm^{-2} with 4% S incorporation (Table 4).[74] As can be seen from Fig. 17a, these were among the highest J_{SC}s reported for the Ag-Bi-I system. The increase in J_{SC} was due to an increase in the EQE, as well as a reduction in the optical bandgap from 1.87 eV (no S) to 1.82 eV (4 at.% S), which enhanced light absorption. As discussed in Section 2.1.5, the reduction in bandgap came about from the VBM being raised. Further increases in S incorporation reduced the bandgap more, but were accompanied by further decreases in the V_{OC} (see Table 4). Pai *et al.* attributed these reductions in V_{OC} to an increase in the density of recombination centers.[74]

3.1.5 Device Stability

Several groups have reported stable performance of unencapsulated Ag-Bi-I photovoltaics when stored in ambient air, dry air, or in a N_2-filled glovebox.[22,26,40,45,59,67,74,78,96,101,107] A range of stability tests have been conducted, from 10 days[22] to 77 days[59] in ambient air. In these tests, the devices were stored in the designated testing environment, and measured under 1-sun illumination at regular time intervals. In most cases, only a very small decrease in PCE was observed, on the order of 5–15%.[22,45,74] In the case of $AgBi_2I_7$ doped with 10% Br, a slight improvement in PCE was observed after storing in ambient air in the dark for 77 days, and this was attributed to changes in the TQ1 HTL (see footnote of Table 4 for full name) after oxygen exposure, since the increase in PCE correlated with an increase in J_{SC}.[59] In addition, Lu *et al.* found that $AgBiI_4$ demonstrated greater thermal and photo-stability than$MAPbI_3$ perovskite. In thermogravimetric analysis measurements, the onset in mass loss for $AgBiI_4$ was 260 °C (due to BiI_3 sublimation), whereas the onset temperature for the perovskite was 200 °C (due to methylammonium iodide removal).[45] When pristine films

were sealed in an inert-gas environment and exposed to 1-sun illumination for up to 3 h, $AgBiI_4$ showed no phase degradation, whereas the perovskite formed a PbI_2 impurity peak after only 1 h.[45]

However, it will be important to also understand long term changes in PCE under continuous operation at the maximum power point. A work by Zhang *et al.* found that although the PCE decreased by less than 5% after repeated measurements over a period of 500 h in air, under continuous operation, the PCE decreased by approximately 40% under continuous operation for 50 s.[101] These changes may arise from heat-induced, ion migration or changes to the device at the interfaces during operation, and should be investigated further. Indeed, as discussed earlier in Section 2.4.1 (on the effects of AgI impurities) and Section 2.4.2 (on ion migration), ionic species can be released and migrate to the top metal electrode, causing corrosion and performance degradation.[56] This occurs even for metal electrodes that would normally be considered inert, such as Au, and motivates further work to understand the mechanisms involved, as well as mitigation strategies (*e.g.*, developing more inert electrodes). Achieving stable operation at the maximum power point and under continuous illumination will be important for Ag-Bi-I photovoltaics to ultimately pass standard accelerated degradation tests.[113,114]

In summary, from Table 4 and Fig. 17, we can see that reasonably high parameters of 15 mA cm^{-2} for J_{SC},[74] 0.83 V for V_{OC},[101] and 76% for FF[39] have been demonstrated in different devices. This suggests that a properly optimized device can potentially demonstrate a PCE of around 10%. We can suggest that the next generation of these halide absorber solar cells should adopt Ag- or Cu-rich compositions for absorber layers with heterovalent doping and the ETA heterojunction device structure.

3.2 Indoor Light Harvesting

Indoor photovoltaics (IPVs) are gaining increasing attention as a highly promising route

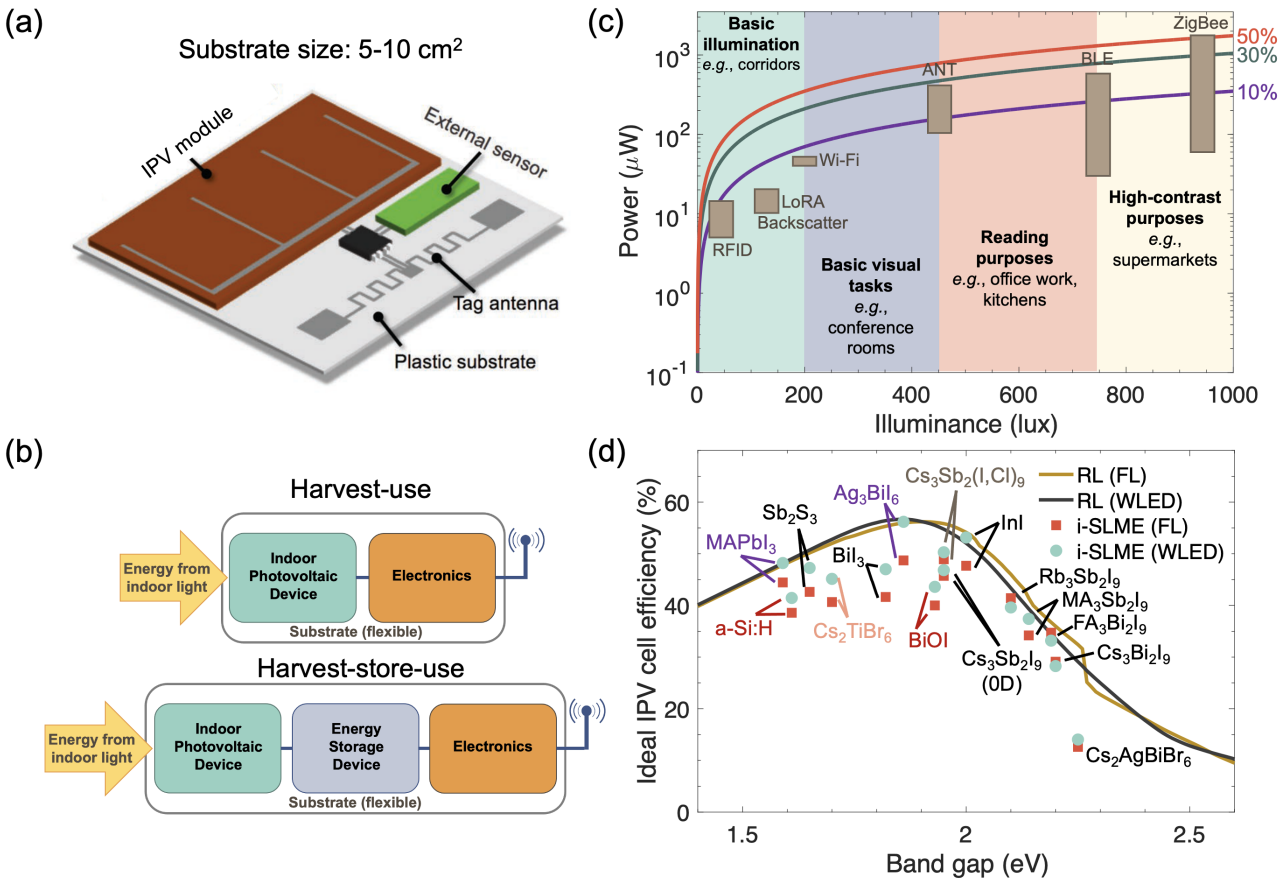

Figure 20: Motivation for using Ag-Bi-I for indoor photovoltaics (IPVs). (a) Schematic of a radiofrequency identification (RFID) tag with an IPV. Reproduced with permission from Ref.[115] Copyright 2019, Wiley. (b) Illustration of IoTs nodes based on the 'harvest-use' and 'harvest-store-use' concepts.[24] (c) Power produced by IPV over a range of PCEs under different illuminances. 1000 lux illuminance is taken to have 350 μW cm^{-2} irradiance. Power consumption of communication protocols from Ref.[116] (d) Radiative limit and indoor spectroscopic limited maximum efficiencies (i-SLMEs) under white light emitting diode (WLED) and fluorescent (FL) light sources. Reproduced under the terms of the CC-BY license from Ref.[24] Copyright 2021, The Authors.

[1]RDF = rudorffite, spiro-OMeTAD = 2,2,7,7-tetrakis(N,N-di-p-methoxyphenyl-amine)9,9-spirobifluorene, 4A1N = 4-aminoaphthalene-1-sulfonate, P3HT = poly(3-hexylthiophene-2,5-diyl), PTAA = poly[bis(4-phenyl)(2,4,6-trimethylphenyl)amine], TQ1 = poly[[2,3-bis(3-octyloxyphenyl)- 5,8-quinoxalinediyl]-2,5-thiophenediyl]

Table 5: Performance of Ag-Bi-I and Cu-Ag-Bi-I indoor photovoltaics. The average value and uncertainty for each parameter is shown, along with the value of the champion device in brackets, where all of this information is available. Otherwise, the champion performance reported is shown. The light source used in these reports were white light emitting diodes (WLEDs), except for the report shown of DSSCs, which were measured under fluorescent (FL) lighting. Please note that not all devices were measured under the same illumination conditions, and the standards for indoor photovoltaic measurements had not been published when these reports were made.[1]

Year	Compound	Device Structure	Illuminance (lux)	P_{out} (μW cm^{-2})	PCE (%)	V_{oc} (V)	J_{sc} (μA cm^{-2})	FF (%)	Ref.
2020	DSSC (FL)	FTO/TiO_2/XY1:L1/electrolyte/PEDOT:PSS/FTO	1000	103.1	34.0	0.91	147	77	117
2020	DSSC (FL)	FTO/TiO_2/XY1:L1/electrolyte/PEDOT:PSS/FTO	500	49.5	32.7	0.88	73.4	77	117
2020	DSSC (FL)	FTO/TiO_2/XY1:L1/electrolyte/PEDOT:PSS/FTO	200	19.0	31.4	0.84	29.0	78	117
2021	LHP (triple cation)	FTO/TiO_2/LHP/Lycopene/spiro-OMeTAD/MoO_x/Ag	1000	111.7	40.2	0.85	248	53	119
2023	LHP ($CsPbI_3$)	FTO/TiO_2/4A1N/LHP/spiro-OMeTAD/Ag	1062	130±7 (138)	39±2 (41)	1.05±0.01 (1.07)	150±10 (160)	81±1 (83)	120
2022	Cu_2AgBiI_6 (with HI)	FTO/c-TiO_2/RDF/spiro-OMeTAD/Au	1000	17±1 (22)	3.7±0.3 (4.7)	0.54±0.04 (0.60)	62±7 (80)	63±1 (65)	110
2022	Cu_2AgBiI_6 (w/o HI)	FTO/c-TiO_2/RDF/spiro-OMeTAD/Au	1000	6±2 (11)	1.3±0.5 (2.3)	0.46±0.05 (0.54)	25±6 (36)	57±4 (64)	110
2022	$ATBiI_4$	FTO/c-TiO_2/RDF/PTAA/Ag	1000	1.56	0.52	0.71	4.35	50.6	121
2022	$ATBiI_4$	FTO/c-TiO_2/RDF/PTAA/Ag	500	0.82	0.54	0.68	2.55	47.0	121
2023	$Cu_2Ag(Bi-Sb)I_6$	FTO/c-m-TiO_2/RDF/spiro-OMeTAD/Au	1000	n.r.	8.3±0.6 (9.5)	0.55±0.01 (0.56)	116±4 (128)	68.5±0.7 (70.0)	122

to sustainably powering Internet of Things (IoTs) devices.[24,116] The IoT is an ecosystem of interconnected devices that can communicate with each other via the cloud. Such an ecosystem is considered to embed 'intelligence' into infrastructure, by making them responsive and adaptable (*i.e.*, smart homes, smart factories, smart agriculture, etc.). The IoT is predicted to substantially improve quality of life, increase productivity and reduce CO_2eq emissions by making processes more efficient.[24,115–118] As the IoT ecosystem increases in size towards the trillion-node level, a critical question is how these autonomous devices can be sustainably powered. Currently, there is a heavy reliance on batteries, which have limited lifespan, and this could not only restrict the size and number of applications of the IoT, but also lead to substantial waste.[24] In this context, harvesting ambient light as a power source for IoT devices is highly appealing. IPVs can be integrated to the IoT node (Fig. 20a), and could either directly power the IoT device (harvest-use), or both power the IoT device and recharge an energy storage device (*e.g.*, battery or supercapacitor) that then powers the device in the dark (Fig. 20b, harvest-store-use). IPVs are advantageous over other energy harvesters because ambient light is a reliable source of energy that is widely available, and there is no need for the IPVs to be directly in contact with the light source. Furthermore, the energy density of indoor light sources is high compared to other sources of energy, typically up to 300-350 μW cm^{-2} under 1000 lux illuminance. Fig. 20c illustrates that the instantaneous power IPVs can harvest under direct illumination is sufficient for a wide range of low-power communications protocols commonly used for wireless sensors[116] with a relatively compact area of 10 cm^2. The excess energy can be stored to power the IoT node in the dark. Given the highly predictable availability of ambient lighting, the power management system and total power harvested by the IPV can be designed for. As such, the IPV industry is one of the fastest growing photovoltaic markets.[116]

Cu-Ag-Bi-I materials can have an important impact on the IPV field. Commercial IPVs are dominated by hydrogenated amorphous silicon (a-Si:H). However, owing to the high

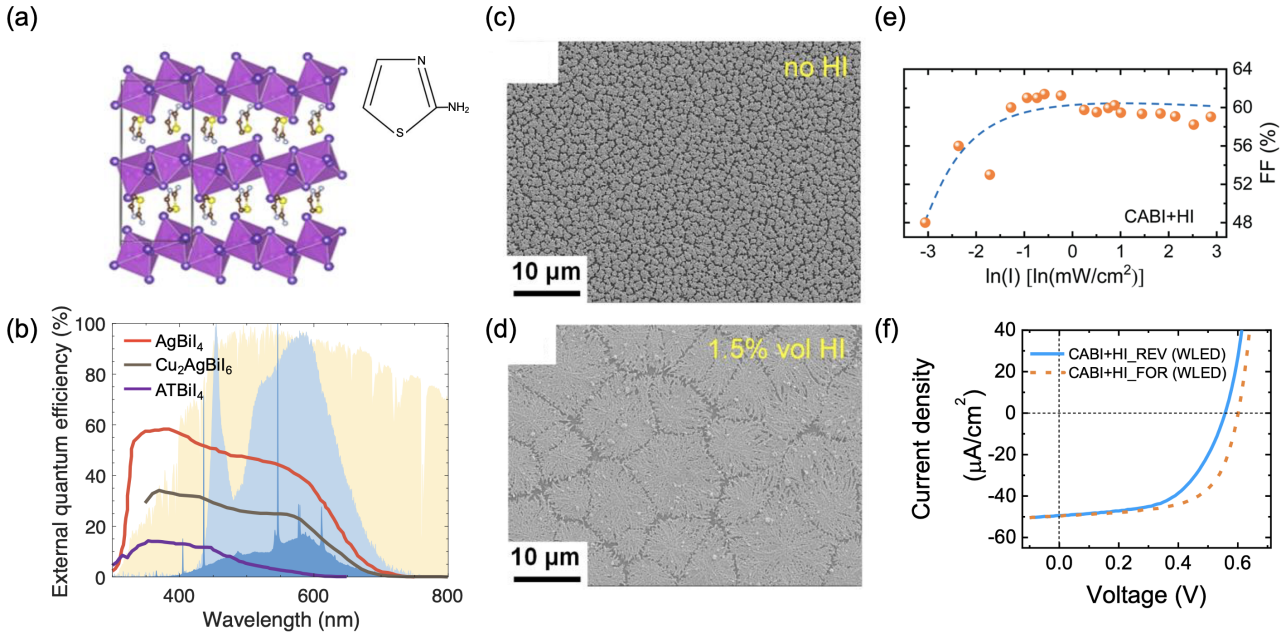

Figure 21: Performance of recently-reported Ag-Bi-I and Cu-Ag-Bi-I IPVs. (a) Crystal structure of $ATBiI_4$, with the structure of AT = 2-aminothiazolium inset. Reproduced under the terms of the CC-BY license from Ref.[121] Copyright 2022, The Authors. (b) EQE against wavelength of incident light for $AgBiI_4$,[46] Cu_2AgBiI_6[110] and $ATBiI_4$ IPVs, compared to the spectra for white light emitting diode (light blue), fluorescent (FL) light sources, as well as 1-sun (yellow). Morphology of Cu_2AgBiI_6 (c) without and (d) with 1.5% HI added to the precursor solution. (e) Fill factor of Cu_2AgBiI_6 IPVs under 100-45000 lux illuminance. (f) Forward and reverse sweeps for Cu_2AgBiI_6 IPVs. Parts (c)-(f) reproduced under the terms of the CC-BY license from Ref.[110] Copyright 2022, The Authors.

defect density in a-Si:H, the PCEs are limited up to 21%,[123] and are mostly in the 4.4–9.2% range.[124,125] Higher PCEs under indoor light sources have been achieved by organic photovoltaics (to 30.3%),[126] dye-sensitized solar cell (DSSC; to 34.0%, Table 5)[117] and lead-halide perovskite photovoltaics (LHP; to 41.2%, Table 5).[120] However, organic IPVs are limited by high synthesis costs, especially for the complex molcules used in the most efficient devices.[127] LHPs are limited by the presence of toxic and bioaccumulative Pb in a readily-accessible form, and may be prevented by legislation (*e.g.*, EU restriction of hazardous substances directive) for use in consumer electronics.[128] Furthermore, LHPs, organic PV and DSSCs are commonly processed using large quantities of toxic solvents (*e.g.*, DMF or chlorobenzene).[12] Simple inorganic compounds that can be processed using low thermal-

budget methods using low-toxicity solvents (*e.g.*, DMSO[12]) or solvent-free are therefore highly appealing. Hoye, Pecunia and co-workers calculated the efficiency limit expected based on the measured optical absorption spectra (*i.e.*, iSLME) for a range of inorganic perovskite-inspired materials (PIMs), and found that Ag_3BiI_6 had radiative limit and indoor spectroscopic limited maximum efficiencies (i-SLMEs) reaching up to 56.2% under 1000 lux WLED illumination for Ag_3BiI_6 (Fig. 20d).[23,24] The high i-SLMEs were due to the Ag-Bi-I compounds having an optimal bandgap (close to 1.9 eV) for harvesting visible indoor lighting (WLED or FL), as well as its high absorption coefficients (see Fig. 6).[38] These factors, coupled with the ability to synthesize Ag-Bi-I semiconductors using a small number of steps (compared to organic molecules), and compatibility with processing by nontoxic solvents or solvent-free methods, make the class of materials promising.

The demonstration of high i-SLMEs for Ag_3BiI_6 was only made in 2021.[23] Since then, Turkevych *et al.*,[46] Grandhi *et al.*,[110] and Arivazhagan *et al.*[121] have reported initial findings on Cu-Ag-Bi-I IPVs. The compounds explored were $AgBiI_4$, Cu_2AgBiI_6 and $ATBiI_4$, respectively, where AT = 2-aminothiazolium. The molecular structure of AT, along with the crystal structure of $ATBiI_4$, are shown inset in Fig. 21a (see Section 2 for the crystal structure of $AgBiI_4$ and Cu_2AgBiI_6). Unlike the all-inorganic compounds, the large size of AT results in a one-dimensional structure, comprised of edge-sharing chains of BiI_6 octahedra.[129]

The EQE spectra from the three compounds are shown in Fig. 21b. All three materials have bandgaps in the range of 1.78–1.96 eV,[46,110,121] and the EQE onset for these devices was from approximately 700 nm wavelength, with an inflection point close to the optical bandgap. In the case of Cu_2AgBiI_6, the authors reported a four-fold increase in PCE under WLED lighting compared to 1-sun illumination, due to the better spectral match of their devices to indoor lighting.[110] Importantly, the V_{oc} under 1000 lux illuminance remained relatively close to the V_{oc} under 1-sun illumination (0.60 V *vs.* 0.70 V, respectively).[110] The $ATBiI_4$ devices exhibited lower EQEs and lower device performance (Table 5), which may be due to discontinuities in the film and possibily BiI_3 impurities. High trap densities on the order

of 10^{18} cm^{-3} were also found from space-charge limited current densities measurements, and this would also limit performance.[121]

Challenges with morphology and phase impurities were found to limit the efficiency of Cu_2AgBiI_6 IPVs. An SEM image of Cu_2AgBiI_6 films is shown in Fig. 21c. Attempts were made to improve this morphology by adding small quantities of HI to the precursor solution. Whilst this led to larger domains (Fig. 21d), discontinuities in the film remained. Intensity-dependent measurements showed that the FF decreased at low illuminances (Fig. 21e), and this was attributed to the effects of morphology leading to dark currents that play a more substantial role under indoor lighting, given the low photocurrents at low illuminances. Furthermore, intensity-dependent V_{OC} measurements showed that the diode ideality factor increased from 1.2 (0.1–1 sun) to 1.6 (100–45 000 lux), suggesting that under lower illuminances, non-radiative recombination due to bulk defects played a greater role. Indeed, phase impurities were found from XRD and PL measurements, and some of these could have acted as recombination centers.[110] Very recently, the same group reported an improvement in the morphology, along with a reduction in defect density, by alloying a small quantity of Sb into the pnictogen site. This led to an improvement in the PCE under 1000 lux from 5.52 % to 9.53%, mainly due to an increase in the J_{SC} from 72 μA cm^{-2} to 128 μA cm^{-2}.[122]

Across all Cu-Ag-Bi-I IPVs reported thus far, hysteresis was found in the photovoltaic performance (Fig. 21f). All three groups used a similar device architecture (refer to Table 5) to that commonly used for LHPs, from which hysteresis is commonly reported. Thus, in addition to efforts to suppress ion migration, it may also be important to investigate alternative electron/HTLs that could reduce hysteresis effects through interface passivation or by inhibiting ionic motion.[130] Furthermore, Al-Anesi *et al.* reported a reduction in the hysteresis of Cs_2AgBiI_6 at high illuminance through Sb alloying, which may be due to a reduction in defect density.[122]

Thus, there have already been encouraging initial results on Cu-Ag-Bi-I IPVs, with PCEs reaching into the range of commercial-standard a-Si:H IPVs, and are at a comparable level

to initial BiOI and vacancy-ordered triple perovskite PIM IPVs.[23] This sets the stage for future efforts at improving the morphology, optoelectronic quality, and device structure to bring Cu-Ag-Bi-I towards their potential as IPVs.

3.3 Photodetectors

Photodetectors have important applications in medical imaging, surveillance cameras, machine vision, optical communications, and many more (Fig. 22a).[131] Whilst crystalline inorganic semiconductors (such as Si or InGaAs) are well established in commercial photodetectors, with high detectivity $>10^{11}$ Jones, rapid advances in new applications calls for innovations in imaging technology.[131] Solution-processed thin film semiconductors are particularly appealing for many reasons. They can be directly incorporated onto read-out integrated circuits, which circumvents the cumbersome integration of conventional semiconductors, allowing greater miniaturization. Solution-processed semiconductors are also compatible with large-area manufacturing techniques, such as roll-to-roll processing, spray coating, doctor blading or inkjet printing.[132] Furthermore, solution-processed thin films can be integrated with flexible substrates, which is important for wearable electronics, or integration into IoTs sensor nodes.[133] Thus, chalcogenide colloidal quantum dots, organic materials and LHPs have gained significant attention as novel photodetector materials, and in some cases, detectivities have exceeded those of Si-based photodetectors in the visible wavelength range.[131] Cu-Ag-Bi-I materials are worth investigating for photodetection, because of their lower toxicity compared to Cd- or Pb-based colloidal quantum dots and LHPs, and their potentially simpler fabrication process compared to organic materials. Up to now, Ag-Bi-I and Cu-Bi-I compounds, as well as Ag/Cu alloys, have been investigated (Table 6), covering the UV and visible (UV-VIS) wavelength ranges (Fig. 22a).

Thus far, groups developing Cu-Ag-Bi-I photodetectors have adopted either a lateral photoconductor (PC) structure (PC; Fig. 22b) or vertical photodiode (PD) structure (PD;

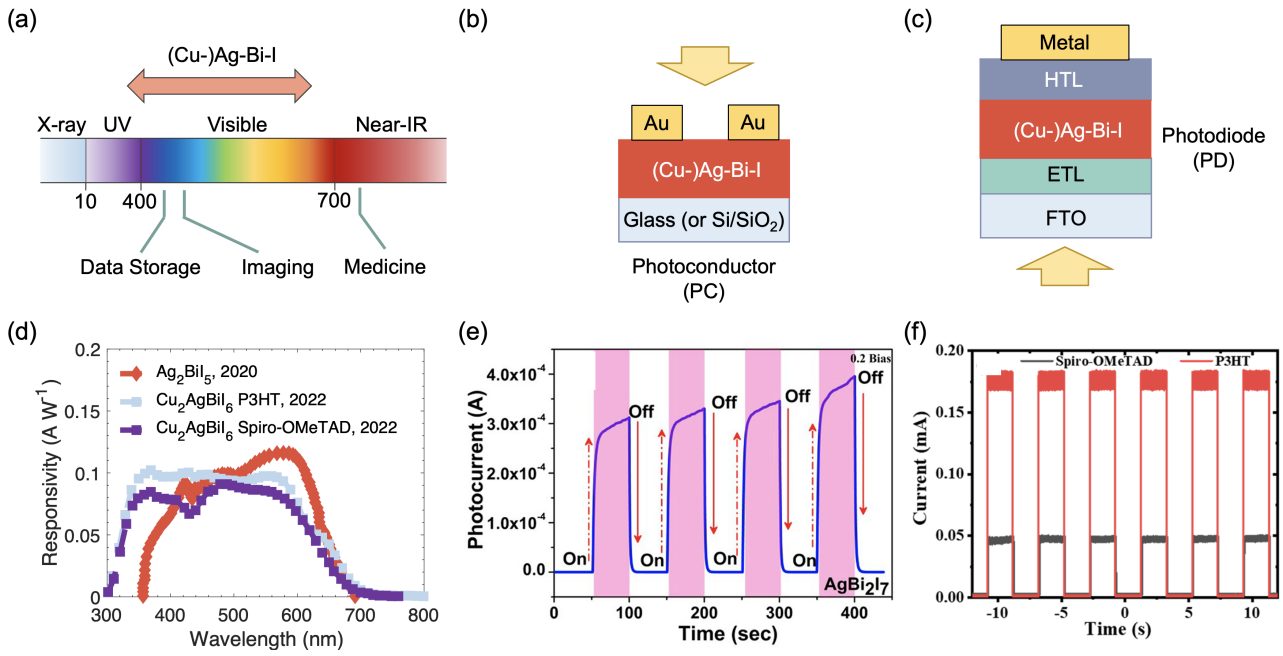

Figure 22: Application of Cu-Ag-Bi-I materials in solution-processed photodetectors. (a) Application of photodetectors at different wavelengths,[131] and the wavelengths Cu-Ag-Bi-I photodetectors have been demonstrated over thus far. Please note that Ag-Bi-I X-ray detectors have also been demonstrated, as elaborated on in Section 3.4. Illustration of photodetectors made in the (b) photoconductor (PC) and (c) photodiode (PD) structure, as reported for Cu-Ag-Bi-I absorbers. (d) Comparison of the spectral responsivity reported in Ref.[41] for Ag_2BiI_5 and Ref.[93] Cu_2AgBiI_6. Rise and fall in photocurrents under chopped illumination for (e) $AgBi_2I_7$ nanocrystal (under AM 1.5G illumination) and (f) Cu_2AgBiI_6 (under 405 nm wavelength illumination) PDs. Part (e) reproduced with permission from Ref.[134] Copyright 2020, American Chemical Society. Part (f) reproduced with permission from Ref.[93] Copyright 2022, American Chemical Society.

Table 6: Champion reported performance of halide Cu-Ag-Bi-I for photodetectors. The spectral response noted refers to the spectra the photodetectors were tested under, and not to the full range of spectra the devices could in principle work under (UV and VIS in all cases). Note: n.r. = no report.[2]

Year	Spectral Region	Compound	Device Type	EQE (%)	Peak Responsivity (A W^{-1})	D* (Jones)	on/off ratio	Rise time (s)	Fall time (s)	Ref.
2020	UV-VIS	$CuBiI_4$	PC	n.r.	0.50	3.8×10^7	1.9	n.r.	n.r.	[81]
2020	UV-VIS	$AgBi_2I_7$	PD	n.r.	n.r. (VIS) 0.15 (UV)	n.r.	6.5×10^4 (VIS) 280 (UV)	<0.3 s	<0.3 s	[134]
2020	UV-VIS	Ag_2BiI_5	PD	n.r.	n.r.	n.r.	2.9×10^2 (VIS, 0.1 V) 5.6×10^2 (VIS, 0.2 V)	n.r.	n.r.	[134]
2020	VIS	Ag_2BiI_5	PD	27	0.12	2×10^{11}	n.r.	0.075–0.25	0.024–0.095	[41]
2021	VIS	$AgBiI_4$	PC	n.r.	4.2×10^5	2.4×10^7	20.4	0.81	0.80	[135]
2021	VIS	Ag_2BiI_5	PC	n.r.	8.6×10^5	3.8×10^7	39.6	1.99	2.04	[135]
2021	VIS	Cu_2BiI_5	PC	0.012	45×10^{-6}	n.r.	n.r.	n.r.	n.r.	[136]
2022	UV-VIS	Cu_2AgBiI_6	PD	35	0.10	1.5×10^{12}	n.r.	0.51×10^{-3}	1.51×10^{-3}	[93]

[2]PC = photoconductor, PD = photodiode

Fig. 22c), as shown in Table 6. The PC structure is simpler, and involves depositing identical metal electrodes onto the Cu-Ag-Bi-I. The increase in conductivity following light absorption is read by applying an external voltage. In the case of Cu-Ag-Bi-I, the PD structures adopted have been identical to the architectures used in photovoltaics, although the thicknesses and processing of the individual layers are often different between these two applications because of the different ways in which they operate. In PDs, the built-in potential assists with the extraction of the photogenerated charge-carriers, and this is often further assisted by the application of an external bias.[131]

The key performance metrics for photodetectors are related to their efficiency, noise and speed. Efficiency includes the EQE, responsivity and specific detectivity. The responsivity (R) is the ratio of the current extracted to the optical power input, and can be calculated from the EQE (η_{EQE}) from Equation 1, where $h\nu$ is the photon energy, and q the fundamental charge.

$$R = \frac{\eta_{EQE} q}{h\nu} \tag{1}$$

Ultimately, the overall figure of merit for the sensitivity of photodetectors is the specific detectivity (D*), which can be calculated from R, the noise current (I_N), the noise bandwidth (B) used in measuring the noise current, and detector active area (A) from Equation 2. Noise is the random fluctuation in the output current, and is often due to frequency-dependent flicker (1/f) noise (due to trapping in the bulk or surface) or frequency-independent thermal noise (due to the random thermal motion of charge-carriers) and dark shot noise (due to dark current).[137] Often, in calculating D*, groups would consider I_N to be solely due to the dark shot noise, but this would often lead to an over-estimation of D*, since many other sources of noise also play a role. For example, for Ag_2BiI_5 PDs, the D* would have been 2×10^{12} Jones if only shot noise was considered. But after considering thermal noise as well as shot noise, the D* reduced by an order of magnitude to 2×10^{11} Jones.[41] To account for all sources of noise and accurately determine D*, the noise current as a function of frequency

should be directly measured. However, the specific detectivities reported by all other groups in Table 6 were calculated based only on the dark current noise.[81,93,135,136]

$$D^* = \frac{R\sqrt{AB}}{I_N} \tag{2}$$

Finally, the speed of the photodetector is commonly characterized by its response time, which is usually defined by the time for the photocurrent to increase from 10% to 90% of the maximum photocurrent under chopped illumination (rise time), or decrease from 90% to 10% (fall time).[93,131] Another metric for the speed of photodetectors is the maximum frequency they can operate at (i.e., the cut-off frequency).[131] However, this parameter has not yet been reported for Cu-Ag-Bi-I photodetectors.

A comparison of the responsivity of recently-reported Cu-Ag-Bi-I PD is shown in Fig. 22d, showing the ability of these devices to operate over a wide spectral range from the UV to visible. Higher responsivity values reaching 0.5 A W^{-1} were reported for $CuBiI_4$ photoconductors under AM 1.5G illumination (100 mW cm^{-2}) by Qu *et al.*[81] These photoconductors were made in a lateral configuration, in which both Au electrodes were deposited onto the front surface of the $CuBiI_4$ film. This was important to achieve rectification with an on/off ratio of 1.9, since pinholes were present in the morphology of the films,[81] and a high leakage current may have occurred if a vertical device structure were used.

Much higher responsivities on the order of 10^5 A W^{-1} were reported for $AgBiI_4$ and Ag_2BiI_5 photoconductors by Prasad *et al.*[135] The films had a more compact morphology than the $CuBiI_4$ films made by Qu *et al.*,[81] and key to achieving this was a post-annealing process at 125 °C for 15 min, which reduced the density of pinholes and increased the size of grains.[135] The responsivity was calculated from the ratio of the photocurrent to incident power, measured under 454 nm, 532 nm and 633 nm wavelength excitation at a power density of 0.1 mW cm^{-2} and 1 V bias.[135] However, these responsivities significantly exceed the ideal responsivities (when EQE is 100%), which are <1 A W^{-1} at these excitation wavelengths. A possible explanation for this is photoconductive gain, in which the accumulation of majority

charge-carriers can lead to measured EQEs exceeding 100%.[138]

An advantage of the PD structure over the PCstructure is that a built-in field is already present without any external bias applied. PD are therefore capable of being self-powered, which is important for low-power applications, such as in sensor nodes for the IoTs.[24,41] Zhang *et al.* reported self-powered Cu_2AgBiI_6 PD, which had a responsivity of 0.085 A W^{-1} under 405 nm wavelength excitation.[93] The spectrally-resolved responsivity over the UV and visible wavelengths is shown in Fig. 22d, from which it can be seen that improved performance was obtained using P3HT as the HTL rather than spiro-OMeTAD. This was because devices with P3HT had a higher J_{SC}. Zhang *et al.* also found that passivating the surface of the Cu_2AgBiI_6 films with phenethylammonium iodide (PEAI) led to an increase in the built-in potential, and this improved the photocurrents obtained.[93]

A photoresponse further in to the UV was obtained from $AgBiI_4$, Ag_2BiI_5 and $AgBi_2I_7$ quantum dots (QDs) by Premkumar *et al.*, with an average size of 5 nm.[134] These quantum dots were found to have stronger excitonic characteristics and blue-shifted absorption compared to bulk films, with the excitonic peaks of $AgBiI_4$, Ag_2BiI_5 and $AgBi_2I_7$ occurring at 2.99, 3.04 and 2.91 eV, respectively.[134] These quantum dots were used in PDs, with the device structure: FTO/nc-TiO_2/QD/MoO_3/Al, in which the nc-TiO_2 layer was a film comprised of 50 nm-sized nanocrystals. The photocurrent at 0.1 V and 0.2 V applied bias was measured under 1-sun illumination, and the highest on/off ratios were reached for the $AgBi_2I_7$ photodiode, with a value of 6.5×10^4 (Table 6). The $AgBi_2I_7$ PDalso exhibited the best performance as a UV detector (under 390 nm wavelength excitation), with an on/off ratio of 280 and responsivity of 0.15 A W^{-1}. In these UV detectors, the MoO_3 layer was removed. Under both 1-sun and UV illumination, all devices had a long rise time $<$0.3 s, with a sawtooth pattern in the photocurrent under chopped illumination (Fig. 22e), and this was attributed to unrelaxed electrons in excited state energy levels.[134] Prasad *et al.* reported longer response times for $AgBiI_4$ and Ag_2BiI_5 thin film PDs, on the order of 0.8 s ($AgBiI_4$) and 2 s (Ag_2BiI_5).[135] By contrast, much shorter response times on the order of milliseconds

were reported by Zhang *et al.* for Cu_2AgBiI_6 (Fig. 22f).[93]

An important advantage widely reported for Cu-Ag-Bi-I photodetectors is their stability under ambient environments. For $CuBiI_4$, Cu_2AgBiI_6, as well as the Ag-Bi-I QDs from Premkumar *et al.*, the photocurrent under chopped illumination was measured for 100–500 s, and in all cases no decrease in performance was found.[81,93,134] Prasad *et al.* kept their $AgBiI_4$ and Ag_2BiI_5 PDs in ambient air for 15 days, and found no significant change in current-voltage curves.[135] As another example, Shaji and co-workers found that Cu_2BiI_5 photodetectors remained operational after storage for 30 days in ambient air, with photocurrents that were similar to or less than an order of magnitude smaller than fresh devices.[136]

Thus, Cu-Ag-Bi-I are potential solution-processable semiconductors for next-generation photodetectors, with promising stabilities in air. The development of these materials into photodetectors is still at an early stage and warrants further development, particularly in improving the processing and device architecture to further improve the performance. It will also be important to measure the noise current of these devices to more accurately calculate the specific detectivity, and elucidate in more detail the factors influencing the response time of these devices.

3.4 Broader Potential Applications

A core advantage of Bi-I-based materials is the high atomic number of these elements, which is important for efficiently attenuating ionizing radiation.[139] Ionizing radiation is widely used for non-invasive diagnostics, such as in security screening, detection of radionuclides from nuclear waste, or medical imaging. Across all applications, detectors with higher sensitivity, and the ability to detect lower dose rates (*i.e.*, lower limit of detection, LoD) are desired. For example, in medical imaging, the standard dose rate is 5500 nGy_{air} s^{-1}, which is four orders of magnitude above background levels of ionizing radiation, thus posing a risk to the patient during medical scans.[139,140] Achieving detectors that can directly convert X-ray photons to electrical signals with lower LoD and higher sensitivity requires

materials with high average atomic numbers (Z_{av}) and density, since the linear attenuation coefficient is proportional to $\rho {Z_{av}}^4$.[34,139,140] $AgBi_2I_7$ was recently investigated for X-ray detection, and was found to have linear attenuation coefficients (Fig. 23a) over an order of magnitude larger than amorphous selenium (α-Se), which is the industry-standard material for direct-conversion detectors in medical imaging.[34,139] This is particularly advantageous for detecting higher-energy X-rays. For example, Tie *et al.* showed that whilst several millimeters thick α-Se would be needed to attenuate 100 keV X-rays, only 0.5 mm of $AgBi_2I_7$ would be needed.[34] Furthermore, $AgBi_2I_7$ single crystals were found to have electron/hole mobilities on the order of hundreds of $cm^2\ V^{-1}\ s^{-1}$, with mobility-lifetime ($\mu\tau$) products on the order of $10^{-3}\ cm^2\ V^{-1}$ for both electrons and holes.[34] X-ray detectors were made with a PC structure (Fig. 23b, inset), in which the $AgBi_2I_7$ single crystal was sandwiched between two parallel Au electrodes. The photocurrent was measured from 11,403 $nGy_{air}\ s^{-1}$ down to 105 $nGy_{air}\ s^{-1}$ (Fig. 23b) from a 60 kVp W-target anode X-ray tube, with 43 keV mean photon energy. From these measurements, the LoD was found to be 72 $nGy_{air}\ s^{-1}$ by extrapolating the signal-to-noise ratio down to 3, as shown in the inset of Fig. 23b.[34] This is a substantial improvement over the current medical standard, and the sensitivity obtained (282.5 $\mu C\ Gy_{air}^{-1}\ cm^{-2}$) exceeded that of α-Se (20 $\mu C\ Gy_{air}^{-1}\ cm^{-2}$).[34] These $AgBi_2I_7$ X-ray detectors also had higher sensitivities than the first report of $Cs_2AgBiBr_6$ double perovskite X-ray detectors (105 $\mu C\ Gy_{air}^{-1}\ cm^{-2}$),[140] but falls short of current state-of-the-art values for LHPs (now exceeding 10^4 $\mu C\ Gy_{air}^{-1}\ cm^{-2}$).[139] Lead-halide perovskite X-ray detectors have also achieved directly-measured LoD values below 40 $nGy_{air}\ s^{-1}$.[31] Roy Shaon *et al.* theoretically analyzed $AgBi_2I_7$ radiation detectors, and found that these devices have a predicted upper-limit in sensitivity of 313 $\mu C\ Gy_{air}^{-1}\ cm^{-2}$ at 20 keV (for mammography), and 2870 $\mu C\ Gy_{air}^{-1}\ cm^{-2}$ at 60 keV (for chest radiography).[47] It should be noted that the calculated upper limit in sensitivity of LHPs is only 8000 $\mu C\ Gy_{air}^{-1}\ cm^{-2}$,[141] yet sensitivities exceeding this have been reported, which may be due to multiplication effects, such as photoconductive gain.[141] Thus, there is scope for further improvements in the performance of

$AgBi_2I_7$ radiation detectors, and it will be important to determine and control the photoconductive gain (such as by controlling the device architecture), as well as understand the role of ion migration in these devices.

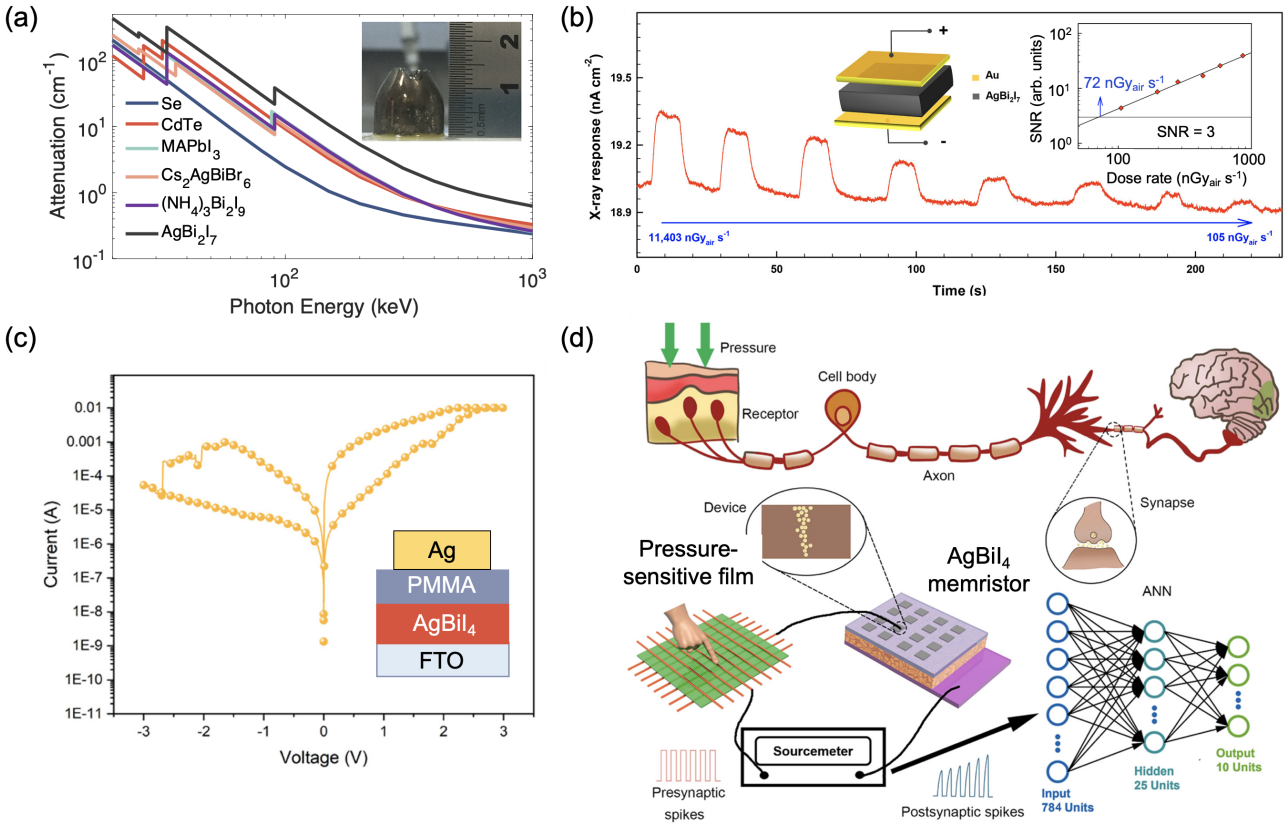

Figure 23: Broader applications of Ag-Bi-I in X-ray detectors and artificial synapses. (a) Attenuation coefficient of $AgBi_2I_7$ for ionizing radiation, with a photograph of the $AgBi_2I_7$ single crystal inset. (b) Photocurrent of $AgBi_2I_7$ single crystal photoconductors with different dose rates of X-rays. Inset is a schematic of the photoconductor, as well as the determination of the lowest detectable dose rate from the signal to noise ratio (SNR). Part (b) and inset to part (a) reproduced with permission from Ref.[34] Copyright 2020, American Chemical Society. (c) Typical resistive switching curve for $AgBiI_4$ memristors, with the device structure inset. (d) Illustration of how humans respond to tactile signals (top), and the replication of this system using a pressure-senstive film and $AgBiI_4$ memristors. Parts (c) and (d) reproduced with minor adaptations from Ref.[35] under the terms of the CC-BY-NC 3.0 license. Copyright 2022, The Authors.

Beyond photo-active applications, $AgBiI_4$ has also exhibited resistive switching.[35,142] Recently, there has been a surge of interest in developing novel materials for resistive switching random access memory (ReRAM) devices that could achieve high integration density, over-

come the scaling limitations of Si flash memory, and be compatible with polymer substrates for flexible memristors.[142] Ye *et al.* achieved compact $AgBiI_4$ films at a low processing temperature of 150 °C through dynamic hot casting, in which chlorobenzene was used as the antisolvent.[142] These films were integrated into a vertically-structured device, with a transparent conducting oxide (ITO[142] or FTO[35]) on the bottom electrode, and Ag as the top electrode (Fig. 23c). A thin layer of poly(methyl methacrylate), or PMMA, was used between the $AgBiI_4$ and Ag electrode to prevent the degradation of the $AgBiI_4$ layer by reactions with Ag. These devices exhibited low set and reset voltages of 0.16 V and -0.16 V, respectively, with an on/off ratio exceeding 10^4.[142] The on/off ratio is comparable with the highest reported for LHPs, and the set/reset voltage signicantly lower, which is important for achieving ReRAM with low power consumption. These devices exhibited excellent data retention, maintaining the resistivity in the high and low resistance states for up to 10^4 s (at a reading bias of 0.02 V). The endurance of the devices was also high, maintaining the resistive switching behavior after cycling 700 times. When built on flexible substrates, the $AgBiI_4$ exhibited inferior performance, with an on/off ratio on the order of 10^2, but this was durable after 1000 bending cycles, demonstrating the mechanical robustness of these devices.[142]

The proposed mechanism for resistive switching in the $AgBiI_4$ memristors was the formation of conducting Ag-based filaments. Although the PMMA layer prevented reactions between the $AgBiI_4$ and Ag, it was thin enough for Ag^+ cations to diffuse through to form these filaments.[142] However, in a later report, the same group increased the thickness of $AgBiI_4$ from 500 nm to almost 1 μm, which led to higher set/reset voltages (Fig. 23c).[35] The mechanism was proposed to be different for the thicker devices due to the reduction in the electric field with an increase in layer thickness, to the extent that it was insufficient to cause Ag filament formation. Rather, the resistive switching mechanism was proposed to be based on V_I defects.[35] These thicker devices exhibited a continuous reduction in resistivity during the set process (at 1.5 V) and increase in resistivity during the reset process (at

-1.5 V), which resembles the behavior of biological synapses. This led to the construction of an artificial sensor neural system based on a pressure-sensitive film and $AgBiI_4$ memristor artificial synapse feeding information to an artifical neural network that replicates the human tactile sensing system, as illustrated in Fig. 23d.[35] Ag-Bi-I semiconductors are therefore highly promising for neuromorphic computing.

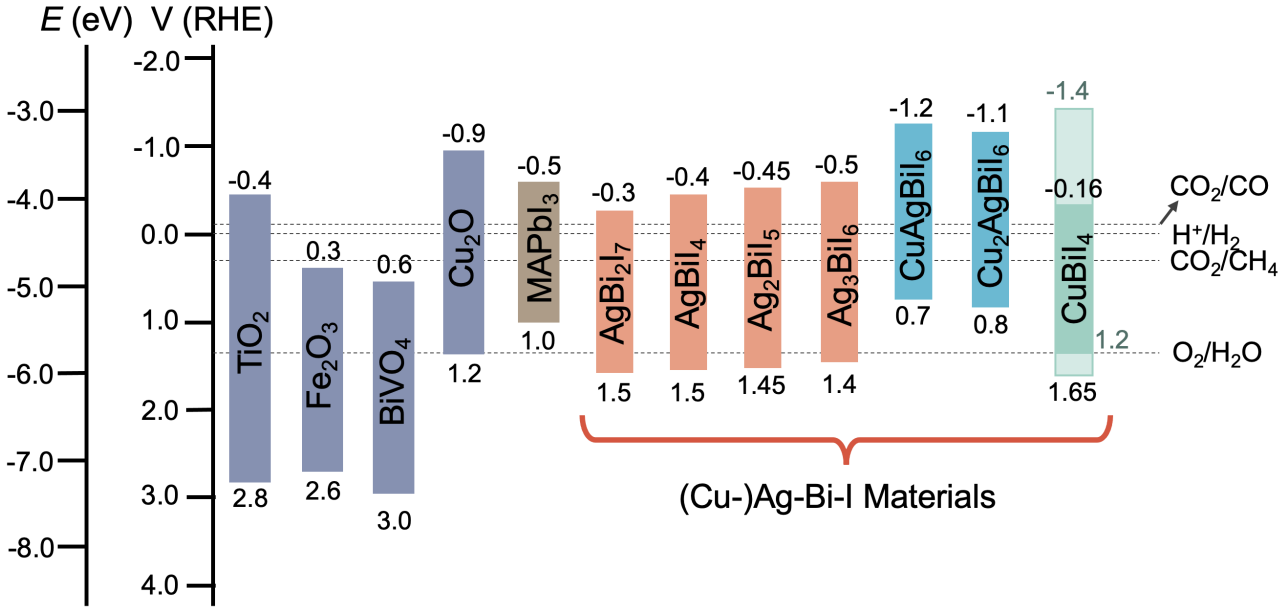

Figure 24: Comparison of the band positions of established semiconductors for photoelectrodes with the band positions of emerging Cu-Ag-Bi-I semiconductors. Band positions are shown relative to vacuum level, and on the reversible hydrogen electrode (RHE) scale, in which 0 V(RHE) is -4.44 ± 0.02 eV.[143] Band positions obtained from Ref.[31,64–67] Please note that Lu *et al.* and Zhang *et al.* reported different sets of band positions and bandgaps for $CuBiI_4$.[66,67] Pairs of band extrema are given in the same color (green or black).

Finally, an area that has not yet been explored is the application of Cu-Ag-Bi-I materials for photocatalysis or photoelectrochemical cells. As shown in Fig. 24, the band positions of Ag-Bi-I and Cu-Bi-I compounds are suitable for proton reduction to form H_2, CO_2 reduction, or water oxidation to form O_2 gas. Stable materials for clean solar fuel production are urgently required, and the device structures developed for photovoltaics can be beneficial for improving the performance and stability of these materials for photocathodes or photoanodes.[9] Furthermore, a bandgap of approximately 2 eV is optimal for single-junction

devices for solar-driven water splitting (*i.e.*, for both water oxidation and reduction), with an efficiency limit estimated to be in the range of 15–17%.[144,145] Cu-Ag-Bi-I, with bandgaps close to this range, are therefore promising for exploration in water splitting, as well as for photoelectrochemistry more broadly.

4. Future Perspectives for Ternary and Quaternary Compounds from the CuI-AgI-BiI_3 Phase Space

(Cu-)Ag-Bi-I compounds have many exciting emerging applications. To fully explore these areas, it will be important to resolve fundamental questions about these materials, and gain further understanding of their process-property-structure-performance relationships in order to more rationally optimize these compounds. Longer-term, it will be important to consider how Cu-Ag-Bi-I materials could be manufactured sustainably and reliably at scale.

4.1 Important Fundamental Questions

One of the key fundamental questions is the nature of charge-carrier transport, and how it is influenced by coupling to phonons in the material. Recent work on Bi-based compounds have shown a wide prevalence of carrier localization due to charge-carrier coupling to acoustic phonons.[1,62,63] Buizza *et al.* have provided insights into this phenomenon in Cu-Ag-Bi-I compounds, but it will be important to extend this over a wider range of stoichiometries and crystal structures. Such insights will be valuable to guide the community to design Cu-Ag-Bi-I compounds that could avoid carrier localization and exhibit long diffusion lengths.

Another important question is the role of defects in the bulk and surface of (Cu-)Ag-Bi-I materials. Although defect tolerance is predicted in materials with strong s-orbital character from heavy-metal pnictogens,[13] the VB density of states in the case of Ag-Bi-I and Cu-Bi-I compounds is dominated by d-orbitals from the transition metal A-site cation. The picture is further complicated by the cation disorder present in compounds containing Ag and Bi, which have the same ionic radii. Joint experimental-computational investigations would

be valuable, and may guide the community towards compositions that could exhibit defect tolerance, or provide guidance on how materials can be processed to avoid the worst traps. In particular, it is important to understand how ion migration can be suppressed in these materials (*e.g.*, in LHPs, fullerene ETLs suppress ionic conduction[95]). Doing so reduces the extent to which ionic conduction obscures the effects of trap states on the capacitance *vs.* frequency spectrum, thus allowing more accurate determination of the traps present through capacitance-based techniques.

At the inter-grain-level, it will be important to understand how defects at grain boundaries affect non-radiative recombination and charge-carrier transport. Such characterization may be accomplished by cathodoluminescence measurements,[146,147] but in the case of Cu-Ag-Bi-I materials is complicated by the weak luminescence present in these materials. EBIC measurements can also be used to link grain structure to charge-carrier properties and early attempts from Pai *et al.* highlight that grain boundaries and interfaces act as active channels for charge-carrier extraction.[65] Another important inter-granular property is microstrain, which is influenced by the degree of misorientation between grains and extended defects (*e.g.*, dislocations). The degree of misorientation can be measured by electron back-scatter diffraction (EBSD), or geometric phase analysis from transmission electron microscopy images. Recent EBSD measurements with LHPs have shown that greater misorientation results in increased non-radiative recombination.[148,149] Similar investigations with Cu-Ag-Bi-I can reveal the true size of grains (as opposed to assuming that the microstructure found in SEM images are grains), and guide the optimization of film processing to improve optoelectronic properties.

Finally, it will be important to understand the degree of ion migration in Cu-Ag-Bi-I, and how ions are segregated macroscopically over the entire film. Hysteresis has been widely found in Cu-Ag-Bi-I solar cells, and ion migration is believed to be the cause of device degradation in some cases. Indeed, Ye *et al.* have proposed that iodide vacancy migration is responsible for resistive switching in micron-thick $AgBiI_4$ films.[35]

4.2 Process-Property-Structure-Performance Relationships

Currently, it is common to report the stoichiometry of Cu-Ag-Bi-I materials based on the starting stoichiometry used in solution synthesis. However, the diffraction patterns of many related stoichiometries are very similar, making phase determination challenging. This is complicated by the presence of phase-impurities, such as AgI-based phases,[105] or other Cu-Ag-Bi-I stoichiometries. Furthermore, investigations into new materials as thin films results in peaks being absent due to texturing, which further complicates accurate phase identification. In-depth studies into powder samples or single crystals to better understand the crystal structure would be important, as would the use of techniques to measure the bulk composition of compounds (*e.g.*, mass spectrometry, Rutherford Backscattering Spectrometry, or X-ray microanalysis).

Beyond the processing of the absorber itself, it will be important to understand how the processing of charge-selective layers on top of the Cu-Ag-Bi-I influences its properties. For example, we and others have found that the addition of *tert*-butylpyridine into spiro-OMeTAD causes the partial dissolution of the Cu-Ag-Bi-I film. In addition, it will be important to understand more how the charge-transport overlayer influences the stability of the Cu-Ag-Bi-I. For example, we have found that Ag-Bi-I thin films, made by hot casting, degrade in ambient air, whereas many groups have reported that full devices are stable in ambient air for several days to months (see Section 3.1.5). The higher apparent stability in devices rather than bare thin films may be due to the role of the overlayer in preventing the ingress of moisture from air, as well as a more optimal morphology being less susceptible to moisture-induced degradation. For example, Hsiao *et al.* found that films with larger grains led to solar cells that degraded more slowly under operation.[105] Thus far, groups have reported Cu-Ag-Bi-I stability mostly based on XRD measurements of the bulk film and the performance of the final photovoltaic devices.[22,40] But it will be important to understand whether changes in the film properties occur when exposed to ambient air without a protective HTL that are not detected

by X-ray diffraction, such as the formation of amorphous regions due to moisture ingress, or due to changes in morphology after ageing in air. Furthermore, it is important to establish more precisely the range of conditions (namely vacuum level, beam flux density) for characterizing Cu-Ag-Bi-I thin films without causing changes in the sample during measurement.

4.3 Sustainable Processing at Scale

Finally, although current efforts have overwhelmingly focussed on simple solution-processing for preparing and investigating Cu-Ag-Bi-I thin films, devising more scalable and reproducible methods of synthesizing these materials will be required for future commercial applications. Recently, Hsiao *et al.* demonstrated the deposition of Ag_3BiI_6 by thermally-assisted doctor blading, achieving solar cells with 2.03% PCE in devices with 1 cm^2 area, comparable with the performance of small 4 mm^2 devices (2.77% PCE).[105] Further efforts to increase the performance of large-area devices, as well as increasing the active area towards 10 cm^2 and beyond are needed. Achieving this through solution-processing is complicated by the difficulty in achieving dense morphology in these Cu-Ag-Bi-I films, which may be due to how the precursor molecules coordinate to the solvent.[46] Furthermore, it will be important to consider the speed of processing films, since this has a direct influence over the cost of manufacturing.[113] It is also important to devise large-scale manufacturing routes for devices that have low thermal budget (and therefore low CO_2eq footprint), with low synthetic complexity, and do not make use of toxic solvents and precursors.[24]

5. Conclusions

In conclusion, over the past few years, ternary and quaternary compounds from the CuI-AgI-BiI_3 phase space have transformed from relative obscurity to intriguing materials for optoelectronic applications. Beginning with initial reports in photovoltaics in 2016, these materials have now been explored for energy harvesting, photodetection, radiation detection, memristors, and artificial synpases for neuromorphic computing. The potential application

space can be much broader, with opportunities also in photocatalysis and solar water splitting. This rich diversity in possible applications stems from the strong absorption of light, stable bandgaps in the range of 1.6-1.9 eV, as well as the high degree of tunability in a range of structural and optoelectronic properties by controlling the composition. At the same time, the fundamental understanding of these materials is at a nascent stage, and more in-depth insights into the nature of charge-carriers and charge-carrier transport are needed, as well as deeper understanding of the role of defects, ion migration and grain boundaries. Furthermore, the rich chemical diversity in the Cu-Ag-Bi-I family of materials should be exploited more, exploring compounds beyond Ag-Bi-I and Cu-Bi-I. Such explorations should be guided by new insights into these materials, such as the role of structure on carrier localization. On the more applied end of the scale, future efforts should also focus on developing the growth of these materials by scalable, rapid and sustainable methods to position these materials for possible commercial applications.

Acknowledgments

The authors would like to acknowledge the input and helpful discussions with Christina (Chuijiang) Kong, and are saddened by her passing prior to the completion of this review. H. Z. and F.C.-P.M. acknowledge funding from Iberdrola through the "Energy for Future (E4F) Postdoctoral Fellowship" (no. 101034297). I. T. acknowledges support from the Japan Society for the Promotion of Science, JSPS KAKENHI (no. 21K05250). H. L. thanks the Department of Chemistry at the University of Oxford for support. R. L. Z. H., H. L. and P. L. acknowledge support from a UK Research and Innovation (UKRI) Frontier Grant (no. EP/X022900/1), awarded via the European Research Council Starting Grant 2021 scheme. R. L. Z. H., H. Z., H. L. and P. L. also acknowledge funding from the Henry Royce Institute Industrial Collaborative Programme scheme, funded by EPSRC (no. EP/X527257/1). F.C-P.M. acknowledges funding from the Engineering and Physical Sciences Research Council (EPSRC, no. EP/V034995/1), and Royal Society (no. RGS/R1/201236). R.W.M. acknowl-

edge support from EPSRC: University of Strathclyde - Equipment Account "Nanoanalysis for Advanced Materials and Healthcare", grant no. EP/K011952/1 and EP/J021199/1. R. L. Z. H. acknowledges funding from the Royal Academy of Engineering through the Research Fellowship scheme (No.: RF/201718/17101), as well as EPSRC (grant no. EP/V014498/1).

Declaration of Interests

The authors declare no conflicts of interest.

References

(1) Buizza, L. R.; Herz, L. M. Polarons and Charge Localization in Metal-Halide Semiconductors for Photovoltaic and Light-Emitting Devices. *Advanced Materials* **2021**, *33*, 2007057.

(2) Hoye, R. L. Z.; Hidalgo, J.; Jagt, R. A.; Correa-Baena, J.-P.; Fix, T.; MacManus-Driscoll, J. L. The Role of Dimensionality on the Optoelectronic Properties of Oxide and Halide Perovskites, and their Halide Derivatives. *Advanced Energy Materials* **2021**, *12*, 2100499.

(3) Choi, J. W.; Shin, B.; Gorai, P.; Hoye, R. L. Z.; Palgrave, R. Emerging Earth-Abundant Solar Absorbers. *ACS Energy Letters* **2022**, *7*, 1553–1557.

(4) Correa-Baena, J.-P.; Saliba, M.; Buonassisi, T.; Grätzel, M.; Abate, A.; Tress, W.; Hagfeldt, A. Promises and challenges of perovskite solar cells. *Science* **2017**, *358*, 739–744.

(5) Yoo, J. J.; Seo, G.; Chua, M. R.; Park, T. G.; Lu, Y.; Rotermund, F.; Kim, Y.-K.; Moon, C. S.; Jeon, N. J.; Correa-Baena, J.-P.; Bulović, V.; Shin, S. S.; Bawendi, M. G.;

Seo, J. Efficient perovskite solar cells via improved carrier management. *Nature* **2021**, *590*, 587–593.

(6) Ma, D. et al. Distribution control enables efficient reduced-dimensional perovskite LEDs. *Nature* **2021**, *599*, 594–598.

(7) Yakunin, S.; Sytnyk, M.; Kriegner, D.; Shrestha, S.; Richter, M.; Matt, G. J.; Azimi, H.; Brabec, C. J.; Stangl, J.; Kovalenko, M. V.; Heiss, W. Detection of X-ray photons by solution-processed lead halide perovskites. *Nature Photonics* **2015**, *9*, 444–449.

(8) She, X.-J.; Chen, C.; Divitini, G.; Zhao, B.; Li, Y.; Wang, J.; Orri, J. F.; Cui, L.; Xu, W.; Peng, J.; Wang, S.; Sadhanala, A.; Sirringhaus, H. A solvent-based surface cleaning and passivation technique for suppressing ionic defects in high-mobility perovskite field-effect transistors. *Nature Electronics* **2020**, *3*, 694–703.

(9) Andrei, V.; Reuillard, B.; Reisner, E. Bias-free solar syngas production by integrating a molecular cobalt catalyst with perovskite–$BiVO_4$ tandems. *Nature Materials* **2019**, *19*, 189–194.

(10) Moody, N.; Sesena, S.; deQuilettes, D. W.; Haynes, C. L.; Bulović, V.; Bawendi, M. G. Assessing the Regulatory Requirements of Lead-Based Perovskite Photovoltaics. *Joule* **2020**, *4*, 970–974.

(11) Hoye, R. L. Z. Preventing lead release from perovskites. *Nature Sustainability* **2023**,

(12) Vidal, R.; Alberola-Borràs, J.-A.; Habisreutinger, S. N.; Gimeno-Molina, J.-L.; Moore, D. T.; Schloemer, T. H.; Mora-Seró, I.; Berry, J. J.; Luther, J. M. Assessing health and environmental impacts of solvents for producing perovskite solar cells. *Nature Sustainability* **2020**, *4*, 277–285.

(13) Brandt, R. E.; Stevanović, V.; Ginley, D. S.; Buonassisi, T. Identifying defect-tolerant semiconductors with high minority-carrier lifetimes: beyond hybrid lead halide perovskites. *MRS Communications* **2015**, *5*, 265–275.

(14) Zakutayev, A.; Caskey, C. M.; Fioretti, A. N.; Ginley, D. S.; Vidal, J.; Stevanović, V.; Tea, E.; ; Lany, S. Defect Tolerant Semiconductors for Solar Energy Conversion. *Journal of Physical Chemistry Letters* **2014**, *5*, 1117–1125.

(15) Ke, W.; Kanatzidis, M. G. Prospects for low-toxicity lead-free perovskite solar cells. *Nature Communications* **2019**, *10*, 965.

(16) Oldag, T.; Aussieker, T.; Keller, H.-L.; Preitschaft, C.; Pfitzner, A. Solvothermale Synthese und Bestimmung der Kristallstrukturen von $AgBiI_4$ und Ag_3BiI_6. *Zeitschrift für anorganische und allgemeine Chemie* **2005**, *631*, 677–682.

(17) Fourcroy, P.; Palazzi, M.; Rivet, J.; Flahaut, J.; Céolin, R. Etude du systeme $AgIBiI_3$. *Materials Research Bulletin* **1979**, *14*, 325–328.

(18) Dzeranova, K. B.; Kaloev, N. I.; Bulakhova, G. A. System BiI_3-AgI. *Russian Journal of Inorganic Chemistry* **1985**, *30*, 2983–2985.

(19) Fourcroy, P.; Carre, D.; Thevet, F.; Rivet, J. Structure du tétraiodure de cuivre (I) et de bismuth (III), $CuBiI_4$. *Acta Crystallographica Section C: Crystal Structure Communications* **1991**, *47*, 2023–2025.

(20) Turkevych, I.; Kazaoui, S.; Ito, E.; Urano, T.; Yamada, K.; Tomiyasu, H.; Yamagishi, H.; Kondo, M.; Aramaki, S. Photovoltaic Rudorffites: Lead-Free Silver Bismuth Halides Alternative to Hybrid Lead Halide Perovskites. *ChemSusChem* **2017**, *10*, 3754–3759.

(21) Turkevych, I.; Urano, T.; Yamagishi, H.; Yamada, K. JP2016161737. 2016.

(22) Kim, Y.; Yang, Z.; Jain, A.; Voznyy, O.; Kim, G.-H.; Liu, M.; Quan, L. N.; García de Arquer, F. P.; Comin, R.; Fan, J. Z.; Sargent, E. H. Pure Cubic-Phase Hybrid Iodobismuthates $AgBi_2I_7$ for Thin-Film Photovoltaics. *Angewandte Chemie International Edition* **2016**, *55*, 9586–9590.

(23) Peng, Y.; Huq, T. N.; Mei, J.; Portilla, L.; Jagt, R. A.; Occhipinti, L. G.; MacManus-Driscoll, J. L.; Hoye, R. L. Z.; Pecunia, V. Lead-Free Perovskite-Inspired Absorbers for Indoor Photovoltaics. *Advanced Energy Materials* **2021**, *11*, 2002761.

(24) Pecunia, V.; Occhipinti, L. G.; Hoye, R. L. Z. Emerging Indoor Photovoltaic Technologies for Sustainable Internet of Things. *Advanced Energy Materials* **2021**, *11*, 2100698.

(25) Rüdorff, W.; Becker, H. Notizen: Die Strukturen von $LiVO_2$, $NaVO_2$, $LiCrO_2$ und $NaCrO_2$. *Zeitschrift für Naturforschung B* **1954**, *9*, 614–615.

(26) Zhu, H.; Erbing, A.; Wu, H.; Man, G. J.; Mukherjee, S.; Kamal, C.; Johansson, M. B.; Rensmo, H.; Odelius, M.; Johansson, E. M. J. Tuning the Bandgap in Silver Bismuth Iodide Materials by Partly Substituting Bismuth with Antimony for Improved Solar Cell Performance. *ACS Applied Energy Materials* **2020**, *3*, 7372–7382.

(27) Ghosh, B.; Wu, B.; Guo, X.; Harikesh, P. C.; John, R. A.; Baikie, T.; Arramel,; Wee, A. T. S.; Guet, C.; Sum, T. C.; Mhaisalkar, S.; Mathews, N. Superior Performance of Silver Bismuth Iodide Photovoltaics Fabricated via Dynamic Hot-Casting Method under Ambient Conditions. *Advanced Energy Materials* **2018**, *8*, 1802051.

(28) Sansom, H. C.; Longo, G.; Wright, A. D.; Buizza, L. R.; Mahesh, S.; Wenger, B.; Zanella, M.; Abdi-Jalebi, M.; Pitcher, M. J.; Dyer, M. S., et al. Highly Absorbing Lead-Free Semiconductor Cu_2AgBiI_6 for Photovoltaic Applications from the Quaternary CuI-AgI-BiI_3 Phase Space. *Journal of the American Chemical Society* **2021**, *143*, 3983–3992.

(29) Cui, Y.; Yang, L.; Wu, X.; Deng, J.; Zhang, X.; Zhang, J. Recent progress of lead-free bismuth-based perovskite materials for solar cell applications. *J. Mater. Chem. C* **2022**, *10*, 16629–16656.

(30) Jin, Z.; Zhang, Z.; Xiu, J.; Song, H.; Gatti, T.; He, Z. A critical review on bismuth and antimony halide based perovskites and their derivatives for photovoltaic applications: recent advances and challenges. *J. Mater. Chem. A* **2020**, *8*, 16166–16188.

(31) Huang, Y.-T.; Kavanagh, S. R.; Scanlon, D. O.; Walsh, A.; Hoye., R. L. Z. Perovskite-Inspired Materials for Photovoltaics and Beyond - From Design to Devices. *Nanotechnology* **2021**, *21*, 132004.

(32) Chakraborty, A.; Pai, N.; Zhao, J.; Tuttle, B. R.; Simonov, A. N.; Pecunia, V. Rudorffites and Beyond: Perovskite-Inspired Silver/Copper Pnictohalides for Next-Generation Environmentally Friendly Photovoltaics and Optoelectronics. *Advanced Functional Materials* **2022**, *32*, 2203300.

(33) Sansom, H. C.; Buizza, L. R.; Zanella, M.; Gibbon, J. T.; Pitcher, M. J.; Dyer, M. S.; Manning, T. D.; Dhanak, V. R.; Herz, L. M.; Snaith, H. J., et al. Chemical Control of the Dimensionality of the Octahedral Network of Solar Absorbers from the CuI–AgI–BiI_3 Phase Space by Synthesis of 3D $CuAgBiI_5$. *Inorganic Chemistry* **2021**, *60*, 18154–18167.

(34) Tie, S.; Zhao, W.; Huang, W.; Xin, D.; Zhang, M.; Yang, Z.; Long, J.; Chen, Q.; Zheng, X.; Zhu, J., et al. Efficient X-ray attenuation lead-free $AgBi_2I_7$ halide rudorffite alternative for sensitive and stable X-ray detection. *The Journal of Physical Chemistry Letters* **2020**, *11*, 7939–7945.

(35) Ye, H.; Liu, Z.; Han, H.; Shi, T.; Liao, G. Lead-free $AgBiI_4$ perovskite artificial synapses for a tactile sensory neuron system with information preprocessing function. *Materials Advances* **2022**, *3*, 7248–7256.

(36) Wu, B. et al. Strong self-trapping by deformation potential limits photovoltaic performance in bismuth double perovskite. *Science Advances* **2021**, *7*, eabd3160.

(37) Wu, M.-C.; Kuo, R.-Y.; Chang, Y.-H.; Chen, S.-H.; Ho, C.-M.; Su, W.-F. Alkali metal cation incorporated Ag_3BiI_6 absorbers for efficient and stable rudorffite solar cells. *Oxford Open Materials Science* **2021**, *1*, itab017.

(38) Crovetto, A.; Hajijafarassar, A.; Hansen, O.; Seger, B.; Chorkendorff, I.; Vesborg, P. C. Parallel evaluation of the BiI_3, BiOI, and Ag_3BiI_6 layered photoabsorbers. *Chemistry of Materials* **2020**, *32*, 3385–3395.

(39) Seo, Y.; Ha, S. R.; Yoon, S.; Jeong, S. M.; Choi, H.; Kang, D.-W. Dynamic casting in combination with ramped annealing process for implementation of inverted planar Ag_3BiI_6 rudorffite solar cells. *Journal of Power Sources* **2020**, *453*, 227903.

(40) Zhu, H.; Pan, M.; Johansson, M. B.; Johansson, E. M. High photon-to-current conversion in solar cells based on light-absorbing silver bismuth iodide. *ChemSusChem* **2017**, *10*, 2592–2596.

(41) Pecunia, V.; Yuan, Y.; Zhao, J.; Xia, K.; Wang, Y.; Duhm, S.; Portilla, L.; Li, F. Perovskite-inspired lead-free Ag_2BiI_5 for self-powered nir-blind visible light photodetection. *Nano-micro letters* **2020**, *12*, 1–12.

(42) He, F.; Wang, Q.; Zhu, W.; Chen, D.; Zhang, J.; Zhang, C.; Hao, Y. Carbon-based, all-inorganic, lead-free Ag_2BiI_5 rudorffite solar cells with high photovoltages. *Solid-State Electronics* **2021**, *176*, 107950.

(43) Ramachandran, A. A.; Krishnan, B.; Avellaneda, D. A.; Palma, M. I. M.; Martinez, J. A. A.; Shaji, S. Photodetection and photocatalytic properties of Ag_2BiI_5 thin films formed by iodization of Ag-BiI3 layers. *Surfaces and Interfaces* **2022**, *30*, 101985.

(44) Sansom, H. C.; Whitehead, G. F.; Dyer, M. S.; Zanella, M.; Manning, T. D.; Pitcher, M. J.; Whittles, T. J.; Dhanak, V. R.; Alaria, J.; Claridge, J. B., et al. $AgBiI_4$ as a lead-free solar absorber with potential application in photovoltaics. *Chemistry of Materials* **2017**, *29*, 1538–1549.

(45) Lu, C.; Zhang, J.; Sun, H.; Hou, D.; Gan, X.; Shang, M.-h.; Li, Y.; Hu, Z.; Zhu, Y.; Han, L. Inorganic and lead-free $AgBiI_4$ rudorffite for stable solar cell applications. *ACS Applied Energy Materials* **2018**, *1*, 4485–4492.

(46) Turkevych, I.; Kazaoui, S.; Shirakawa, N.; Fukuda, N. Potential of $AgBiI_4$ rudorffites for indoor photovoltaic energy harvesters in autonomous environmental nanosensors. *Japanese Journal of Applied Physics* **2021**, *60*, SCCE06.

(47) Shaon, A. R.; Hasan, T.; Mahmood, S. A. Performance Evaluation of $AgBi_2I_7$-based Direct Conversion X-ray Detector. 2021 IEEE International Conference on Telecommunications and Photonics (ICTP). 2021; pp 1–4.

(48) Yang, X.; Zhong, S.; Wang, K.; Ye, Z.; Zhang, R.; Wei, H.; Zhao, L.; Li, W.; Chen, Y.; Cui, Y. Study of Resistive Switching and Biodegradability in Ultralow Power Memory Device Based on All-Inorganic Ag/$AgBi_2I_7$/ITO Structure. *Advanced Materials Interfaces* **2022**, 2200237.

(49) Xiao, Z.; Meng, W.; Mitzi, D. B.; Yan, Y. Crystal structure of $AgBi_2I_7$ thin films. *The Journal of Physical Chemistry Letters* **2016**, *7*, 3903–3907.

(50) Mashadieva, L. F.; Aliev, Z. S.; Shevelkov, A. V.; Babanly, M. B. Experimental investigation of the Ag–Bi–I ternary system and thermodynamic properties of the ternary phases. *Journal of Alloys and Compounds* **2013**, *551*, 512–520.

(51) Huang, Y.-T. et al. Strong Absorption and Ultrafast Localisation in $NaBiS_2$ Nanocrystals with Microsecond Charge-Carrier Lifetimes. *Nature Communications* **2022**, *13*, 4960.

(52) Bera, A.; Paramanik, S.; Maiti, A.; Pal, A. J. Energy landscape in silver-bismuth-iodide rudorffites: Combining scanning tunneling spectroscopy and Kelvin probe force microscopy. *Physical Review Materials* **2021**, *5*, 095404.

(53) Aminoff, G. VII. Über die Kristallstruktur von AgJ. *Zeitschrift für Kristallographie - Crystalline Materials* **1922**, *57*, 180–185.

(54) Trotter, J.; Zobel, T. The crystal structure of SbI_3 and BiI_3. *Zeitschrift für Kristallographie - Crystalline Materials* **1966**, *123*, 67–72.

(55) Wyckoff, R. W. G.; Posnjak, E. The Crystal Structures of the Cuprous Halides. *Journal of the American Chemical Society* **1922**, *44*, 30–36.

(56) Kulkarni, A.; Ünlü, F.; Pant, N.; Kaur, J.; Bohr, C.; Jena, A. K.; Öz, S.; Yanagida, M.; Shirai, Y.; Ikegami, M., et al. Concerted Ion Migration and Diffusion-Induced Degradation in Lead-Free Ag_3BiI_6 Rudorffite Solar Cells under Ambient Conditions. *Solar RRL* **2021**, *5*, 2100077.

(57) Hoye, R. L. Z. et al. Perovskite-Inspired Photovoltaic Materials: Toward Best Practices in Materials Characterization and Calculations. *Chemistry of Materials* **2017**, *29*, 1964–1988.

(58) Park, J. W.; Lim, Y.; Doh, K.-Y.; Jung, M. T.; Jeon, Y. I.; Yang, I. S.; Choi, H.-s.; Kim, J.; Lee, D.; Lee, W. I. Enhancement of the photovoltaic properties of Ag_2BiI_5 by Cu doping. *Sustainable Energy & Fuels* **2021**, *5*, 1439–1447.

(59) Wu, H.; Zhu, H.; Erbing, A.; Johansson, M. B.; Mukherjee, S.; Man, G. J.; Rensmo, H.; Odelius, M.; Johansson, E. M. Bandgap tuning of silver bismuth iodide via controllable bromide substitution for improved photovoltaic performance. *ACS Applied Energy Materials* **2019**, *2*, 5356–5362.

(60) Pazoki, M.; Johansson, M. B.; Zhu, H.; Broqvist, P.; Edvinsson, T.; Boschloo, G.; Johansson, E. M. Bismuth iodide perovskite materials for solar cell applications: electronic structure, optical transitions, and directional charge transport. *The Journal of Physical Chemistry C* **2016**, *120*, 29039–29046.

(61) Hosseini, S.; Adelifard, M.; Ataei, M. An investigation on physical properties of Ag_2BiI_5 absorber layers synthesized by microwave assisted spin coating technique. *Journal of Materials Science: Materials in Electronics* **2019**, *30*, 5021–5029.

(62) Buizza, L. R.; Sansom, H. C.; Wright, A. D.; Ulatowski, A. M.; Johnston, M. B.; Snaith, H. J.; Herz, L. M. Interplay of Structure, Charge-Carrier Localization and Dynamics in Copper-Silver-Bismuth-Halide Semiconductors. *Advanced Functional Materials* **2022**, *32*, 2108392.

(63) Rondiya, S. R.; Jagt, R. A.; MacManus-Driscoll, J. L.; Walsh, A.; Hoye, R. L. Self-trapping in bismuth-based semiconductors: Opportunities and challenges from optoelectronic devices to quantum technologies. *Applied Physics Letters* **2021**, *119*, 220501.

(64) Wu, M.-C.; Wang, Q.-H.; Hsiao, K.-C.; Chen, S.-H.; Ho, C.-M.; Jao, M.-H.; Chang, Y.-H.; Su, W.-F. Composition engineering to enhance the photovoltaic performance and to prolong the lifetime for silver bismuth iodide solar cell. *Chemical Engineering Journal Advances* **2022**, *10*, 100275.

(65) Pai, N. et al. Solution Processable Direct Bandgap Copper-Silver-Bismuth Iodide Photovoltaics: Compositional Control of Dimensionality and Optoelectronic Properties. *Advanced Energy Materials* **2022**, *12*, 2201482.

(66) Hu, Z.; Wang, Z.; Kapil, G.; Ma, T.; Iikubo, S.; Minemoto, T.; Yoshino, K.; Toyoda, T.; Shen, Q.; Hayase, S. Solution-Processed Air-Stable Copper Bismuth Iodide for Photovoltaics. *ChemSusChem* **2018**, *11*, 2930–2935.

(67) Zhang, B.; Lei, Y.; Qi, R.; Yu, H.; Yang, X.; Cai, T.; Zheng, Z. An in-situ room temperature route to $CuBiI_4$ based bulk-heterojunction perovskite-like solar cells. *Science China Materials* **2019**, *62*, 519–526.

(68) Hoye, R. L. Z.; Ehrler, B.; Böhm, M. L.; Muñoz-Rojas, D.; Altamimi, R. M.; Alyamani, A. Y.; Vaynzof, Y.; Sadhanala, A.; Ercolano, G.; Greenham, N. C.; Friend, R. H.; MacManus-Driscoll, J. L.; Musselman, K. P. Improved Open- Circuit Voltage in ZnO–PbSe Quantum Dot Solar Cells by Understanding and Reducing Losses Arising from the ZnO Conduction Band Tail. *Advanced Energy Materials* **2014**, *4*, 1301544.

(69) Hoye, R. L. Z. et al. Strongly Enhanced Photovoltaic Performance and Defect Physics of Air-Stable Bismuth Oxyiodide (BiOI). *Advanced Materials* **2017**, *29*, 1702176.

(70) Pascual-San-José, E.; Rodríguez-Martínez, X.; Adel-Abdelaleim, R.; Stella, M.; Martínez-Ferrero, E.; Campoy-Quiles, M. Blade coated P3HT:non-fullerene acceptor solar cells: a high-throughput parameter study with a focus on up-scalability. *J. Mater. Chem. A* **2019**, *7*, 20369–20382.

(71) Spiro-OMeTAD (Spiro-MeOTAD) (accessed 3/2/23). `https://www.ossila.com/products/spiro-ometad`.

(72) PTAA for Perovskite Applications (accessed 3/2/23). `https://www.ossila.com/products/ptaa-perovskites`.

(73) Miyata, A.; Mitioglu, A.; Plochocka, P.; Portugall, O.; Wang, J. T.-W.; Stranks, S. D.; Snaith, H. J.; Nicholas, R. J. Direct measurement of the exciton binding energy and effective masses for charge carriers in organic–inorganic tri-halide perovskites. *Nature Physics* **2015**, *11*, 582–587.

(74) Pai, N.; Lu, J.; Gengenbach, T. R.; Seeber, A.; Chesman, A. S.; Jiang, L.; Senevirathna, D. C.; Andrews, P. C.; Bach, U.; Cheng, Y.-B., et al. Silver bismuth sulfoiodide

solar cells: tuning optoelectronic properties by sulfide modification for enhanced photovoltaic performance. *Advanced Energy Materials* **2019**, *9*, 1803396.

(75) Min, H.; Lee, D. Y.; Kim, J.; Kim, G.; Lee, K. S.; Kim, J.; Paik, M. J.; Kim, Y. K.; Kim, K. S.; Kim, M. G., et al. Perovskite solar cells with atomically coherent interlayers on SnO_2 electrodes. *Nature* **2021**, *598*, 444–450.

(76) Viezbicke, B. D.; Patel, S.; Davis, B. E.; Birnie III, D. P. Evaluation of the Tauc method for optical absorption edge determination: ZnO thin films as a model system. *physica status solidi (b)* **2015**, *252*, 1700–1710.

(77) Wang, Y.; Liu, Y.; Shi, X.; Huang, L.; Tong, J.; Wang, G.; Pan, D. Alkali-metal-ion-doping strategy to improve the photovoltaic properties of Ag_2BiI_5 solar cells. *New Journal of Chemistry* **2021**, *45*, 14158–14166.

(78) Yu, F.; Wang, L.; Ren, K.; Yang, S.; Xu, Z.; Han, Q.; Ma, T. Cs-incorporated $AgBiI_4$ rudorffite for efficient and stable solar cells. *ACS Sustainable Chemistry & Engineering* **2020**, *8*, 9980–9987.

(79) Hosseini, S.; Adelifard, M. The Impact of Cesium and Antimony Alloying on the Photovoltaic Properties of Silver Bismuth Iodide Compounds. *physica status solidi (a)* **2021**, *218*, 2000774.

(80) Fourcroy, P.; Thevet, F.; Rivet, J.; Carre, D. Contribution à l'étude du système formé par l'iodure cuivreux et le triiodure de bismuth. *Comptes Rendus de l'Academie Des Sciences Serie II* **1990**, *311*, 631–635.

(81) Qu, N.; Lei, Y.; Yang, X.; Hu, X.; Zhao, W.; Zhao, C.; Zheng, Z. From BiI_3 to $CuBiI_4$: a striking improvement in the photoelectric performance of a novel photodetector candidate. *Journal of Materials Chemistry C* **2020**, *8*, 8451–8456.

(82) Baranwal, A. K.; Masutani, H.; Sugita, H.; Kanda, H.; Kanaya, S.; Shibayama, N.; Sanehira, Y.; Ikegami, M.; Numata, Y.; Yamada, K., et al. Lead-free perovskite solar cells using Sb and Bi-based $A_3B_2X_9$ and A_3BX_6 crystals with normal and inverse cell structures. *Nano Convergence* **2017**, *4*, 1–14.

(83) Das, A.; Pal, K.; Acharyya, P.; Das, S.; Maji, K.; Biswas, K. Strong Antibonding I (p)–Cu (d) States Lead to Intrinsically Low Thermal Conductivity in $CuBiI_4$. *Journal of the American Chemical Society* **2023**, *145*, 1349–1358.

(84) The Periodic Table of Elements (accessed 3/15/23). `https://www.webelements.com`.

(85) Ramachandran, A. A.; Krishnan, B.; Avellaneda, D. A.; Palma, M. I. M.; Martinez, J. A. A.; Shaji, S. Development of lead-free Cu_2BiI_5 rudorffite thin films for visible light photodetector application. *Applied Surface Science* **2021**, *564*, 150438.

(86) Wang, L.; Bao, Y.; Wang, S.; Wang, F.; Xie, C.; Butler, K. T.; Fan, X. Revealing the potential crystal structures of earth-abundant nontoxic photovoltaic $CuBiI_4$. *Crystal Growth & Design* **2021**, *21*, 2850–2855.

(87) Yu, L.; Zunger, A. Identification of potential photovoltaic absorbers based on first-principles spectroscopic screening of materials. *Physical Review Letters* **2012**, *108*, 068701.

(88) Yu, H.; Zhang, B.; Qi, R.; Qu, N.; Zhao, C.; Lei, Y.; Yang, X.; Zheng, Z. Gradient formation and charge carrier dynamics of $CuBiI_4$ based perovskite-like solar cells. *Sustainable Energy & Fuels* **2020**, *4*, 2800–2807.

(89) Brandt, R. E.; Poindexter, J. R.; Gorai, P.; Kurchin, R. C.; Hoye, R. L. Z.; Nienhaus, L.; Wilson, M. W. B.; Polizzotti, J. A.; Sereika, R.; Žaltauskas, R.; Lee, L. C.; MacManus-Driscoll, J. L.; Bawendi, M.; Stevanović, V.; Buonassisi, T. Searching for "Defect-Tolerant" Photovoltaic Materials: Combined Theoretical and Experimental Screening. *Chemistry of Materials* **2017**, *29*, 4667–4674.

(90) Sansom, H. *Copper and Silver Bismuth Iodide Semiconductors as Potential Solar Cell Absorber Materials*; The University of Liverpool (United Kingdom), 2018.

(91) Fan, E.; Liu, M.; Yang, K.; Jiang, S.; Li, B.; Zhao, D.; Guo, Y.; Zhang, Y.; Zhang, P.; Zuo, C.; Ding, L.; Zheng, Z. One-Step Gas–Solid-Phase Diffusion-Induced Elemental Reaction for Bandgap-Tunable $Cu_aAg_{m1}Bi_{m2}I_n$/CuI Thin Film Solar Cells. *Nano and Micro Letters* **2023**, *15*.

(92) Islam, M.; Kato, S.; Kishi, N.; Soga, T. Enhanced surface morphology and photovoltaic properties of a new class of material copper silver bismuth iodide solar cell. *Journal of Materials Research and Technology* **2023**, *25*, 4171–4186.

(93) Zhang, F.; Hu, Z.; Zhang, B.; Lin, Z.; Zhang, J.; Chang, J.; Hao, Y. Low-Temperature Solution-Processed Cu_2AgBiI_6 Films for High Performance Photovoltaics and Photodetectors. *ACS Applied Materials & Interfaces* **2022**, *14*, 18498–18505, PMID: 35417144.

(94) Giunta, K. S.; McKee, S. N.; Nicholas, A. D.; Pike, R. D. $BiCuI_4(Pyridine)_5$ a neutral ligand-supported compound of BiI3 and CuI. *Inorganic Chemistry Communications* **2023**, *147*, 110245.

(95) Bisquert, J.; Garcia-Belmonte, G.; Guerrero, A. *Perovskite Photovoltaics and Optoelectronics*; John Wiley & Sons, Ltd, 2022; Chapter 6, pp 173–213.

(96) Jung, K. W.; Sohn, M. R.; Lee, H. M.; Yang, I. S.; Sung, S. D.; Kim, J.; Diaub, E. W.-G.; Lee, W. I. Silver bismuth iodides in various compositions as potential Pb-free light absorbers for hybrid solar cells. *Sustainable Energy & Fuels* **2018**, *2*, 294–302.

(97) Shao, Z.; Mercier, T. L.; Madec, M. B.; Pauporté, T. Exploring $AgBi_xI_{3x+1}$ semiconductor thin films for lead-free perovskite solar cells. *Materials and Design* **2018**, *141*, 81–87.

(98) Shao, Z.; Le Mercier, T.; Madec, M. B.; Pauporté, T. $AgBi_2I_7$ layers with controlled surface morphology for solar cells with improved charge collection. *Materials Letters* **2018**, *221*, 135–138.

(99) Jia, X.; Ding, L. A low-temperature solution-processed copper antimony iodide rudorffite for solar cells. *Science China-Materials* **2018**, *62*, 54–58.

(100) Kulkarni, A.; Jena, A. K.; Ikegami, M.; Miyasaka, T. Performance enhancement of $AgBi_2I_7$ solar cells by modulating a solvent-mediated adduct and tuning remnant BiI_3 in one-step crystallization. *Chemical Communications* **2019**, *55*, 4031–4034.

(101) Zhang, Q.; Wu, C.; Qi, X.; Lv, F.; Zhang, Z.; Liu, Y.; Wang, S.; Qu, B.; Chen, Z.; Xiao, L. Photovoltage Approaching 0.9 V for Planar Heterojunction Silver Bismuth Iodide Solar Cells with Li-TFSI Additive. *ACS Applied Energy Materials* **2019**, *2*, 3651–3656.

(102) Hu, W.; He, X.; Fang, Z.; Lian, W.; Shang, Y.; Li, X.; Zhou, W.; Zhang, M.; Chen, T.; Lu, Y.; Zhang, L.; Ding, L.; Yang, S. Bulk heterojunction gifts bismuth-based lead-free perovskite solar cells with record efficiency. *Nano Energy* **2020**, *68*, 104362.

(103) Zhai, W.; Huang, L.; Cui, X.; Li, G.; Zhang, Z.; Chen, P.; Li, Y.; Tang, Y.; Lin, L.; Yan, Z.; Liu, J.-M. Tuning the morphology and optoelectronic properties of $AgBiI_4$ film through isopropanol treatment. *Journal of Materials Chemistry C* **2022**, *10*, 5321–5327.

(104) Hosseini, S.; Adelifard, M. The Effect of Multi-walled Carbon Nanotubes and Reduced Graphene Oxide Doping on the Optical and Photovoltaic Performance of Ag_2BiI_5-Based Solar Cells. *Journal of Electronic Materials* **2020**, *49*, 5790–5800.

(105) Hsiao, K.-C.; Yu, Y.-F.; Ho, C.-M.; Jao, M.-H.; Chang, Y.-H.; Chen, S.-H.; Chang, Y.-H.; Su, W.-F.; Lee, K.-M.; Wu, M.-C. Doping engineering of carrier transporting

layers for ambient-air-stable lead-free rudorffite solar cells prepared by thermal-assisted doctor blade coating. *Chemical Engineering Journal* **2023**, *451*, 138807.

(106) Khazaee, M.; Sardashti, K.; Chung, C.-C.; Sun, J.-P.; Zhou, H.; Bergmann, E.; Dunlap-Shohl, W. A.; Han, Q.; Hill, I. G.; Jones, J. L.; Lupascu, D. C.; Mitzi, D. B. Dual-source evaporation of silver bismuth iodide films for planar junction solar cells. *Journal of Materials Chemistry A* **2018**, *7*, 2095–2105.

(107) Yi, Z.; Zhang, T.; Ban, H.; Shao, H.; Gong, X.; Wu, M.; Liang, G.; Zhang, X. L.; Shen, Y.; Wang, M. $AgBi_3I_{10}$ rudorffite for photovoltaic application. *Solar Energy* **2020**, *206*, 436–442.

(108) Merker, A.; Morgenroth, M.; Scholz, M.; Lenzer, T.; Oum, K. Critical Evaluation of the Photovoltaic Performance of $(AgI)_x(BiI_3)_y$ Thin Films from the Viewpoint of Ultrafast Spectroscopy and Photocurrent Experiments. *The Journal of Physical Chemistry C* **2023**, *127*, 1487–1498.

(109) Iyoda, F.; Nishikubo, R.; Wakamiya, A.; Saeki, A. Ag-(Bi, Sb, In, Ga)-I Solar Cells: Impacts of Elemental Composition and Additives on the Charge Carrier Dynamics and Crystal Structures. *ACS Applied Energy Materials* **2020**, *3*, 8224–8232.

(110) Grandhi, G. K.; Al-Anesi, B.; Pasanen, H.; Ali-Löytty, H.; Lahtonen, K.; Granroth, S.; Christian, N.; Matuhina, A.; Liu, M.; Berdin, A.; Pecunia, V.; Vivo, P. Enhancing the Microstructure of Perovskite-Inspired Cu-Ag-Bi-I Absorber for Efficient Indoor Photovoltaics. *Small* **2022**, *18*, 2203768.

(111) Dunlap-Shohl, W. A.; Zhou, Y.; Padture, N. P.; Mitzi, D. B. Synthetic Approaches for Halide Perovskite Thin Films. *Chemical Reviews* **2019**, *119*, 3193–3295.

(112) Potential of $AgBiI_4$ rudorffites for indoor photovoltaic energy harvesters in autonomous environmental nanosensors. 33rd International Microprocesses and Nanotechnology Conference (MNC-2020), Nov. 9, 2020, Osaka, Japan.

(113) Perini, C. A.; Doherty, T. A.; Stranks, S. D.; Correa-Baena, J.-P.; Hoye, R. L. Pressing challenges in halide perovskite photovoltaics—from the atomic to module level. *Joule* **2021**, *5*, 1024–1030.

(114) IEC 61216-1:2021/COR1:2021 Corrigendum 1 - Terrestrial photovoltaic (PV) modules - Design qualification and type approval - Part 1: Test requirements (IEC Webstore, 2023) (accessed 3/2/23). https://webstore.iec.ch/publication/68934.

(115) Mathews, I.; Kantareddy, S. N. R.; Sun, S.; Layurova, M.; Thapa, J.; Correa-Baena, J.-P.; Bhattacharyya, R.; Buonassisi, T.; Sarma, S.; Peters, I. M. Self-Powered Sensors Enabled by Wide-Bandgap Perovskite Indoor Photovoltaic Cells. *Advanced Functional Materials* **2019**, *29*, 1904072.

(116) Mathews, I.; Kantareddy, S. N.; Buonassisi, T.; Peters, I. M. Technology and Market Perspective for Indoor Photovoltaic Cells. *Joule* **2019**, *3*, 1415–1426.

(117) Michaels, H.; Rinderle, M.; Freitag, R.; Benesperi, I.; Edvinsson, T.; Socher, R.; Gagliardi, A.; Freitag, M. Dye-sensitized solar cells under ambient light powering machine learning: towards autonomous smart sensors for the internet of things. *Chemical Science* **2020**, *11*, 2895–2906.

(118) Connecting for Net-Zero: Addressing the Climate Change Crisis through Digital Technology (accessed 1/7/23). https://newscentre.vodafone.co.uk/app/uploads/2021/09/Connecting-Net-Zero-090921-Pages-1.pdf.

(119) Dong, C.; Li, X.-M.; Ma, C.; Yang, W.-F.; Cao, J.-J.; Igbari, F.; Wang, Z.-K.; Liao, L.-S. Lycopene-Based Bionic Membrane for Stable Perovskite Photovoltaics. *Advanced Functional Materials* **2021**, *31*, 2011242.

(120) Wang, K.-L. et al. Ion–Dipole Interaction Enabling Highly Efficient $CsPbI_3$ Perovskite Indoor Photovoltaics. *Advanced Materials* **2023**, *35*, 2210106.

(121) Arivazhagan, V.; Gun, F.; Reddy, R. K. K.; Li, T.; Adelt, M.; Robertson, N.; Chen, Y.; Ivaturi, A. Indoor light harvesting lead-free 2-aminothiazolium bismuth iodide solar cells. *Sustainable Energy & Fuels* **2022**, *6*, 3179–3186.

(122) Al-Anesi, B.; Grandhi, G. K.; Pecoraro, A.; Sugathan, V.; Viswanath, N. S. M.; Ali-Löytty, H.; Liu, M.; Ruoko, T.-P.; Lahtonen, K.; Manna, D.; Toikkonen, S.; Muñoz-García, A. B.; Pavone, M.; Vivo, P. Antimony-bismuth alloying: the key to a major boost in the efficiency of lead-free perovskite-inspired indoor photovoltaics. *ChemRxiv* **2023**, 1–37.

(123) Reich, N.; van Sark, W.; Turkenburg, W. Charge yield potential of indoor-operated solar cells incorporated into Product Integrated Photovoltaic (PIPV). *Renewable Energy* **2011**, *36*, 642–647.

(124) Freunek, M.; Freunek, M.; Reindl, L. M. Maximum efficiencies of indoor photovoltaic devices. *IEEE Journal of Photovoltaics* **2013**, *3*, 59–64.

(125) De Rossi, F.; Pontecorvo, T.; Brown, T. M. Characterization of photovoltaic devices for indoor light harvesting and customization of flexible dye solar cells to deliver superior efficiency under artificial lighting. *Applied Energy* **2015**, *156*, 413–422.

(126) Ma, L.-K.; Chen, Y.; Chow, P. C.; Zhang, G.; Huang, J.; Ma, C.; Zhang, J.; Yin, H.; Hong Cheung, A. M.; Wong, K. S.; So, S. K.; Yan, H. High-Efficiency Indoor Organic Photovoltaics with a Band-Aligned Interlayer. *Joule* **2020**, *4*, 1486–1500.

(127) Du, X.; Heumueller, T.; Gruber, W.; Classen, A.; Unruh, T.; Li, N.; Brabec, C. J. Efficient Polymer Solar Cells Based on Non-fullerene Acceptors with Potential Device Lifetime Approaching 10 Years. *Joule* **2019**, *3*, 215–226.

(128) Directive 2011/65/EU of the European Parliament and of the Council of 8 June 2011 on the restriction of the use of certain hazardous substances in electrical and electronic equipment (recast) (accessed 1/8/23). `https://tinyurl.com/bde9wsyf`.

(129) Li, T.; Wang, Q.; Nichol, G. S.; Morrison, C. A.; Han, H.; Hu, Y.; Robertson, N. Extending lead-free hybrid photovoltaic materials to new structures: thiazolium, aminothiazolium and imidazolium iodobismuthates. *Dalton Trans.* **2018**, *47*, 7050–7058.

(130) Zhao, Y.; Zhou, W.; Ma, W.; Meng, S.; Li, H.; Wei, J.; Fu, R.; Liu, K.; Yu, D.; Zhao, Q. Correlations between Immobilizing Ions and Suppressing Hysteresis in Perovskite Solar Cells. *ACS Energy Letters* **2016**, *1*, 266–272.

(131) de Arquer, F. P. G.; Armin, A.; Meredith, P.; Sargent, E. H. Solution-processed semiconductors for next-generation photodetectors. *Nature Reviews Materials* **2017**, *2*, 16100.

(132) Saki, Z.; Byranvand, M. M.; Taghavinia, N.; Kedia, M.; Saliba, M. Solution-processed perovskite thin-films: the journey from lab- to large-scale solar cells. *Energy Environ. Sci.* **2021**, *14*, 5690–5722.

(133) Park, J. W.; Kang, B. H.; Kim, H. J. A Review of Low-Temperature Solution-Processed Metal Oxide Thin-Film Transistors for Flexible Electronics. *Advanced Functional Materials* **2020**, *30*, 1904632.

(134) Premkumar, S.; Liu, D.; Zhang, Y.; Nataraj, D.; Ramya, S.; Jin, Z.; Mamba, B. B.; Kuvarega, A. T.; Gui, J. Stable Lead-Free Silver Bismuth Iodide Perovskite Quantum Dots for UV Photodetection. *ACS Applied Nano Materials* **2020**, *3*, 9141–9150.

(135) Prasad, M. D.; Krishna, M. G.; Batabyal, S. K. Silver Bismuth Iodide Nanomaterials as Lead-Free Perovskite for Visible Light Photodetection. *ACS Applied Nano Materials* **2021**, *4*, 1252–1259.

(136) Adappattu Ramachandran, A.; Krishnan, B.; Avellaneda Avellaneda, D.; Isabel Mendivil Palma, M.; Amilcar Aguilar Martinez, J.; Shaji, S. Development of lead-free

Cu_2BiI_5 rudorffite thin films for visible light photodetector application. *Applied Surface Science* **2021**, *564*, 150438.

(137) Li, G.; Wang, Y.; Huang, L.; Sun, W. Research Progress of High-Sensitivity Perovskite Photodetectors: A Review of Photodetectors: Noise, Structure, and Materials. *ACS Applied Electronic Materials* **2022**, *4*, 1485–1505.

(138) Dan, Y.; Zhao, X.; Chen, K.; Mesli, A. A Photoconductor Intrinsically Has No Gain. *ACS Photonics* **2018**, *5*, 4111–4116.

(139) Wei, H.; Huang, J. Halide lead perovskites for ionizing radiation detection. *Nature Communications* **2019**, *10*, 1066.

(140) Pan, W. et al. $Cs_2AgBiBr_6$ single-crystal X-ray detectors with a low detection limit. *Nature Photonics* **2017**, *11*, 726–732.

(141) He, Y.; Hadar, I.; Kanatzidis, M. Detecting ionizing radiation using halide perovskite semiconductors processed through solution and alternative methods. *Nature Photonics* **2021**, *16*, 14–26.

(142) Ye, H.; Sun, B.; Wang, Z.; Liu, Z.; Zhang, X.; Tan, X.; Shi, T.; Tang, Z.; Liao, G. High performance flexible memristors based on a lead free $AgBiI_4$ perovskite with an ultralow operating voltage. *Journal of Materials Chemistry C* **2020**, *8*, 14155–14163.

(143) van de Krol, R.; Grätzel, M. *Photoelectrochemical Hydrogen Production*; Springer, 2012.

(144) Murphy, A.; Barnes, P.; Randeniya, L.; Plumb, I.; Grey, I.; Horne, M.; Glasscock, J. Efficiency of solar water splitting using semiconductor electrodes. *International Journal of Hydrogen Energy* **2006**, *31*, 1999–2017.

(145) Fountaine, K. T.; Lewerenz, H. J.; Atwater, H. A. Efficiency limits for photoelectrochemical water-splitting. *Nature Communications* **2016**, *7*, 13706.

(146) Jagadamma, L. K.; Edwards, P. R.; Martin, R. W.; Rusekas, A.; Samuel, I. D. W. Nanoscale Heterogeneity in $CsPbBr_3$ and $CsPbBr_3$:KI Perovskite Films Revealed by Cathodoluminescence Hyperspectral Imaging. *ACS Applied Energy Materials* **2021**, *4*, 2707.

(147) Li, Z.; Senanayak, S. P.; Dai, L.; Kusch, G.; Shivanna, R.; Zhang, Y.; Pradhan, D.; Ye, J.; Huang, Y.-T.; Sirringhaus, H.; Oliver, R. A.; Greenham, N. C.; Friend, R. H.; Hoye, R. L. Z. Understanding the Role of Grain Boundaries on Charge-Carrier and Ion Transport in $Cs_2AgBiBr_6$ Thin Films. *Advanced Functional Materials* **2021**, *31*, 2104981.

(148) Jariwala, S.; Sun, H.; Adhyaksa, G. W.; Lof, A.; Muscarella, L. A.; Ehrler, B.; Garnett, E. C.; Ginger, D. S. Local Crystal Misorientation Influences Non-radiative Recombination in Halide Perovskites. *Joule* **2019**, *3*, 3048–3060.

(149) Ghosh, P.; Bruckbauer, J.; Trager-Cowan, C.; Krishnan Jagadamma, L. Crystalline grain engineered $CsPbIBr_2$ films for indoor photovoltaics. *Applied Surface Science* **2022**, *592*, 152865.